공학박사학위논문

Mathematical modeling of complex distributed parameter system: Discretization approach

복잡한 분포정수계의 수학적 모델링:

이산화 접근법

2019 년 8 월

서울대학교 대학원

화학생물공학부

이 용 규

Mathematical modeling of complex distributed parameter system: Discretization approach

복잡한 분포정수계의 수학적 모델링: 이산화 접근법

지도교수 이 원 보

이 논문을 공학박사 학위논문으로 제출함

2019 년 6 월

서울대학교 대학원

화학생물공학부

이 용 규

이용규의 박사 학위논문을 인준함

2019 년 6 월

위 원 장	이 종 민	(인)
부 위 원 장	이 원 보	(인)
위 원	이 규 태	(인)
위 원	남 재 욱	(인)
위 원	이 철 진	(인)

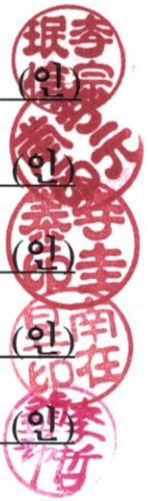

Abstract

Mathematical modeling of complex distributed parameter system: Discretization approach

Yongkyu Lee

School of Chemical & Biological Engineering

The Graduate School of Seoul National University

In recent years, many researchers in chemical engineering have made great efforts to develop mathematical models on the theoretical side that are consistent with experimental results. Despite these efforts, however, establishing models for a system with complex phenomena such as multiphase flow or stirred reactors is still considered to be a challenge. In the meantime, an increase in computational efficiency and stability in various numerical methods has allowed us to correctly solve and analyze the system based on the fundamental equations. This leads to the need for a mathematical model to accurately predict the behavior of systems in which there is interdependence among the internal elements. A methodology for building a model based on equations that represent fundamental phenomena can lower technical barriers in system analysis.

In this thesis, we propose three mathematical models validated from laboratory or pilot-scale experiments. First, an apparatus for vaporizing liquid natural gas is surrounded with a frost layer formed on the surface during operation, and performance of the apparatus is gradually deteriorated due to the adiabatic effect. Because the system uses ambient air as a heat sink, it is necessary to consider the phase transition and mass transfer of water vapor, and natural gas in the air in order to understand the fluctuation of system characteristics. The model predicts the experimental data of a pilot-scale vaporizer within a mean absolute error of 5.5 %. In addition, we suggest the robust design methodology and optimal design which is able to maintain the efficiency under the weather conditions for a year. Two or more data analysis techniques including discrete waveform transformation and *k*-means clustering are used to extract features that can represent time series data. Under the settings, the performance in the optimized desgin is improved by 22.92 percentage points compared to that in the conventional system.

In the second system, the continuous tubular crystallization reactor has advantages in terms of production capacity and scale-up compared with the conventional batch reactor. However, the tubular system requires a well-designed control system to maintain its stability and durability, and thus; there is a great deal of demand for the mathematical model of this system. We were able to estimate crystal size distribution by considering the population balance model simultaneously with several heat exchanger models. The model constructed based on the first principle reaction scheme successfully predicted the results from the full-factorial experiment. The experiments were conducted with LAM (L-asparagine monohydrate) solution. In the prediction, the average

crystal length and standard deviation were within 20% of the results of an experiment where the crystals were not iteratively dissolved in the liquid but maintained a low-level supersaturation. Furthermore, to confirm the controllability of the crystal size distribution in the system, we replaced the LAM solution with HEWL (Hen-egg white lysozyme) solution.

Finally, we propose a multi-compartment model to predict the behavior of a high-pressure autoclave reactor for polymer production. In order to simulate a complex polymer synthesis mechanism, the rotation effect of impellers in the reactor on polymerization and the influence caused by polymerization heat were sequentially evaluated. As a result, This model turned out to be able to predict the physical properties of the polymers produced in an industrial-scale reactor within 7% accuracy.

In this thesis, all three systems are distributed parameter systems which can be expressed as partial differential equations for time and space. To construct a high order model, the system was interpreted based on discretization approach under minimal assumptions. This methodology can be applied not only to the systems suggested in this thesis but also to those consisting of interpdependent variables. I hope that this thesis provides guidance for further researches of chemical engineering in nearby future.

Keywords: mathematical modeling, parameter estimation, distributed parameter system, ambient air vaporizer, population balance modeling, continuous crystallization process, high-pressure autoclave reactor

Student Number: 2014-22598

Contents

List of Figures

List of Tables

Chapter 1

Introduction

1.1 Research motivation

Technological developments of mathematical modeling and estimation methodologies have made significant advances in understanding various physical and chemical phenomena: Intermolecular forces, reaction kinetics, phase change, thermodynamics and hydrodynamics. With the aid of sufficient capacities of computer resources and computational efficiency, developed techniques can be widely used in research academia and industry. Recently multi-phase systems which consists of gas, liquid, and solid; crystallization and pharmaceutical process for tighter specifications on product quality; and chemical reactors where fluid flow behavior affects the reaction mechanism of components, which could not be numerically solved without appropriate assumptions and simplified version of the system, are likely to be dealt with rigorous models. The models, also referred to as 'first-principle based model' are capable of representing and simulating the systems using algebraic equations (*e.g.* the formulas of heat capacity, conductivity, and kinetic parameters), differential equations (*e.g.* Fourier's law of conduction, crystal growth equations, and reaction rate of chemical compound), and balance equations (*e.g.* mass, momentum, and energy balances). The parameters of first-principle equations should be calibrated and estimated for enhancing accuracy. The estimation can be done with comparison between simulation results and dataset from lab-scale experiments or pilot-scale plants. Precise prediction of

target system performance and characteristics of the product facilitates understanding of the system, cost-effective operation and design, and customized manufacturing.

In this thesis, complex phenomena of systems are expressed in partial differential equations. Called as a distributed parameter system, three systems can be solved and analayzed with the discretization approach. First, the ambient air vaporizer (AAV), which is one of the equipment for liquid natural gas (LNG) regasification, is designed with dynamic conditions of the atmosphere. The water vapor in the air is condensed into frost on the surface of the fin tube due to its direct contact with cryogenic liquid. These phase transition of the substances and coexistence of several diverse components make it hard to design and operate the regasification machinery. The multi-phase and multi-component system can be evaluated and analyzed in detail by modeling sublimation of water vapor and heat transfer between matierals with proper estimated values of empirical and first-principle quations parameters.

Second, modeling and analysis methodology is also employed to build up a mathematical model of the pharmaceutical crystallization process. Occuring in moderate conditions only, the formation of crystalline requires a thoroughly operated and controlled apparatus, such as temperature controlled bath, stirring system, and parallel peristaltic pumps to result in the product as intended. Therefore, an accurate process model is the linchpin of the control system development. With a well-developed model, the functionality of the control system can be verified, tuning gains via simulation, and optimization of the crystallizer. Finally, a high-pressure polymerization autoclave reactor is also

needed to be modeled to design and optimize the molecular weight distribution of a resin product. The main challenge is to evaluate and analyze the effects of impeller rotation at reaction rates. In order to revamp the properties of the polymer and manipulate the equipment properly, it is indispensable to be equipped with a polymer reactor model that is time-saving, simple, and well-constructed.

To construct rigorous models for the systems, as we mentioned above, we treated them as distributed parameter systems which have more interconnection among variables than lumped parameter systems. The systems were not modeled, analyzed, and estimated in the same ways before. Furthermore, the proposed methodologies and procedure have the potential to be applied to another complicated system modeling. In such systems, the patterns of interactions among components have an influence on both behavior of the whole system and its productive capacity, requiring a greater deal of demand for these modeling processes.

1.2 Research objective

The systems are mathematically modeled, validated with the experimentally obtained dataset, evaluated and analyzed with properly fitted parameters. First of all, all works are established under first-principle equations and foundational belief with minimum assumptions and simplification. Basic phenomena including heat and mass transfer among fluids and solids, phase transition of materials, and fluid behavior induced by rotating structure occurred in the target system are fully understood and compared with other earlier studies. Then,

foundational equations for representing the phenomena are enumerated and represented as matrices which are easily treated with linear algebra and statistics. However, exact solution is hard to be found for these problems in general, causing numerical approaches to be more preferred for their convenience and easy to use. For this reason, a variety of solvers are used to induce a numerical approximation of solutions of ordinary differential equations (ODEs), partial differential equations (DAEs), and differential algebraic equations (DAEs). For example, Euler's method is commonly used for calculating the first-order ODE with a given initial point. As a modified version of Euler's method, second order and fourth order Runge-Kutta methods provide further improved solution with smaller local and global errors. There are many other differential equation solvers besides these examples, such as Adams-Moulton for computing the successive point with one previous point, IDA solver for DAEs, and CVODE for treating stiff and non-stiff system. The solution derived from these solvers is demonstrated with experimental results. In this process, the empirically induced or misinterpret parameters should be calibrated and estimated to fit the data points. In this thesis, all of these procedures are done in three different systems with a detailed description of methods and results.

1.3 Outline of the thesis

This thesis consists of five chapters. Chapter 1 explains reasons for studying these projects and topics with the specification of the objects in detail. Furthermore thesis outline is listed with associated publications to clarify the

relative papers and co-authors. Since complex systems are recognized as distributed parameter systems, properties and modeling approaches of the systems are described in Chapter 2. From Chapter 3 to Chapter 5, the systems are numerically modeled and demonstrated with each experimental data set. The abstract of each chapter is described below this paragraph. Finally, Chapter 6 deals with the contribution of each project, which summarizes the results and their potential to be applied to other projects and systems. Future work is also suggested to intrigue other researchers and provide a guideline for their further research on the topic treated in this thesis.

- Chapter 3

During the operation of an ambient air vaporizer (AAV) designed for vaporizing liquefied natural gas (LNG), the condensation of water vapor results in frost accumulation on the surface of the vaporizer tubes. The frost deposited on the surface lowers the heat transfer rate because the thermal conductivity of frost is less than 1/40 times the thermal conductivity of aluminum, which was used as the material for the tube and fin. It is essential to understand the behavior of frost accumulation because the actual challenge in this field is to predict frost growth in cryogenic conditions and the dynamic heat transfer performance of the AAV owing to frost. In this study, the formation of a frost layer on the surface of an LNG vaporizer and the reduction in heat performance are evaluated using a dynamic numerical model that combines heat transfer and mass transfer. The trend of frost growth and the temperature profile of LNG with position and time were studied by modeling and simulation. The numerical results predicted by the model are validated by the experimental data of a pilot-

scale AAV, and the mean absolute error (MAE) between the experimental data and model-predicted values was 5.5%. The water vapor condensed by cryogenic LNG in the vicinity of the inlet augments the frost and increases the heat transfer resistance. Under the experimental conditions, when 1 to 2 mm of frost accumulates every 2 h, sensible heat flux is reduced by 15% after 6 h. It is observed from the growing tendency of the frost that the region where LNG is vaporized shifts to the back of the tube over time. Sensitivity analysis of air conditions such as relative humidity, temperature, and velocity presents guidelines for selecting the plant location, climatic conditions, and capacity of fans.

With the constructed model of AAV, a methodology for the robust design of an ambient-air vaporizer under time-series weather conditions is proposed. Two techniques are used to extract representative features in the time-series data. (i) The major trend of a day is rapidly identified by the discrete wavelet transform (DWT), in which a high level of Haar function reflects the trend of a day and drastically reduces the data size. (ii) The *k*-means clustering method groups the similar features of a year, and the reconstructed time-series dataset extracted by the centroids of clusters represent the weather conditions of a year. The results of the multi-feature-based optimization were compared with non-wavelet based and multi-period optimization by simulation under a year of data. The design structure from the feature extraction shows 22.75% better performance than the original case and is 12 times more robust in different weather conditions than clustering with raw data.

- Chapter 4

Despite the many advantages of the continuous crystallization to increase consistency and flexibility of process; reduce operational variability and capital cost; and improve control of product specifications, there are few models of the system that give a reasonable description of the crystal formation kinetic. With the reasons, the population balance model of continuous tubular crystallizer is established to evaluate and analyze the effect of temperature trajectory through slug and insonation on the crystal size distribution. The measurement dataset extracted from a large full-factorial design of experiments is verified and compared with the predicted crystal size distribution from the discretized population balance model on the basis of first-principle kinetics whose parameters are estimated in global optimization strategy. The predicted mean crystal length and the standard deviation is reasonably accurate with <20% prediction error compared with the result of experiments performed at the dissolution-free and low level of supersaturation environment.

Because the above population balance model is developed under L-asparagine monohydrate (LAM) crystallization process, construction and validation cannot provide sufficient evidence to be applied to the pharmaceutical process. Nonetheless, the population balance model, in conjunction with the mass transfer and thermodynamic, precisely describes the crystallization process, and increase the possibility of prediction and control of product quality in continuous manufacturing of pharmaceuticals. This statement is assured with further research where the hen egg white lysozyme (HEWL), one of the affordable proteins, is used as a solute molecule.

Accompanied with the growth of biopharmaceuticals market, the demand for improvement of product quality with a minimal cost is increased, and the

need for the development of genuinely continuous manufacturing process for the production of the high-value biological product on a large scale has been continuously brought up. Even with the requirement and benefits of the continuous process, the lack of sufficient comprehension about the mechanism of crystallization and a wide range of controllable variables hinders the advance in the system. This article provides the continuous tubular crystallizer eligible to tune particle size distribution of product and control the spatial temperature through a tubular body with the rigorously estimated mathematical model of the system. Under the proper buffer and pH condition, the magnitude and dispersion of product crystals are reproducibly manipulated using fully controlled temperature profile over a 25 – 30 minutes residence time and the formation of amorphous precipitates can be achieved under higher supersaturation condition ($\Delta\sigma_{max}\sim220$) via the addition of concentrated precipitant. The demonstration of tunable continuous crystallization process would likely have a profound impact on the biopharmaceutical industry and potentially result in increased worldwide access to biologic drugs at substantially reduced costs.

- Chapter 5

With the growth in the ethylene-vinyl acetate (EVA) resin market supplemented by the increase in demand for flexible packaging of food and personal care, there are opportunities in the development of polymerization process designed to produce the high-performance product. The high-pressure autoclave reactor, one of the processes for the production of higher percentage by weight of vinyl acetate, ensures valuable polymer properties and prevents runaway decomposition when it is explicitly modeled on the comprehension of

hydrodynamics and free-radical polymerization. In this chapter, we present a multi-compartment model of an ethylene–vinyl acetate autoclave reactor including the mixing effects of the stirring device calculated using computational fluid dynamics; the model is simplified by cell aggregation and the polymerization kinetics is modeled with the method of moments. The proposed model has been verified through comparison of the predicted product properties and locally distributed temperatures with those from an industrial plant. The proposed model, which is capable of simulating a complex system with low computational load, can be applied to maintain consistent product quality, prevent undesired thermal runaway, and optimize the conversion and production rates.

1.4 Associated publications

The works of Chapter 3.2 and Chapter 3.4 are written based on [1]. The works in Chapter 3.3 and Chapter 3.4 are present in [2]. The contents in Chapter 4 were already built in two journal papers but they are not submitted yet. However, the works were performed in conjunction with *Nicholas J. Mozdzierz* and the relative substances were also presented in his thesis [3] which is not published yet. The works in Chapter 5 are also not yet published but the content has been submitted to *Industrial & Engineering Chemistry Research*.

Chapter 2

Distributed parameter system

2.1 Introduction

With the advance of technology, such as real-time control system, monitoring, and prediction system, conventional methodologies to analyze the lumped parameter system (LPS) are no longer useful. Nowadays, the most sophisticated process tends to be regarded as a distributed parameter system (DPS) where the input, output and even parameters can vary both temporally and spatially [4]. While an ordinary differential equation (ODE) is enough to explain LPS, DPS should be expressed in partial differential equations (PDE) due to its coupled time-space. Since such systems are known as infinite-dimensional systems in which solution should be an arbitrary function, the problem could not be solved with general ODE solver such as Runge-Kutta methods. Therefore, they cannot be easily solved and approached with their original forms. For example, wave equation

$$\frac{\partial^2\psi}{\partial x^2}+\frac{\partial^2\psi}{\partial y^2}+\frac{\partial^2\psi}{\partial z^2}=\frac{1}{\nu}\frac{\partial^2\psi}{\partial t^2} \tag{2-1}$$

is one of the popular PDE involving functions and their partial derivatives. Dependence of the function ψ on the variables (x, y, z, t) makes it difficult to be solved with common approaches. Only linear second-order PDE can be analytically solved among the number of the equation types. The linear second-order PDE are classified as three types of problems: elliptic, hyperbolic, or parabolic. On the other hand, other systems are hardly amenable to the analytic

solution. They are possible to be interpreted by the methods such as separation of variables, weighted residual method, and spectral method [4-6]. However, numerical approach using discretization is mainly used to solve the DPS nowadays. Although these approaches require high computational load, their high-order function leads to an accurate solution.

The aim of this thesis is to propose discretization based numerical approach methodologies for three distributed parameter systems: 1) ambient air vaporizer, 2) continuous tubular crystallization process, and 3) high-pressure autoclave reactor for polymer production. Each system has a number of variables which are interdependent to each other and compared with high-order experiments dataset (or some arbitrary constants). On account of this comparison, the variables should be solved with high-order based method. By suggesting the systems that have been rarely treated in earlier papers, we hope this thesis contributes to development of a rigorous model for other complex distributed parameter systems.

2.2 Modeling methods

Distribution of properties such as fluids temperature, concentration can be derived from the partial differential equations which represent the behavior of systems. Although an exact solution of the systems is able to be obtained with the given initial function, solutions from the assumption cannot give any new information about the systems due to the dependence of the solution on the initial function. We adopt a finite difference based method to solve the complex systems described in the introduction. The discretization approach turns PDE

into either ODE or simultaneous algebraic equations by restricting functional space that uses control volume concept. Thus, distributions of objective variables of the systems can be obtained with sufficient computational power.

The concept of finite difference method is applied throughout the chapters in order to handle the distributed parameter systems in this thesis. In chapter 3, we handle the methodologies to analyze and model an air vaporizer system that uses air as the heat sink substance. The behavior of the frost and liquefied natural gas have a temporal and spatial characteristic. The frost layer grows and heat transfer efficiency of the vaporizer changes over operation time. In addition, the phase transition of liquefied natural gas to natural gas as the fluid runs is considered as a natural phenomenon in the vaporizer. From a chemical engineering perspective, the heat equation consisting of spatial variables and a time variable is mainly used to analyze the temperature change and phase transition. The representative equation is

$$\frac{\partial u}{\partial t} = \alpha\left(\frac{\partial^2 u}{\partial x^2} + \frac{\partial^2 u}{\partial y^2} + \frac{\partial^2 u}{\partial z^2}\right) \tag{2-2}$$

where α is diffusivity coefficient and the quantity of the parameter is thermal diffusivity of the medium. Because the equation is a partial differential equation, it should be approached with the discretization method to be numerically solved. In a cylindrical coordinate, the equation is modified to

$$\frac{\partial u}{\partial t} = \alpha\left(\frac{1}{r}\frac{\partial}{\partial r}\left(r\frac{\partial u}{\partial r}\right) + \frac{1}{r^2}\frac{\partial^2 u}{\partial \phi^2} + \frac{\partial^2 u}{\partial z^2}\right). \tag{2-3}$$

The heat equation represented under cylindrical coordination is appropriate to exhibit the distribution of temperature and heat flux through the vaporizer.

Additionally, we ignored the effect of heat profile on the tangential direction, which led the second term in Eq. 2-2 to be excluded from the analysis. This equation is not used as the way it is in Chapter 3. Rather, the whole is divided into numerous parts/categories in detail on temporal and spatial spaces with the concept of a control volume. Then, the continuous system represented by a partial differential equation is then separated into several algebraic equations which are iteratively solved with the corresponding boundary conditions. Although the solution from the discrete state cannot perfectly reflect the continuous characteristic of the complex system, this approach is sufficient to predict the frost layer growth and regasification rate roughly.

It is not common in the research field of crystallization that the system should be interpreted in temporal and spatial space. With the demand for higher efficiency crystallization process, the research in the batch process system has been practically displaced by continuous process system. Nowadays, there are a significant number of articles and papers about the novel continuous crystallization process. The lapse of time, which was not considered seriously in the conventional crystallization process, is regarded as the key factor in the new system. Since researchers and workers related to crystallization are unfamiliar to the continuous system, almost no research about modeling and verification of the system exists. The key equation in the crystallization process is

$$\frac{\partial n(L,t)}{\partial t} + G(t)\frac{\partial n(L,t)}{\partial L} = B - D \qquad (2\text{-}4)$$

where $n(L,t)$ represents the particle size distribution over operation time and $G(t)$, B and D indicate growth, birth, and death rate of the particle, respectively. This equation is conventionally called population balance equation because the solution is derived from the balance between values in multi-dimension including temporal and spatial spaces. In Chapter 4, the Eq. 2-4 will be simultaneously solved with other equations such as heat transfer equation and mass balance equation with one characteristic length. Transition of PDE into ODE with chain rule and forward difference method in one dimension enable interpreting the new crystallization system with ease.

Finally, in this thesis, we treat the polymerization of the monomers in a single-phase. Despite a long history of the polymerization process, there is no in-depth knowledge about the system. As a result of trial and error through which the polymer synthesis system has been developed, a few types of research about modeling and analysis are left now. With the advance of numerical analysis method such as computational fluid dynamics (CFD), the stirred flow in a polymer reactor can be solved. Since fluid dynamics is governed by Navier-Stokes equations: continuity, momentum and energy equations which are coupled and time-dependent, the equations should be solved simultaneously to get a flow pattern. A three-dimensional unsteady form of the equations include

$$\frac{\partial \rho}{\partial t} + \frac{\partial (\rho u)}{\partial x} + \frac{\partial (\rho v)}{\partial y} + \frac{\partial (\rho w)}{\partial z} = 0, \qquad (2\text{-}5)$$

$$\frac{\partial(\rho u)}{\partial t}+\frac{\partial(\rho u^2)}{\partial x}+\frac{\partial(\rho uv)}{\partial y}+\frac{\partial(\rho uw)}{\partial z} = -\frac{\partial p}{\partial x}+\frac{1}{Re_r}\left(\frac{\partial \tau_{xx}}{\partial x}+\frac{\partial \tau_{xy}}{\partial y}+\frac{\partial \tau_{xz}}{\partial z}\right), \tag{2-6}$$

$$\frac{\partial(\rho v)}{\partial t}+\frac{\partial(\rho uv)}{\partial x}+\frac{\partial(\rho v^2)}{\partial y}+\frac{\partial(\rho vw)}{\partial z} = -\frac{\partial p}{\partial y}+\frac{1}{Re_r}\left(\frac{\partial \tau_{xy}}{\partial x}+\frac{\partial \tau_{yy}}{\partial y}+\frac{\partial \tau_{yz}}{\partial z}\right), \tag{2-7}$$

$$\frac{\partial(\rho w)}{\partial t}+\frac{\partial(\rho uw)}{\partial x}+\frac{\partial(\rho vw)}{\partial y}+\frac{\partial(\rho w^2)}{\partial z} = -\frac{\partial p}{\partial z}+\frac{1}{Re_r}\left(\frac{\partial \tau_{xz}}{\partial x}+\frac{\partial \tau_{yz}}{\partial y}+\frac{\partial \tau_{zz}}{\partial z}\right), \tag{2-8}$$

$$\begin{aligned}&\frac{\partial(E_T)}{\partial t}+\frac{\partial(uE_T)}{\partial x}+\frac{\partial(vE_T)}{\partial y}+\frac{\partial(wE_T)}{\partial z}\\ &= -\frac{\partial(up)}{\partial x}-\frac{\partial(vp)}{\partial y}-\frac{\partial(wp)}{\partial z}-\frac{1}{Re_r Pr_r}\left(\frac{\partial q_x}{\partial x}+\frac{\partial q_y}{\partial y}+\frac{\partial q_z}{\partial z}\right)\\ &+\frac{1}{Re_r}\left[\frac{\partial}{\partial x}\left(u\tau_{xx}+v\tau_{xy}+w\tau_{xz}\right)+\frac{\partial}{\partial y}\left(u\tau_{xy}+v\tau_{yy}+w\tau_{yz}\right)\right.\\ &\left.+\frac{\partial}{\partial z}\left(u\tau_{xz}+v\tau_{yz}+w\tau_{zz}\right)\right].\end{aligned} \tag{2-9}$$

From Eq. 2-5 to Eq. 2-9, the equations describe the behavior of continuity, x-momentum, y-momentum, z-momentum, and energy of the fluid in a domain. Because the equations are complicatedly linked and share the variables, it is necessary for adequate comprehension about the system and calculus to solve a flow pattern. Moreover, the hydrodynamics solution is also coupled with polymerization kinetics to predict the performance of the polymer reactor. The CFD program and advanced ode solver make the problem-solving process easier. The interdependent equations will be efficiently solved with the finite volume method and multi-grid solver in the CFD program, and the advanced ode solver will be suitable for solving differential algebraic equation (DAE).

2.3 Conclusion

The complex systems treated in this thesis are entirely confined to a distributed parameter system. Other sides of the lumped parameter system, the variables and parameters are not easily determined by a few equations. Therefore, the concept of finite difference is mainly applied to simplify the target problems. The major hindrance of this approach is the requirement of enormous computational time and local optimal points during the parameter estimation process. Most of solving processes are performed in parallel computation and basic programming language. Further details about each system and solving approach are described in following chapters (from Chapter 3 to Chapter 5).

Chapter 3

Modeling and design of pilot-scale ambient air vaporizer

3.1 Introduction

Traditionally, liquefied natural gas (LNG) terminals have used a submerged combustion vaporizer (SCV), an open rack vaporizer (ORV), an intermediate fluid vaporizer (IFV), or other types of vaporizers such as the direct air vaporizers and the ambient air vaporizer (AAV), which have been used in small regasification plants [7]. Recently, with the shale gas revolution, numerous American import terminals are being converted into liquefaction and exporting terminals, and new projects for LNG receiving terminals are planned in countries such as Indonesia and Malaysia [8, 9]. In these equatorial regions, where the site ambient temperature stays high, LNG vaporizer systems with air heat sources can provide complete LNG vaporization duty. Hence, in these regions, AAVs will lower operating costs and fuel consumption as well as aid in reducing emissions harmful to the environment [10]. However, in recent years, as global environmental concerns have increased, AAVs have attracted attention in hot areas as well as in numerous other parts of the world. As an ORV uses seawater as the heat source, it exerts a negative influence on the marine ecosystem. In addition, an SCV uses the heat generated from the combustion of fuel, thereby contributing to pollution.

However, an AAV is an environment-friendly LNG vaporizer that utilizes heat absorbed from ambient air. In an AAV, LNG flows through the vertical

tubes arranged in parallel, and the air flows between the fins surrounding the tube. Moist air provides sensible heat (owing to temperature difference) to LNG, and it also provides latent heat that is manifested as the water vapor contained in moist air, Therefore, in an AAV, a complex phenomenon occurs in which heat transfer and mass transfer occur simultaneously. Because frost formation attributed to the condensation of water vapor is the main cause of this complicated phenomenon, understanding frost growth is essential for studying AAVs.

Frost is a porous material composed of ice and air. It is less dense than pure ice and exhibits high porosity, as it contains a significant quantity of air. Therefore, the frost accumulated on the surface of the AAV functions as a thermal resistance, which interferes with the heat transfer from the air to LNG because of low thermal conductivity; moreover, an AAV with high mechanical strength is required to support the weight of the accumulated frost [11-15]. In the case of an AAV with a forced draft fan, the frost is accumulated on the tubes and fins, which are located in the flow path; this restricts the airflow and increases pressure loss. The inlet of the air stream gradually becomes clogged, and the flow passage becomes narrower after a certain period. The resulting pressure drop and reduction in the amount and velocity of the air stream degrade the heat transfer performance of the AAV [15, 16]. Therefore, the target temperature of NG at the outlet cannot be attained Because of these problems, the AAV alternates between vaporization and defrosting operations.

Table 1. Previous research on frost growth and densification

Geometry	cold sink temp [°C]	relative humidity [%]	air velocity [m/s]	air temperature [°C]	researcher
flat surface	-15	50 ~ 80	0.5 ~ 2	25	Lee *et al.*[17]
flat surface	-20 ~ -15	50	1 ~ 2.5	5 ~ 10	Lee *et al.*[18]
fin-tube heat exchanger	-15	70	1.9	5	Yan *et al.*[19]
flat surface	-35 ~ -15	50 ~ 70	1 ~ 2.5	5 ~ 15	Yang *et al.*[20]
fin-tube heat exchanger	-33 ~ -30	60	1 ~ 1.5	8	Yang *et al.*[21]
flat surface	-15 ~ -5	50 ~ 80	0.7	16 ~ 22	Hermes *et al.*[22]
flat surface	-28 ~ -8.4	50 ~ 80	1.3 ~ 3	21 ~ 23	Kandula [23]
flat surface	-10	54 ~ 81	1.77	22	Kandula [24]
fin-tube heat exchanger	-30 ~ -20	70 ~ 90	0.76 ~ 2.08	3 ~ 15	Lee *et al.*[25]

The defrosting operation for melting the dense frost is started when the frost accumulation is excessive and the vaporizer is not performing satisfactorily. Hot gas is used as a heat source for defrosting; here, the NG from the outlet is heated through a separate heater and refer to the inlet. The hot gas entering the inlet flows through the tube and melts the frost layer.

To design an AAV, it is critical to determine the duration for which the vaporizer is likely to be operated with the NG of the outlet maintained at a stable temperature. However, it is challenging to predict the operating behavior of an AAV by straightforward calculation because complex phenomena including heat transfer and mass transfer occur. Therefore, modeling and simulation of an AAV are essential for predicting the frost accumulation during operation and heat transfer performance of the AAV over time. The model is also required to determine the duration for which the vaporizer will be operated successfully with the attainment of the target temperature of NG at the outlet.

As frost growth renders it challenging to predict the performance of AAVs, research in this area has continued for a long time. Previous studies can be divided into two areas: the first is related to frost growth and densification on a flat surface and fin-tube heat exchanger, and the second is related to an AAV. First, frost growth and densification have been studied through experiments and modeling. The history of research in these areas is summarized in Table 1. Each study was conducted on a flat surface or a fin-tube heat exchanger and under various cold sink temperatures, relative humidity conditions, air velocities, and air temperatures. Therefore, frost growth and densification studies can be divided into two groups according to the frosting structure.

The first group conducted a frost growth and densification study on a flat surface. Lee et al.[17] developed an analytical model for the frost formation on a cold flat surface by considering the molecular diffusion of water and the heat generation due to the sublimation of the water vapor in the frost layer and compared it with experimental data. Lee et al.[18] developed a mathematical model considering air flow and frost layer simultaneously and compared it with other analytical models and experimental data. Yang et al.[20] proposed a dimensionless correlation to predict the frost properties on a cold plate through experiments. Hermes et al.[22] proposed a mathematical model based on mass and energy balances, assuming that the frost is a porous medium and that the moist air of the frost surface is supersaturated. The model was validated through experiments. Kandula[23] proposed a one-dimensional frost growth and densification model in laminar flow considering the heat and mass diffusion in the frost layer and validated the model through various data. In addition, Kandula[24] conducted experiments on frost growth and densification in laminar flow under conditions of constant and variable humidity.

The second group studied frost growth and densification in a fin-tube heat exchanger. Yan et al.[19] examined the effects of air temperature, relative humidity, flow rate, refrigerant temperature, fin pitch, and row number on the heat transfer performance of a flat plate finned-tube heat exchanger through experiments. Yang et al.[21] proposed a mathematical model using empirical correlations of the heat transfer coefficients of the plate and tube surfaces and a diffusion equation for the frost layer. Lee et al.[25] conducted experiments on frost growth with varying relative humidity, air flow rate, inlet air temperature, and fin pitch for a spirally coiled circular fin-tube heat exchanger.

There is also an area of research that involved applying previous studies on frost to AAVs. Jeong et al.[26] collected and analyzed experimental data on LNG regasification for various air-heating vaporizers. There have also been attempts to identify the effect of frost on the performance of a vaporizer, using computational fluid dynamics (CFD). Three-dimensional CFD models were constructed and analyzed under various operating conditions. However, as the models were steady-state models, it is challenging to grasp trends over time. Moreover, as the frosting behavior was not included in the model, the model is inadequate for the design of an actual vaporizer (Jeong et al., Jeong et al., Liu et al.)[12, 27, 28]. Kuang et al.[11] used numerical models to predict the frosting behavior and thermal performance of a vaporizer. However, the model was validated by experimental data that was not obtained at cryogenic conditions. Liu et al.[13] also attempted to calculate the heat-transfer performance of a vaporizer using a numerical model. In the study, the dynamic heat transfer performance of an AAV was analyzed in natural convection. These previous studies did not consider frost growth in AAVs or developed models considering only natural convection of air. However, certain studies have been undertaken to increase the supply of NG using forced convection of air. Therefore, there is a need to model an AAV in forced convection; moreover, to model accurately, frost growth in an AAV must be considered. In recent years, there have been a number of cases in which apart from theoretical research, the vaporizer design is changed or the process is designed based on theoretical research. Bernert, Jr. et al.[29, 30] designed a frost-free vaporizer by applying a thermal insulation barrier and proposed a design to eliminate ground fog through the dispersion system. In addition, John Mak[31, 32] proposed the

optimization of power generation and defrosting and configuration of the AAV process.

This thesis presents a numerical model that reflects the frost deposited on tube and fin and heat transfer owing to the temperature difference between fluids. In the numerical model, heat and mass transfer are solved by simultaneous equations. Through the solution, time-varying simulation is performed for properties such as enthalpy and the density of each material. The thickness and density of the frost layer formed by the inflow of cryogenic LNG into a vaporizer are calculated, and the decrease in the heat-transfer performance of a vaporizer is predicted. The proposed model was validated by pilot-scale experimental data, and the error of the predicted value was approximately 5.5%. The experiment was conducted for six operation hours under conditions wherein the state of the ambient air and inlet LNG were varying. The NG temperature of the outlet, which is the most critical factor for performance evaluation, is obtained from the experiment. The thickness and density of frost and temperature profile of LNG in a vaporizer. tube with time and position are also predicted using simulation results. The simulation of frost growth at cryogenic conditions and that of the LNG profile in the tube provided insights into the design of AAVs for continuous operation. These insights include the fact that the relative humidity of air is the most critical factor in determining the growth of frost and that sensible heat contributes to total heat flux to a larger extent than latent heat and defrosting and configuration of the AAV process.

Additionally, a new optimization methodology using clusters with a feature extracted from a weather dataset is proposed. It is similar to multi-period optimization, but the time-series data are not divided according to a time interval. The feature used in the optimization is extracted from the DWT method, and the level of Haar function is selected using global sensitivity analysis of the features. Good-quality clusters are formed by the selected level of the Haar function using *k*-means clustering, and the centroids of the clusters represent the massive dataset. The feature vectors are used as the parameters in the numerical model of the vaporizer, and the objective function of optimization is the weighted sum of the results from the features. The optimal design structure from the multi-feature-based optimization method has robustness and effectiveness for various weather conditions and exhibits outstanding performance based on simulation data.

3.2 Modeling and analysis of frost growth in pilot-scale ambient air vaporizer

3.2.1 Ambient air vaporizer

An AAV is an eco-friendly type of vaporizer that uses an ambient air stream as a heat source. The vaporizer is more economical than other types of vaporizers such as the submerged combustion vaporizer (SCV) and intermediate fluid vaporizer (IFV), which use additional fluid and fuel to vaporize LNG [33, 34]. Sensible heat caused by the temperature difference between the air and LNG and latent heat of water vapor sublimation determines the performance of the vaporizer. Hence, weather conditions, including

temperature and humidity, are important factors in the design of the vaporizer structure [1, 7, 13, 15, 35]. Fig. 1 shows an AAV which is located at Korea Gas Corporation's Incheon production base [1]. In the target vaporizer, a fan located on the top of the equipment forces the air upward. The shroud surrounding the vaporizer prevents air stream leakage and intrusion of new air. The frost layer is gradually formed from the inlet of the cryogenic LNG, and the phenomenon spreads as time passes. When the accumulation of frost is great enough to interrupt heat exchange, the temperature of the vaporized natural gas fails to meet the target the temperature at the outlet. In other words, the uncertainty of the weather condition makes the performance of the vaporizer unpredictable, and therefore the design of a vaporizer that can operate for a long time has been a challenge.

(a)

(b)

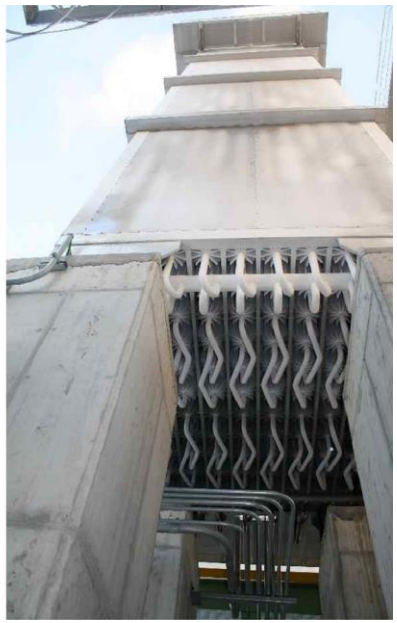

a) vaporizers surrounded by a shroud b) parallel fin tubes inside the vaporizer.

Figure 1. Photos of ambient air vaporizer.

3.2.2 Experimental measurement

The experiment was conducted using the vaporizer located at Korea Gas Corporation's Incheon production base. The dimensions of the AAV used in the experiment was designed to be 2.994 × 2.994 × 14.111 m and capable of handling 10 tons of LNG per hour. At the top of the vaporizer, a forced-air fan with a capacity of 4200 N m^3/min is installed to permit air to flow upward. A shroud is installed around the vaporizer such that the air flowing inside the vaporizer could not escape outward and flow straight. The LNG used in the experiment is a typical LNG consisting of 89.26% methane, 8.64% ethane, and the remaining as other hydrocarbons and nitrogen; it flows into the AAV at a temperature of −158 ºC and pressure of 7.55 MPa. The structural parameters and operating condition of the AAV used in the experiments are listed in Table 2.

Also, the experiment was conducted for 6 h and 20 min in winter daytime; the air temperature range was −4–+4 ºC and relative humidity range was 25−70%. The outlet temperature of the natural gas used to verify the numerical model was measured during the operation time. In the experiment, the geothermal energy, solar heat, fog, and scattering frost due to forced convection of air were uncontrollable factors. The effects of these factors were minimized by installing a shroud to prevent direct contact between the inside and outside of the vaporizer and measuring the air temperature and humidity at the inlet. Moreover, the pressure, temperature, and flow rate of the LNG entering the vaporizer were regulated within an error range of 7%. The type of thermocouple used to measure the temperature of fluids is K-type with an uncertainty of

±0.1 °C up to 600 °C, and the relative humidity of air was measured by a hygrometer with an uncertainty of 2%.

Fig. 2 shows the conceptual design of ambient air vaporizer. In the vaporizer covered with the shroud, there are 12 72 m-long stainless-steel tubes arranged in parallel, and each tube has a U-shaped bend at every 12 m. In addition, 12 aluminum fins surround the tube, and the accumulation of frost on the fins during operation lowers the vaporizer performance.

Table 2. Specification of AAV configuration and operating condition

structure	in parallel
AAV capacity	10 ton/h
fan capacity	4200 N m^3/min
LNG inlet temperature	-158 ºC
operation pressure	7.55 MPa g
number of tubes	24
number of fins on each tube	12
inner diameter of tube	10.5 mm
outer diameter of tube	15.7 mm
height of fin	86.0 mm
length of tube	72 m

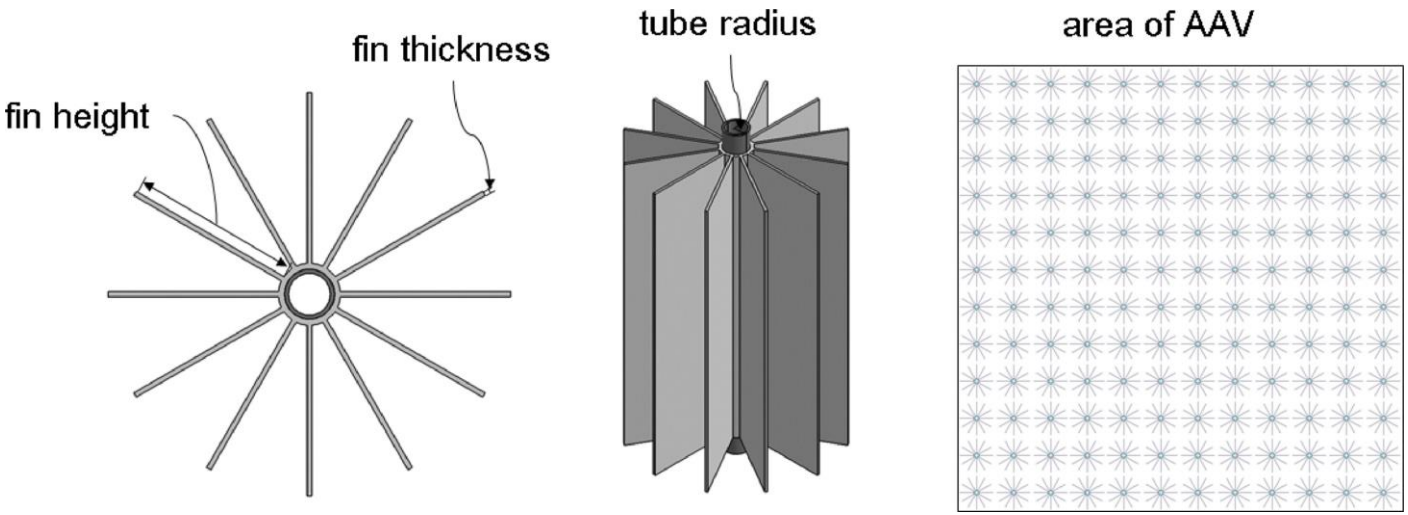

(a) viewed from the side (b) viewed from the below.

Figure 2. AAV structures used in actual experiment.

3.2.3 Numerical model of the vaporizer

The numerical model is based on the energy balance of the sensible heat generated by the temperature difference between the air flowing outside the fin and LNG flowing through the tube and the latent heat generated by the frost growth. The frost grows by mass transfer owing to the difference in density of the water vapor in the air and that of the water vapor on the surface of the fin or on the surface of the frost. The schematic of the AAV and frosting process is illustrated in Fig. 3. The entire length of the 72 m tube was divided into six sections (12 m per section). The six sections are arranged in parallel, with each section introducing fresh-air streams to exchange heat with the LNG. Each section is divided into smaller control volumes, and the frost growth and heat flux are predicted for each control volume. The heat flux and formation of the frost layer owing to the temperature difference between the LNG and air alter the enthalpy of the two materials, which results in a change in temperature. The components and conditions of the LNG and air used as the input in the numerical model are identical to those used in the pilot-scale experiment; moreover, the density of frost is obtained from Kandula [36].

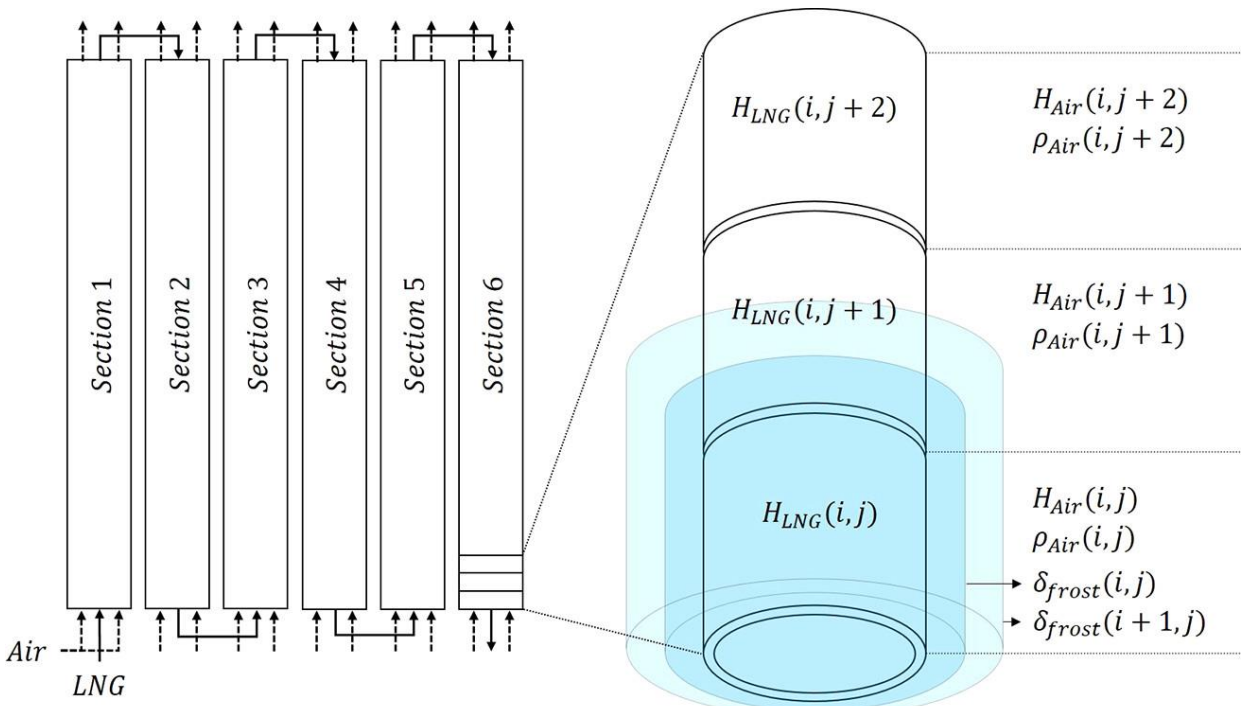

i, time step; j, position of control volume

Figure 3. Schematic diagram of AAV and frost processing.

3.2.3.1 Material properties

- **Air**

Air is used as the heat source in the vaporizer. To calculate the sensible heat and latent heat transferred from air to LNG, data on heat-related properties such as water vapor density and convective coefficient are essential. Water-vapor density is used to determine the amount of water vapor that can be condensed on the tube surface and the heat capacity of air. The empirical correlation of the density of water vapor contained in moist air was introduced by Saul [37], wherein the density of water vapor is determined from the temperature and relative humidity of the air stream. The heat capacity is used to calculate the enthalpy of air used as the heat source at a specific temperature. The formula for deriving the heat capacity of the air from this is as follows. The heat capacity of moist air is calculated by the density of the air and water vapor in it [38].

$$\mathrm{C}_{p,air} = 1005 + 1.82\left(\frac{\rho_{wv,air}}{\rho_{air}}\right) \tag{3-1}$$

The specific enthalpy of water vapor is derived from the temperature of the air stream and the heat capacity. Considering that the heat capacity of water vapor is 1.84 kJ/kg ºC and evaporation heat is 2501 kJ/kg, the equation for obtaining the enthalpy is expressed as follows:

$$H_{air} = \mathrm{C}_{p,air}\mathrm{T} + x[1.84\mathrm{T} + 2501] \tag{3-2}$$

where H is the specific enthalpy [kJ/kg], x is the mass fraction of water vapor [kg/kg], and T is the temperature [ºC].

The convective heat transfer coefficient is directly related to the velocity of the fluid. In the case of air, this coefficient is established to be 3−11 W/(m^2·K) for natural convection and 11−85 W/(m^2·K) for forced convection [39]. The pilot-scale experiment was conducted under forced convection with an airflow rate of 12 m/s, and the coefficient was specified as 32 W/(m^2·K) in the model [40]. The convective mass transfer coefficient, which was obtained by the Chilton−Colburn analogy [41], increases in proportion to the heat transfer coefficient; however, it also depends on the density of air and the heat capacity.

$$\mathrm{h}_m = \frac{\mathrm{h}_{air}}{\rho_{air}\mathrm{C}_{p,air}\mathrm{Le}^{2/3}} \tag{3-3}$$

where Le is the Lewis number, which is the ratio of thermal diffusivity to mass diffusivity. Mass diffusivity of the water vapor in moist air was obtained by Le Gall [42].

$$\mathrm{D}_{mass} = 1.451 \times 10^{-4}\frac{T^{1.72}}{P} \tag{3-4}$$

and the thermal diffusivity of air is determined from [43] as $\mathrm{D}_{\mathrm{thermal}} = 0.000019$

- **Frost**

The frost is accumulated by the condensation of the water vapor in the air by the cryogenic LNG. The thermal conductivity of frost is significantly smaller than that of aluminum fins, thus reducing the heat-transfer performance of a vaporizer. The thermal conductivity of frost is expressed by the equation concerning the density of frost [44]:

$$k_{fr} = 0.132 + 3.13 \times 10^{-4}\rho_{fr} + 1.6 \times 10^{-7}\rho_{fr}^2 \quad (50 < \rho_{fr} < 400) \tag{3-5}$$

where ρ_{fr} is the frost density, which can be calculated by the temperature of the frost surface and wall surface. The form of the frost density correlation is as follows:

$$\frac{\rho_{fr}}{\rho_{ice}} = 0.5\theta\exp\{-[0.376 + 1.5(1-\theta)](1-\varepsilon^{0.5})\} \tag{3-6}$$

where θ is the dimensionless frost surface temperature, and ε is the Reynolds number divided by the critical Reynolds number for a laminar-turbulent transition.

The thickness of the frost is derived by simultaneously calculating the mass flux of the water vapor from the air stream to the saturated frost surface and the frost density correlation. The process is described in section 3.2.3.2.

- **LNG**

The thermal and transport properties of materials at cryogenic temperatures are not constant. Therefore, it is critical to have an understanding of the temperature variation of the properties for an efficient analysis of a thermal system [45]. For calculating the properties of LNG mixtures, the Peng–Robinson equation of state in Aspen HYSYS, which provides an enhanced method for a rigorous treatment of hydrocarbon systems. The convective heat transfer coefficient and enthalpy of LNG were calculated by conducting a case study on temperature with the mixture. For the values obtained, convective heat transfer is represented by a Gaussian function and enthalpy by a third-degree polynomial equation.

3.2.3.2 Main Equations

The numerical model consists of a coupled heat transfer model and a mass transfer model. The heat transfer model simulates the heat transfer phenomena caused by the difference in temperature between LNG and air. In the mass transfer model, the process of frost growth and densification is simulated as mass transfer caused by the difference in densities of water vapor.

The two transfer models were solved numerically using Matlab. The 72 m-long AAV was modeled by dividing it into six sections (12 m per section). The assumptions used to simplify the model are as follows: (1) In all the sections, the air and LNG flows are cocurrent. (2) The frost thickness does not affect air velocity. (3) The density of frost is uniform. (4) The moist air on the frost surface is saturated.

The numerical model handles the data in a matrix form. The rows and columns of the matrix represent the time step and position of the control volume, respectively. The case study to determine the magnitude of the time step and control volume was carried out for 0.2−10 s and 0.05−1 m, respectively. When the magnitudes of the parameters were lower than specific values, the model exhibited similar results with less than 1% difference. Considering the stability of the results and calculation time, the values of the parameters are specified as 1 s and 0.2 m. Dynamic-operation-condition data such as the relative humidity and temperature of air and the flow rate and temperature of LNG was used as input. For simulation, the properties of the material, which were mentioned in section 3.2.3.1, were also prepared. The properties of air, LNG, and frost were updated over time and position, and the heat transfer areas of the fin, tube, and

frost surface were also changed according to frost accumulation. Table 3 summarizes the ranges of the variated parameters used in the proposed dynamic numerical method.

Table 3. Ranges of variated parameters

relative humidity of air [%]	25.5 ~ 62.4
water-vapor density of air [kg/m^3]	0.00092 ~ 0.0026
air temperature [^{o}C]	-4.2 ~ 3.2
LNG temperature [^{o}C]	-151.5 ~ -10.5
LNG flow rate [ton/h]	9.8 ~ 10.7
frost density [kg/m^3]	38.6 ~ 201.9
frost thickness [m]	0.00001 ~ 0.009
frost surface temperature [^{o}C]	-106.8 ~ -7.8
heat flux of sensible heat [W]	15.7 ~ 869.9
heat flux of latent heat [W]	0 ~ 46.0
convective mass transfer coeff. [m]	0.0198 ~ 0.0280

- **Coupled heat transfer model**

The total heat flux is the sum of the sensible heat and latent heat, which is expressed as Eq. 3-7. The sensible heat caused by the temperature difference between the air stream and LNG is the main heat source. The overall heat transfer coefficient, which was determined based on the material of the structure and the heat transfer area, also affects sensible heat flux.

$$\mathrm{Q}_{total} = \mathrm{Q}_{sen} + \mathrm{Q}_{lat} \tag{3-7}$$

$$\mathrm{Q}_{sen} = \mathrm{UA}(\mathrm{T}_{air} - \mathrm{T}_{lng}) \tag{3-8}$$

$$\mathrm{UA} = \frac{1}{\frac{1}{h_{lng}\mathrm{A_i}} + \frac{\Delta \mathrm{r}_{sus}}{k_{sus}A_1} + \frac{\Delta \mathrm{r}_{fin}}{k_{fin}\mathrm{A}_2} + \frac{\Delta \mathrm{r}_{fr}}{k_{fr}\mathrm{A}_3} + \frac{1}{h_{air}\mathrm{A}_0}} \tag{3-9}$$

Here, the subscripts under A indicate the heat transfer area or contact area between materials. The latent heat released as water changes phase from gas to solid was calculated by the heat of sublimation and the water-vapor mass flux from the air stream to the frost surface:

$$\mathrm{Q}_{lat} = h_{sv}(m \times \mathrm{A}_3) \tag{3-10}$$

where m is the amount of frost condensed over time on the frost surface. The value of m is calculated in the mass transfer model.

The enthalpy of LNG is affected by the total heat flux because both the sensible heat caused by air convection in the vicinity of the tube and the latent heat from the condensation of water vapor is transferred to the natural gas through the frost layer. However, the enthalpy of air is affected by the sensible heat, which is absorbed by the LNG and the water vapor condensed on the frost surface.

$$\Delta \mathrm{H}_{lng(i,j)} = \frac{\Delta Q_{total(i,j)}}{\mathrm{F}_{lng}}, \Delta \mathrm{H}_{air(i,j)} = \frac{\Delta Q_{sen}}{F_{air}} \quad (3\text{-}11)$$

$$\mathrm{H}_{lng(i,j+1)} = \mathrm{H}_{lng(i,j)} + \Delta \mathrm{H}_{lng(i,j)} \quad (3\text{-}12)$$

$$\mathrm{H}_{air(i,j+1)} = \mathrm{H}_{air(i,j)} + \Delta \mathrm{H}_{air(i,j)} \quad (3\text{-}13)$$

- **Mass transfer model**

In the mass transfer model, the amount of frost deposited over time on the vaporizer tube and the fin surface is calculated. The driving force for the mass

transfer is the difference between the density of water vapor in the air flowing around the fin and that of the water vapor at the previously condensed frost surface. The density of water vapor at the surface around the fin can be derived from the surface temperature, which can be calculated using the sensible heat in the coupled heat transfer model.

$$\mathrm{T}_{fs} = \mathrm{T}_{air} - \frac{\mathrm{Q}_{sen}}{h_{air}\mathrm{A}_0} \quad (3\text{-}14)$$

$$m = h_m(\rho_{air} - \rho_{fs}) \quad (3\text{-}15)$$

Using the value of T_{fs} derived from the above equation in eq 2-14, we can calculate the density of the frost accumulated on the fin surface [44].

The frost growth rate is derived by dividing the mass flux of water vapor from the air to the frost, by the frost density calculated above:

$$\Delta\delta_{fr} = \frac{m}{\rho_{fr}}\Delta t \quad (3\text{-}16)$$

The reduction in the water-vapor density of air equals the mass transfer rate. If the water vapor density in the vicinity of the frost surface is higher than that in the air stream, mass transfer does not occur on the frost layer.

$$\rho_{wv,air(i,j+1)} = \rho_{wv,air(i,j)} - \frac{m\mathrm{A}_0}{\dot{V}_{air}}\Delta t \qquad (3\text{-}17)$$

Fig. 4 illustrates the flowchart of the numerical model. The model iterates the calculations up to the target time-step and control volume, and all the data are saved in the matrix form.

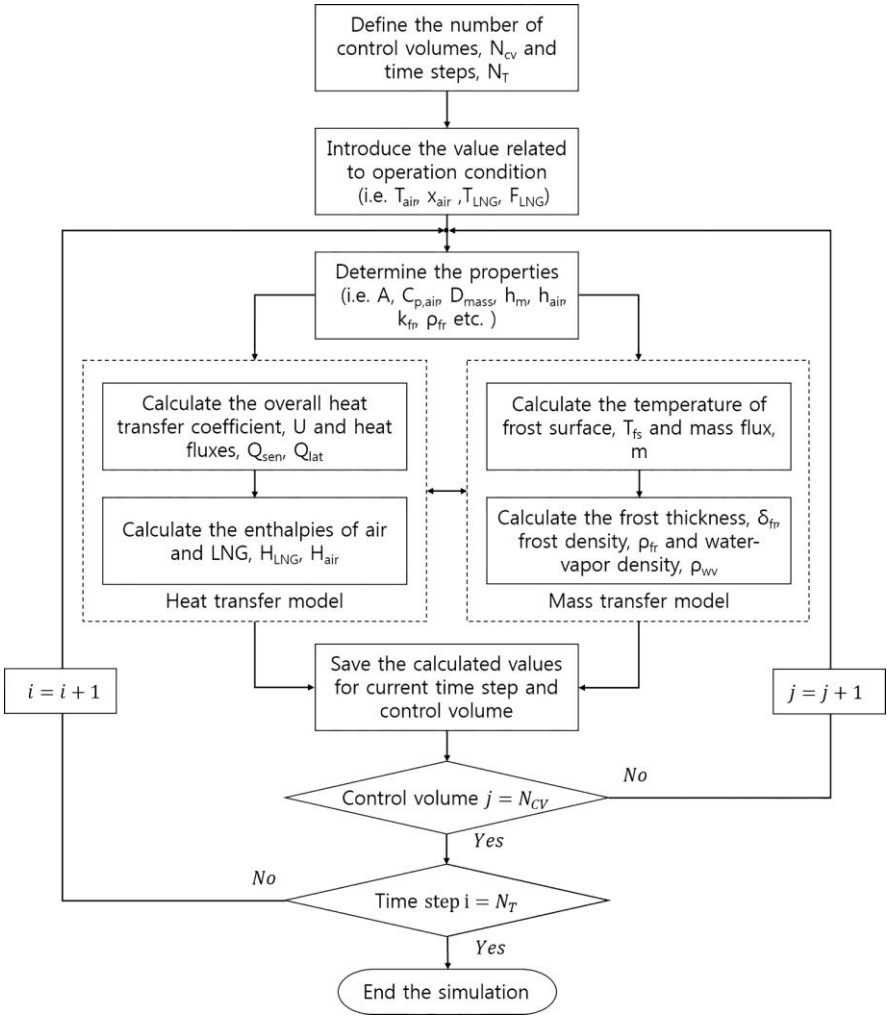

Figure 4. Flowchart of numerical model.

3.2.4 Result and discussion

Once vaporization begins, the water vapor in the air stream is condensed by the flow of cryogenic LNG, and the frost layer grows rapidly. Therefore, the performance of the vaporizer decreases with time, and the temperature of the discharged NG gradually decreases. Through the model developed in this study, the aspect of frost distribution over the entire vaporizer over time can be calculated. Based on the calculated frost thickness and density, the dynamic heat transfer performance of the vaporizer can be derived, and the temperature change of discharged NG can be predicted. The predicted results were compared with the AAV operation record of approximately 6 h, and the accuracy of the model was validated. Moreover, through the validated model, key parameters affecting the operation of the vaporizer were derived using sensitivity analysis.

3.2.4.1 Validation with pilot-scale experimental data

To validate the accuracy of the AAV model developed in this study, the calculated results of the numerical model was compared with the pilot-scale experimental data. As the performance of the pilot-scale AAV is affected by atmospheric conditions and the thermal properties of the LNG entering the unit, these values should be used as the input of the model. Through experiments, the relative humidity and temperature of ambient air, flow rate and temperature of LNG into the AAV, and temperature of discharged NG flow are measured. Owing to the nature of the forced draft vaporizer, the frost-related properties could not be measured because the shroud surrounds the vaporizer. Therefore, in this study, frost growth and fluid temperature are interlocked based on a time-

varying simulation and validated only for one variable, “NG outlet temperature”. During the experiment, the temperature of the ambient air was constant; however, there was a significant change in humidity. This change in humidity hinders the prediction of frost thickness and density over time because it is directly related to the amount of water vapor in the air. The changes in temperature and in flow at the LNG inlet are marginal compared to the humidity of the ambient air.

Fig. 5 compares the pilot-plant data with the model predicted values. At the beginning of operation, the temperature of the NG discharged from the AAV was approximately −10 °C. As the frost began to accumulate at the vicinity of the LNG inlet, the heat transfer efficiency of the vaporizer decreased. After 6 h, the NG temperature at the outlet decreased to −30 °C, and the operation was terminated.

The mean absolute error (MAE) between the pilot-scale data and model-predicted values was 5.5%, which implies that the current model provides satisfactorily accurate prediction of the NG outlet temperature of the pilot-scale AAV. At the x-axis values of three and six, the difference between the two graphs accounts for a large part of the error. First, the output temperature sharply decreases at 3 h of operation. As shown in Fig. 6 (b), the LNG flow rate increased by 7% compared to the initial value, and the residence time of fluid become shorter, which reduces heat transfer efficiency. The error indicates that the numerical model overestimates the effect of flow rate on the heat transfer performance of the vaporizer. After 6 h, the predicted value is larger than the plant data, and the error continues to increase. As the operation continues, the

performance of the vaporizer decreases after some hours, which is related to the frost growth. The space between the tubes arranged in parallel in the vaporizer is constant, and the frost growth clogs the space. The clogging of the space implies that the passage for air is narrowed, which degrades the heat exchange performance of the vaporizer. In the proposed model, the equation for evaluating such physical effects was excluded; therefore, the error was not corrected.

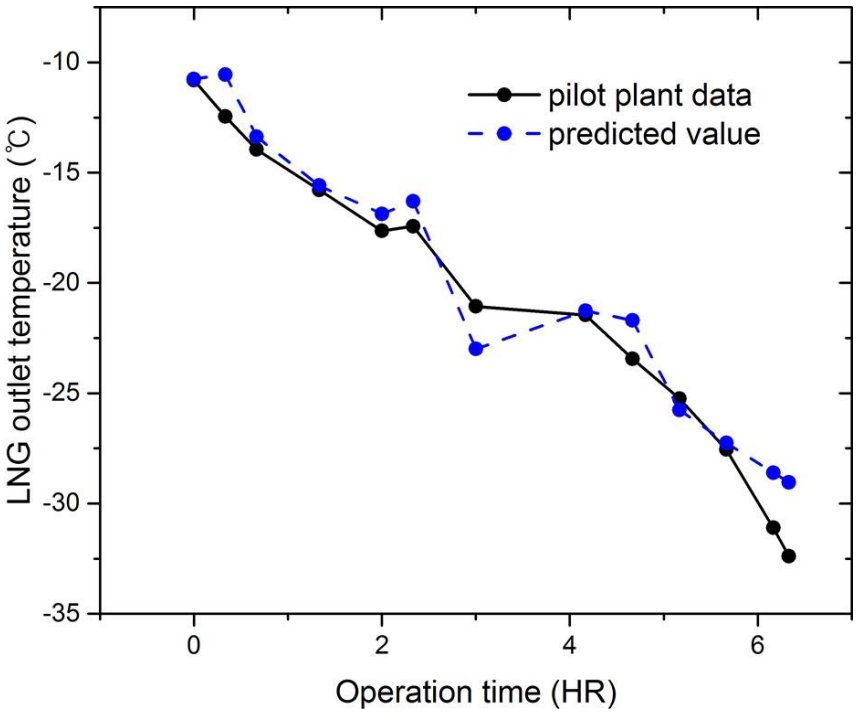

Figure 5. Comparison between the numerical predicted value and pilot-plant data.

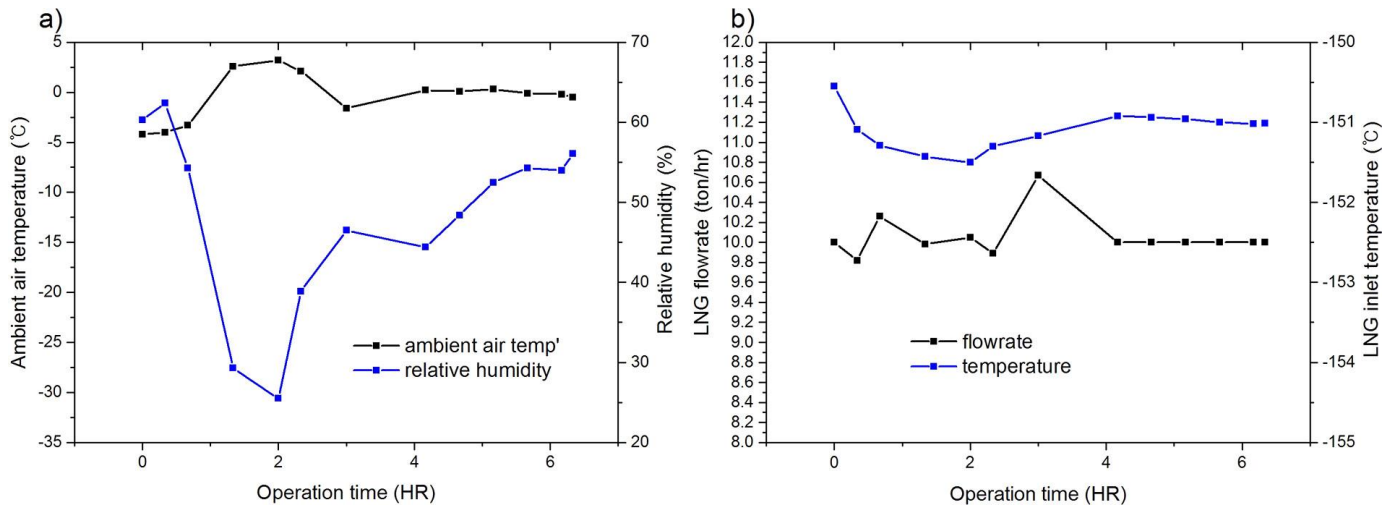

a) ambient air temperature and relative humidity b) LNG flow rate and temperature.

Figure 6. Operation condition of air and LNG over time.

3.2.4.2 Frost formation and vaporizer heat performance

The proposed numerical model was validated by comparing the LNG temperature data of the pilot-scale AAV with the predicted values. In the model, frost thickness and density are predicted according to the position and time as well as the temperature of LNG at the outlet obtained from the input data used for the validation. The position implies the distance from the inlet through which LNG enters, and the time is the time elapsed since the flow rate of LNG reached 10 ton/h. The parameters of LNG and air used in the simulations are temperature, flow rate and composition, enthalpy, and heat transfer coefficient. In addition, in the case of air, additional parameters such as mass transfer coefficient and diffusivity are considered. Lastly, thermal conductivity, density, thickness, and surface temperature were used as frost parameters.

Fig. 7 (a) shows the value of two types of heat flux over time. At the beginning of operation, sensible heat contributes 12 times more than latent heat to the total heat flux. However, sensible heat decreases over time because the frost deposited on the tube interferes with heat exchange. Moreover, the formation of the frost layer permitted cryogenic LNG to be distributed throughout the tube, and the water vapor in the air stream could be condensed on a larger surface area; this contributed to the increase in latent heat over time. Therefore, after 6 h, sensible heat is 7.5 times larger than latent heat.

Fig. 6 (b) shows that the slope of the graph decreases rapidly as the position of LNG increases. The slope represents an increased temperature per unit distance, and a large slope generally indicates that a large quantity of heat is

absorbed. As the fluid flows, the temperature difference between the LNG in the tube and the air reduces, and the heat flow from the air to the LNG decreases gradually. Furthermore, as frost accumulates over time, the temperature of LNG in the vicinity of the outlet reduces to approximately −35 °C after 6 h of operation. Owing to the low temperature of LNG, the frost begins to accumulate around the tube, and the heat transfer efficiency of the vaporizer at the inlet reduces. However, as the amount of frost accumulation at the rear part is marginal in comparison to that at the front part, it is feasible to compensate the heat transfer efficiency at the front part. Therefore, the temperature change of LNG at the outlet is smaller than predicted, as shown in Fig. 7 (b). LNG flows through a total length of 72 m and exchanges heat with fresh air at every 12 m. Fig. 7 (c) and (d) exhibits the frost thickness and density by dividing into six sections based on the location of entry of fresh air. It is observed that LNG is already vaporized in the preceding section as frost is not accumulated at the fifth and sixth sections after 2 h. Additionally, as the temperature of LNG increases while flowing through the tube, the density of water vapor on frost surface at the rear portion of the vaporizer is higher than the front density and mass transfer is further suppressed, so that the thickness of frost is thinner. For the frost density, the correlation proposed by Kandula [36] was used. The frost density is determined by dimensionless frost surface temperature ($\theta = \frac{T_{fs}-T_w}{T_m-T_w}$ where T_m, melting temperature; T_w, tube wall temperature). The frost density increases with θ determined by T_{fs} and T_w. When the thickness exceeds a certain value, T_{fs} becomes constant and frost density is determined by $T_w(\cong T_{LNG})$, which be seen in the 4 and 6 h case of Fig. 7 (d). In the 2 h case, the frost is not thick enough, so the difference between temperature of frost

surface and wall is similar in all sections. This makes it difficult to find a difference in frost density of the graph.

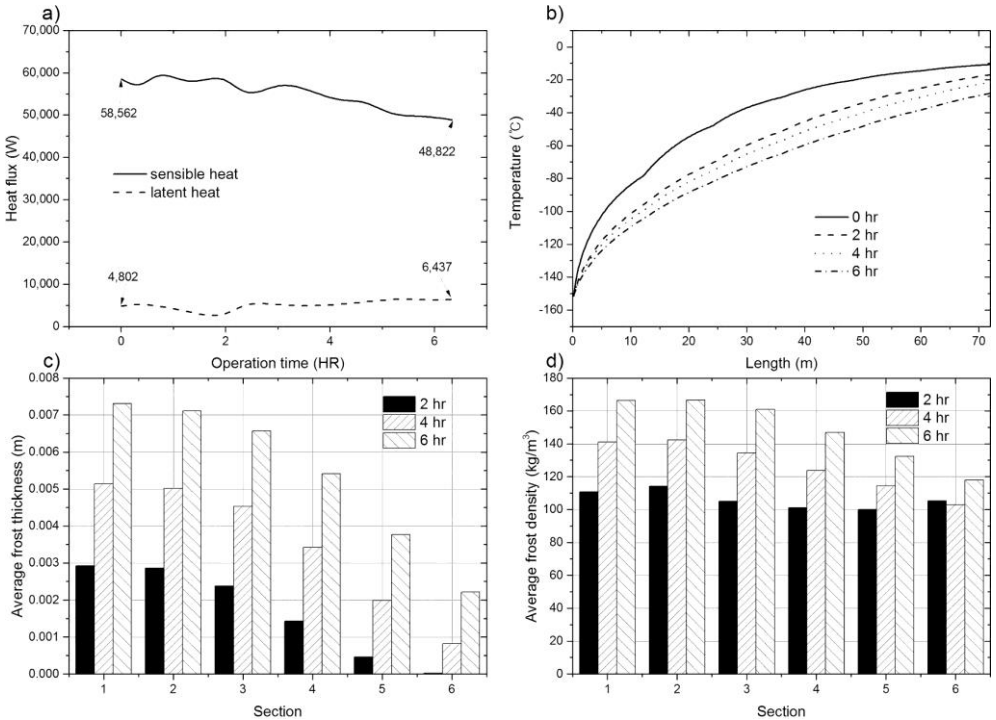

a) sensible heat and latent heat in total heat flux. b) LNG temperature according to the flow length of the fluid in tube. c) average frost thickness distribution over time in each section. d) average frost density distribution over time in each section.

Figure 7. Simulation results from experimental condition.

3.2.4.3 Factors of air that affect thermal performance of vaporizer

The thermal performance of the AAV is directly affected by atmospheric conditions such as humidity, temperature, and velocity of ambient air. These factors affect the amount of heat transferred from air to LNG and the growth rate of frost on the tube and fin. Based on the proposed model, numerical calculations were conducted, and the variations in the LNG outlet temperature and of the frost thickness with operation time under various conditions of the ambient air were determined. Fig. 8 shows the simulation results of the numerical model for the relative humidity of air. In the simulation, air-stream temperature and velocity are assumed to be 0 ºC and 10 m/s, respectively. As the relative humidity of air increases to 30%, 50%, 70%, and 100%, the average frost thickness increases to 0.0032, 0.0055, 0.0078, and 0.0109 m after 10 h of operation. This implies that the average frost thickness tends to increase with the relative humidity. Moreover, the higher the relative humidity of air, the higher the rate of LNG outlet temperature decline over time. The high humidity implies that the density of water vapor in the air stream is high, which accelerates mass transfer and frost growth rate. When the relative humidity is 100%, the AAV initially ensures high heat transfer performance; however, because of high frost growth rate, operation stability and durability cannot be guaranteed. As the relative humidity decreases, the growth rate of frost also declines; therefore, the rate of LNG outlet temperature decline over time also decreases. In the 30% case, the graph is the reverse of the other case after 4 h because the frost layer, which increases the thermal resistance, is thinly formed owing to the low water-vapor density.

The temperature of ambient air is also a critical factor affecting the performance of an AAV. Notwithstanding whether the relative humidity of air is high, if the temperature of the air is low, the amount of water vapor that can be saturated is marginal. Fig. 9 shows the calculation results for the temperature of ambient air when the relative humidity of air is 50% and the velocity of air is 10 m/s. In Fig. 9 (b), it is observed that the difference between the average frost thickness at 20 ºC and that at 40 ºC is marginal. This is explained using the results of the case wherein the ambient temperature is 40 ºC (Fig. 8 (a)). The fact that the LNG outlet temperature remains constant at 36.5 ºC. Notwithstanding, the long operation time indicates that frost is not uniformly accumulated in the whole length of tube and that it is formed only in the front part of the tube, where vaporization occurs and cryogenic LNG flows in. In the rear part of the tube, there is no accumulation of frost owing to the flow of the vaporized NG. However, as shown in Fig. 9 (a), the outlet temperature is not constant at 20 ºC air, and frost is formed over the whole tube; therefore, the average frost thickness is calculated to be high. When the temperature of the ambient air is below 40 ºC, the LNG outlet temperature decreases over time. In the case of −20 ºC, the temperature of the LNG is not changed significantly because the amount of saturated water vapor is low and the frost accumulates negligibly notwithstanding the length of time elapsed. This demonstrates that the LNG outlet temperature is stable over time only if the temperature of the ambient air is adequately high to accelerate the vaporization of LNG at the front of the tube or if the temperature of the air is very low and the amount of frost accumulated on the tube is marginal.

The relative humidity and temperature of the ambient air are determined by the climate of the region where the LNG regasification facilities are located; however, in the case of a forced draft vaporizer, the velocity of air is related to the capacity of the fan. The larger the capacity of the fan generating the upward draft air, the higher the heat transfer performance of the vaporizer. However, the capacity of the fan should be carefully determined as the high air velocity causes problems such as noise, vibration, and pressure decline. As the velocity of air increases, the amount of air that exchanges heat with LNG increases, and the convective heat transfer coefficient increases, thus enhancing the heat transfer performance of the AAV. When the velocity of air is 10 m/s, the temperature of LNG at the outlet reduces by 5.5 ºC from the initial value after 10 h of operation, whereas it declines by 7.5 ºC when the velocity of air is 14 m/s, as shown in Fig. 10 (a). Moreover, notwithstanding whether the velocity of air is changed, the average frost thickness does not change significantly, as shown in Fig. 10 (b). This implies that the increase in the velocity of the air stream contributes more to the convective heat transfer rate than mass transfer rate.

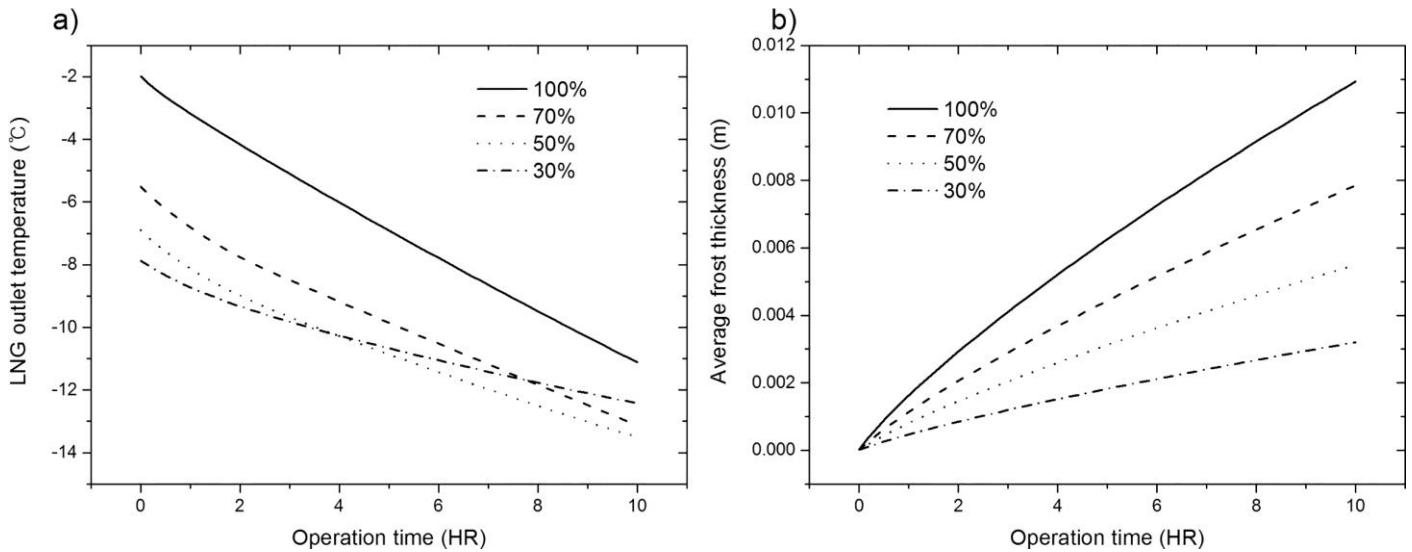

$\mathbf{T}_{air}$ = 0 ºC and $\mathbf{v}_{air}$ = 10 m/s.

Figure 8. Change of LNG outlet temperature and average frost thickness with operation time at different relative humidity of air.

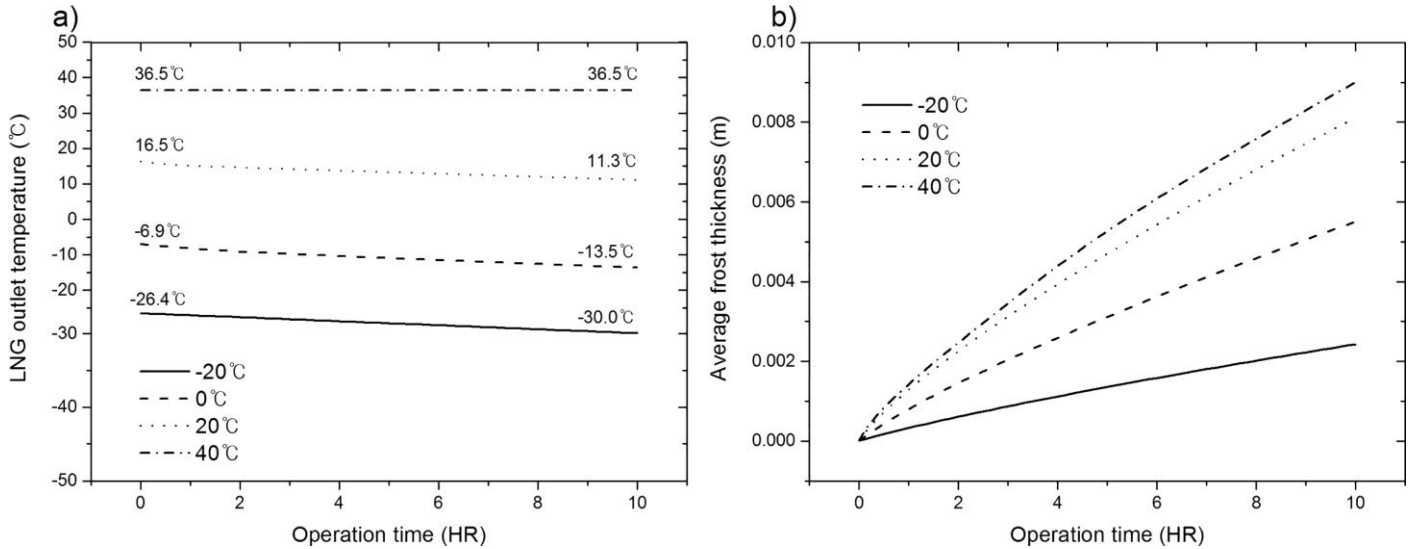

Relative humidity = 50% and $\mathbf{v}_{air}$ = 10 m/s.

Figure 9. Change of LNG outlet temperature and average frost thickness with operation time at different ambient air temperature.

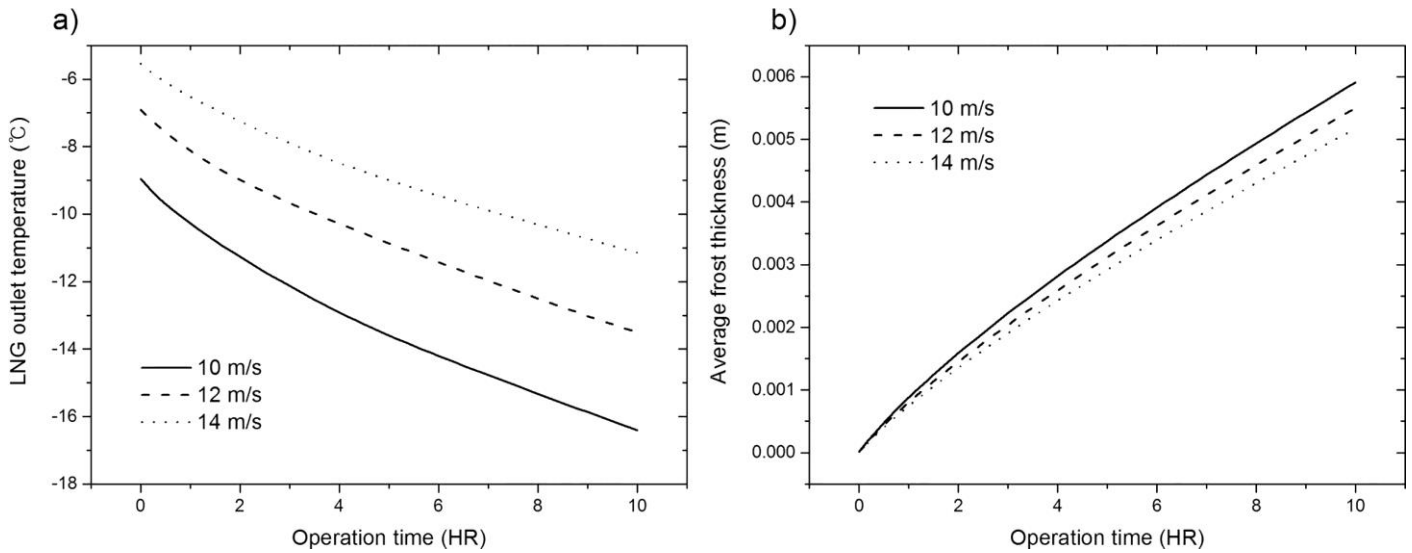

Relative humidity = 50% and $\mathbf{T}_{air}$ = 0 °C.

Figure 10. Change of LNG outlet temperature and average frost thickness with operation time at velocity of air stream.

3.3 Robust design of ambient air vaporizer based on time-series clustering

3.3.1 Background

Robust design or flexible design should be used when uncertainty is contained in parameters or when there are disturbances that affect the process and the equipment dynamically. Thus, an optimal design maximizes performance and minimizes the variance induced by uncertainty propagation from uncertain parameters. Therefore, to solve this kind of design problem, a new methodology is needed that quantitatively evaluates or considers parameter uncertainty or disturbances. In the field of process systems engineering, several methods for solving these problems have been developed. The first one is called multi-period optimization. In general, when time-series data affect system performance, the time-series data are divided according to time intervals, and each representative value is determined. Then, the objective function is obtained by weighted sum and optimized. This method is often used to obtain flexible design by reflecting variables that vary with time, such as utility cost, seasonal climate change, and oil well life cycle [46-54]. In addition, through worst-case analysis, which is often used in traditional robust design and optimization, the optimal design is equivalent to a conservative design that does not fail any external changes. The design is performed in the area that can produce the worst result among the constraints that can affect the design so that the system can operate robustly regardless of the value of the parameter [55-59]. Another method is stochastic design and optimization. In this framework, the objective function is expressed as expected value and variance so that it is

advantageous to find the optimal point more flexibly than worst-case analysis. In particular, as an uncertainty quantification methodology such as polynomial chaos expansion (PCE) is developed, it is actively applied to reactor design and control fields [60-62]. Appropriate pre-processing of time-series data is also required for analyzing the performance of the vaporizer and estimating robust optimal design because the unpredictable and frequently changing characteristics of actual weather data make the problem difficult. The choice of an appropriate time-series data representation method may improve the accuracy and quality of clusters [63]. Adaptive and non-adaptive data representation methods are performed to analyze time-series data. The adaptive data representation method estimates each time-series well, but it is inappropriate for comparing several time-series because it adjusts parameters to minimize the global reconstruction error. The method includes piecewise polynomial interpolation (PPI), piecewise polynomial regression (PPR), piecewise linear approximation (PLA), singular-value decomposition (SVD), symbolic aggregate approximation (SAX), and others [64-66]. The non-adaptive data method is suitable for time-series with a fixed size, and comparison of several time-series data is uncomplicated [67]. The discrete Fourier transform (DFT) and discrete wavelet transform (DWT) are the most popular methods for dimensionality reduction and feature extraction[68-70]. The DWT has a few bene- fits compared to DFT. The DWT is more accurate and efficient in terms of computation, and it can consider localized information better [71, 72]. The clustering method for massive datasets works well with the feature vector of lower dimension from the application of the wavelet method.

The cluster quality is better and computation time is shorter than clusters from the raw dataset [73].

The temperature of the frost surface is an important factor because the mass transfer rate is derived from the difference of the density of water vapor in the air and frost surface as shown in Eq. 3-18.

$$m = h_m(\rho_{air} - \rho_{fs}) \tag{3-18}$$

The water vapor condensation results in the growth of frost thickness for given time step size. For more details on the model and numerical algorithm, see [1]. In this study, the model mentioned above is represented as a function f which is defined as

$$Operation\ \ time = f(\vec{y}, C_i) \tag{3-19}$$

where y is the design variables, which are fan capacity, tube radius, fin height, and fin thickness, and C_i is the reconstructed weather condition using the inverse Haar transform from centroids representing the clusters i. The design parameters like fan capacity, fin thickness and fin height and time-series weather conditions are provided as the input parameter of the function which returns the maximum operation time of the AAV. All of the above equations are included and is used to evaluate the dynamic thermal performance of the vaporizer.

3.3.2 Trend of time-series weather conditions

In an operation where external conditions such as the weather are unrestrained, it is difficult to predict the exact performance of the process. To overcome this hurdle, time-series analysis of the external conditions and appropriate reflection are an integral part of the equipment and process design. In this study, it was assumed that the vaporizer is operated under the one-year climate of Yeonsu-gu Incheon, Republic of Korea, in 2016. The one-year data provided by the Korea Meteorological Administration (KMA) consists of the temperature and relative humidity of the air recorded each minute, so the full data size is 366 (day) ×1440 (min) ×2 (type: temperature, relative humidity). Fig. 11 shows the trends of one-year temperature and relative humidity in a day, month, and year from below. The temperature fluctuated in the range from −20 ºC to 40 ºC, and the value of relative humidity ranged from 0% to 100%. In the trend of the weather conditions of one day from midnight to midnight, the temperature is high during the daytime. In contrast, the relative humidity is low and varies more than temperature at the same time. The weather trend of a month shows the uncertainty and unpredictability of the time-series data in an inadequate scale. However, in a year-scale graph, it is relatively easy to identify the trend of data. From May to September, the overall temperature and relative humidity remain higher than those conditions for the other months. The three graphs in Fig. 11 suggest that time-series data should be analyzed in various scales from low frequency to high frequency.

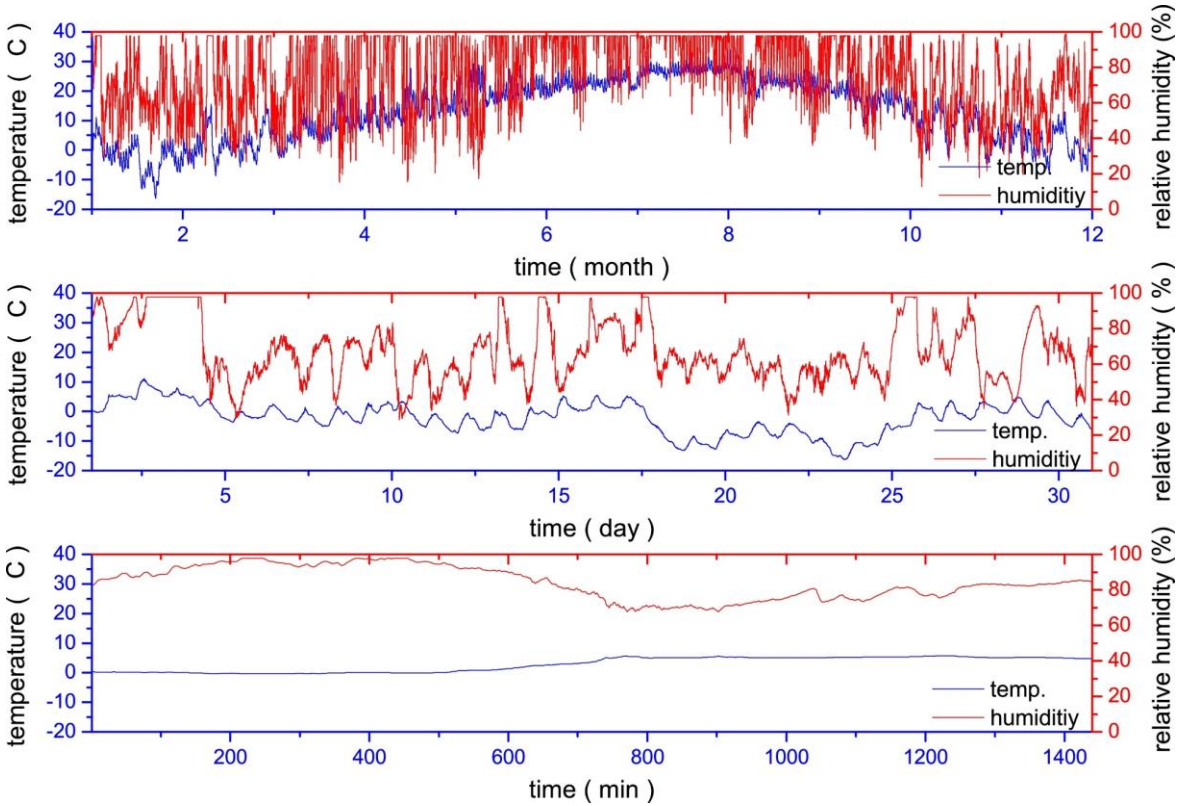

Figure 11. Weather conditions at three different scales.

3.3.3 Optimization of AAV structures under time-series weather conditions

3.3.3.1 Methodology

In Fig. 12, an overview of the proposed methodology for the time-series related design optimization problem is described in the form of a flowchart. The main purpose of the methodology is obtaining a robust design. If we optimize the AAV structure with air temperature and relative humidity fixed, then it does not guarantee robust performance against seasonal climate change because the performance depends strongly on the fluctuation of air temperature and relative humidity. It is possible to consider the one-year real climate data and calculate the vaporizer performance on the basis of the numerical model through one-year simulation. However, this method is computationally expensive (approximately 5 h for function evaluation). Thus, we attempt to extract the representative features by using a wavelet transform and *k*-means clustering. The two-step method of feature extraction can reduce the computational cost and better reflects the time-series trend. This square-integrable orthonormal system can be used to understand the localized features of the time-series signal easily. Notably, we perform the global sensitivity analysis of each level of Haar function, and clustering based on the highest Haar impact level for k-means clustering. The extracted feature provides more promising clusters than clustering with raw climate data, as explained in Section 3.3.4.2. After that, centroids of each cluster are transformed by inverse Haar transform to obtain the representative air temperature and relative humidity profile. Finally, global derivative-free optimization is performed with the representative air

temperature and relative humidity profile by using the DIviding hyper-RECTangle (DIRECT) algorithm. The final performance of the robust optimal AAV design is validated by a one-year simulation.

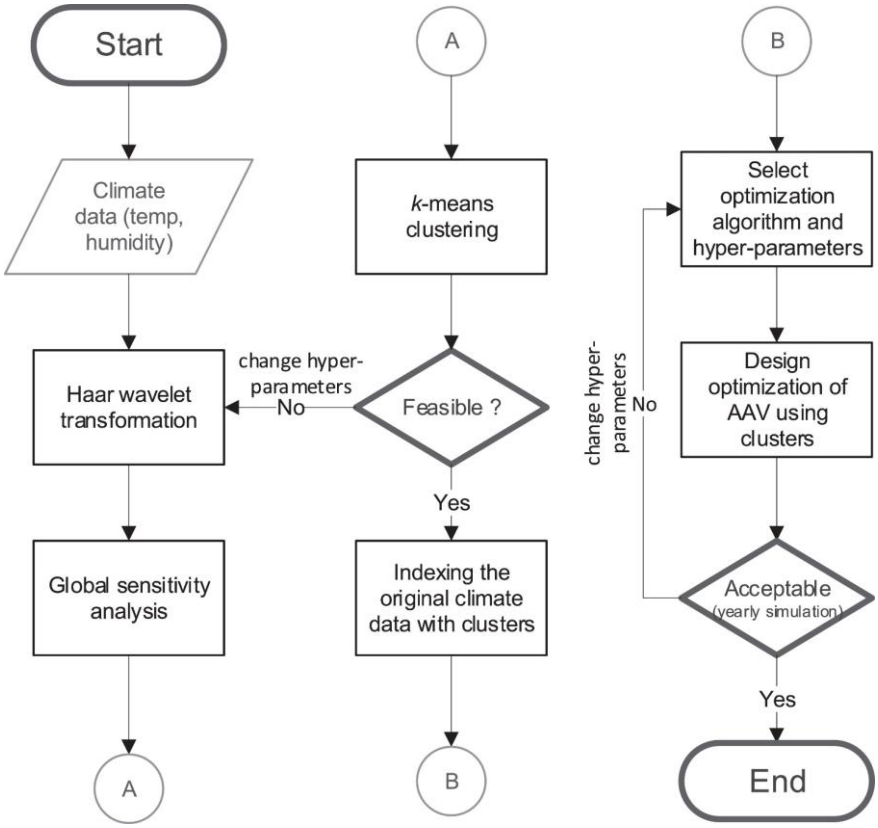

Data pre-processing with Haar wavelet transformation, global sensitivity analysis, *k*-means clustering, and derivative-free optimization.

Figure 12. Flowchart for the proposed methodology.

3.3.3.2 Haar wavelet transform

The Haar wavelet transform is the most basic form of the DWT, where the wavelets are discretely sampled. Unlike the short-time Fourier transform, the wavelet transform treats frequency in a logarithmic way and captures the property of time-frequency localization of the time-series data [74]. The Haar function is the simplest and oldest orthonormal wavelet, and has the advantages of reduced computational and memory requirements [75]. To apply the Haar wavelet transform, the one-year time-series was separated into 366 one-day time-series data $\vec{X}^p = \{x_1, x_2, \dots, x_n\}$ for $p \in [1, 2, \dots, 366]$, where x can be the value of temperature or relative humid- ity. Each day's data can be respectively decomposed into an approximation part $\vec{\mathrm{A}}_\mathrm{j} = \{a_j^1, a_j^2, \dots, a_j^{\frac{n}{2^J}}\}$ and a detail part $\vec{\mathrm{D}}_\mathrm{j} = \{d_j^1, d_j^2, \dots, d_j^{\frac{n}{2^J}}\}$, where j is the level of Haar function. The *i*th element of $\vec{\mathrm{A}}_j$ and $\vec{\mathrm{D}}_j$ are

$$a_j^i = \frac{1}{\sqrt{2}}\left(a_{j-1}^{2i-1} + a_{j-1}^{2i}\right), i \in \left[1, 2, \dots, \frac{\mathrm{n}}{2^j}\right] \quad (3\text{-}20)$$

$$d_j^i = \frac{1}{\sqrt{2}}\left(a_{j-1}^{2i-1} - a_{j-1}^{2i}\right), i \in \left[1, 2, \dots, \frac{\mathrm{n}}{2^j}\right] \quad (3\text{-}21)$$

where $j \in [1, 2, 3, \dots, \mathrm{J}]$ is the level of Haar function mentioned above and J is the maximum level of Haar function whose value is an integer. Hence, the length of the input time-series data should be an integer power of 2, and padding zeros to the end of $\vec{\mathrm{X}}$ and $\vec{\mathrm{Y}}$ was implemented for satisfying the condition. In this study, the length of the input time-series data is 2048 (211) because the

length of day's data is 1440, which means the range of level of Haar function is from 1 to 11. At the first level, a_1^i and d_1^i are represented by

$$a_1^i = \frac{1}{\sqrt{2}}\left(x^{2i-1} + x^{2i}\right), i \in \left[1, 2, \dots, \frac{\mathrm{n}}{2^j}\right] \quad (3\text{-}22)$$

$$d_1^i = \frac{1}{\sqrt{2}}\left(a_{j-1}^{2i-1} - a_{j-1}^{2i}\right), i \in \left[1, 2, \dots, \frac{\mathrm{n}}{2^j}\right] \quad (3\text{-}23)$$

The original time-series data $\vec{\mathrm{X}}^{\mathrm{p}}$ can be represented as a series $\left\{\vec{\mathrm{D}}_1, \vec{\mathrm{D}}_2, \dots, \vec{\mathrm{D}}_{\mathrm{J}}, \vec{\mathrm{A}}_{\mathrm{J}}\right\}$. Fig. 13 shows the results of the decomposition of a day of data from level 1 to 11. The 12 small graphs show the detail part in all levels and the approximation part in level J in the order $\left\{\vec{\mathrm{D}}_1, \vec{\mathrm{D}}_2, \dots, \vec{\mathrm{D}}_{\mathrm{J}}, \vec{\mathrm{A}}_{\mathrm{J}}\right\}$. At a low level, the detail part of the wavelet shows the high-frequency characteristics of the weather. The long trend of weather is shown at the high level, where a few values represent the day data set. Furthermore, at the section of sensitivity analysis and clustering, level of Haar function for $j = J$ is defined as $\vec{\mathrm{D}}_{\mathrm{J}} + \vec{\mathrm{A}}_{\mathrm{J}}$ because it is impossible to decompose $\vec{\mathrm{A}}_{\mathrm{J}}$ and they are the same level of Haar. Thus, 11 level of Haar means $\vec{\mathrm{D}}_{\mathrm{J}} + \vec{\mathrm{A}}_{\mathrm{J}}$ in this thesis.

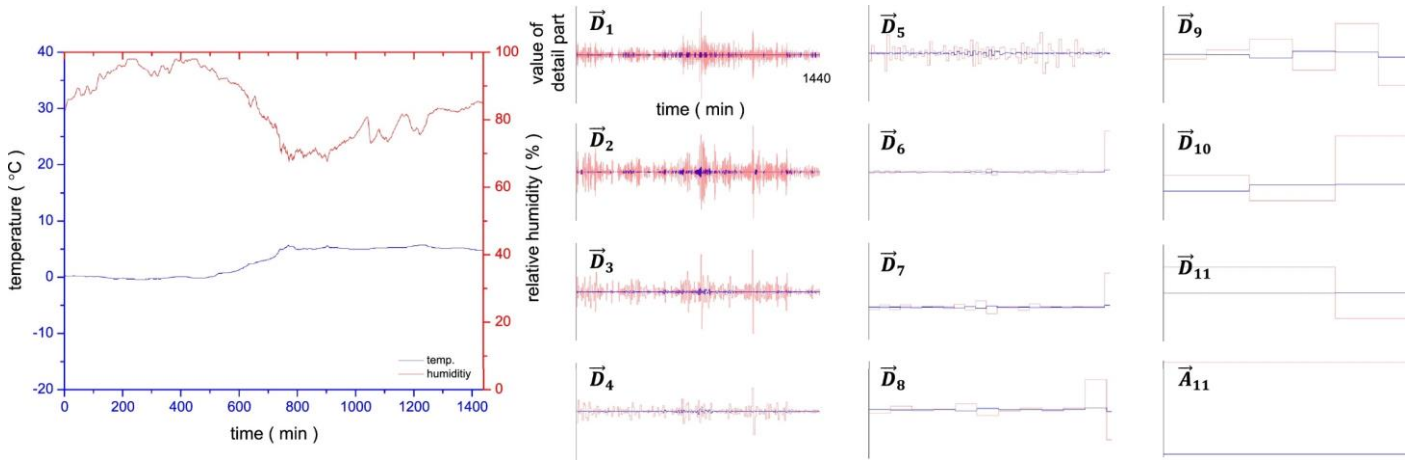

In the right panel of this graph, x-axis is the time of day, while y-axis is the value of detail part in all levels and approximation part in level 11. Additionally, the scale of y-axis is different at each level.

Figure 13. Example of Haar wavelet transforms at different levels for Jan. 1, 2016.

3.3.3.3 Sensitivity analysis

For quantifying the contribution of each level of Haar function to the total variance of the output such as the performance of AAV, variance-based global sensitivity analysis can be applied. After quantifying the sensitivity, we can perform the time-series clustering with the highest sensitive level of Haar function. The level of Haar function global sensitivity can be easily obtained because of its orthonormal characteristics. However, the global sensitivity of AAV performance, which is an objective function of the optimization, is difficult to calculate because of its non-linear relationship between wavelet function and performance. Thus, global sensitivity indices for non-linear mathematical models and their Monte Carlo estimates [76] is employed by using global sensitivity analysis toolbox (GSAT) implemented in Matlab [77]. The Sobol' definition of global sensitivity indices what we used in this section are defined as follows.

$$\mathrm{S}_{i_1 \dots i_1} = \frac{\mathrm{D}^{var}_{i_1 \dots i_s}}{\mathrm{D}^{var}} \tag{3-24}$$

$$\mathrm{D}^{var}_{i_1 \dots i_s} = \int_0^1 f^2_{i_1 \dots i_s} dx_{i_1 \dots i_s} \tag{3-25}$$

$$\mathrm{D}^{var} = \int_0^1 f^2(X) dX - f_0^2 = \sum_{s=1}^{n} \sum_{i_1 < \cdots < i_s} \mathrm{D}^{\mathrm{var}}_{i_1 \dots i_s} \tag{3-26}$$

where $1 \le i_1 < \cdots < i_S \le n$; D^{var} means the total variance of the output; $\mathrm{D}^{var}_{i_1 \dots i_s}$ is the variance of the output of a set of variables $x_{i_1 \dots i_s}$. For calculating decomposition result of analysis of variance(ANOVA) [78, 79], the evaluation of 2^{n} integrals are required. Thus, sensitivity indices for subsets of variables which is defined as

$$S_{\alpha} = \frac{D_{\alpha}^{var}}{D^{var}} \tag{3-27}$$

$$D_{\alpha}^{var} = \sum_{s=1}^{m} \sum_{(i_1 < \cdots < i_s) \epsilon K} D_{i_1 \ldots i_s}^{\mathrm{var}} \tag{3-28}$$

where $1 \leq m \leq n-1; i_1, \ldots, i_m \in M_{\alpha}$. Moreover, subset's D_{α}^{var} can be directly calculated by original non-linear function $f(X)$ with quasi-Monte Carlo methods. Detailed procedures and math- ematical formulations are shown in various literature[76-79]. We set the variable $X = \{x_{i_1}, x_{i_2}, \ldots, x_{i_n}\}$ as each level of Haar function and is de- fined in n-dimensional unit hypercube where n equals to 11. To transform define space of X to n-dimensional unit hypercube, we mapped the $p \in [1, 2, \ldots, 366]$ space to $I \in [0.1]$ space and put pre-calculated value of level of Haar function. For example, $X = \{1, 0, \ldots, 0.5\}$ then $\vec{D}_1$ is defined as the value of the day 366, $\vec{D}_2$ is defined as the value of day 1, and $\vec{D}_{11}$ is defined as the value of day 183. Thus, we can perform the level of Haar function global sensitivity analysis in 11-dimensional unit hypercube with quasi-Monte Carlo sampling technique. Furthermore, we suggest the sensitivity function $S_{p,q,j}$, which represents which level of Haar function most affects the objective function. Unless global sensitivity index, it can show the local sensitivity and we can visualize it with heap map. The equation is

$$S_{p,q,j} = \left[\begin{array}{c} f\left(\vec{y}_o, \sum_{i=J\setminus\{j\}} \left(\frac{1}{N(p \in q)} \sum_{k=p \in q} \vec{D}_i^k + \vec{A}_J^k \right) + \vec{D}_j^p \right) \\ -f\left(\vec{y}_o, \sum_{i=J} \left(\frac{1}{N(p \in q)} \sum_{k=p \in q} \vec{D}_i^k + \vec{A}_J^k \right) \right) \end{array} \right]^2 \tag{3-29}$$

p=1, 2, …, 366; q=Jan, Feb, …, Dec; j=1, 2, …, 11

where p means the day, q means the month, j means the level of Haar function, and f is the objective function, which calculates the operation time of AAV with original design parameters $\vec{y}_o$, and time-series wavelet function. J equals to 11. Because it is not proper to make an artificial air temperature and relative humidity profile, $S_{p,q,j}$ is calculated by real climate data within the set of p and q . First, all one-day air temperature and relative humidity profiles are decomposed by a wavelet function D_j^p, for the jth level and pth day. The first term of Eq. 3-29 is the calculation of the objective function with the monthly averaged wavelet function for levels except the jth level. For the jth level, we can select the specific day's wavelet function in terms of p. The second term of Eq. 3-29 is the function with the monthly average wavelet function for all levels. In the case of the second term, the jth level is also calculated by the monthly averaged value with selected value q. The proposed equation is sufficient to evaluate which level of the Haar function is influential to the objective function; the results of the evaluation of the global sensitivity indices and the proposed sensitivity function $S_{p,q,j}$ are discussed in Section 3.3.4.1.

3.3.3.4 *k*-means clustering

k-means clustering is one of the simplest unsupervised learning algorithms; it is easily programmed and computationally economical [80]. Clustering with features extracted from the wavelet function improves the execution time and clustering quality [73]. The matrix of weather conditions including temperature and relative humidity for a day is one sample, whose size is [1440×2]. The

samples already undergo the process of feature extraction using global sensitivity analysis of various levels. The feature size is less than the original data matrix, and it also reflects the trend of the weather conditions. When data $\{d_1, d_2, \dots, d_n\}$ are given at the level L of Haar function, *k*-means clustering divides the n observations into k sets $H = \{h_1, h_2, \dots, h_n\}$ to minimize the variance.

$$\underset{H}{argmin} \sum_{i=1}^{k} \sum_{d \in h_i} \|d - \mu_i\|^2 \qquad (3\text{-}30)$$

where μ_i is the mean of the points in h_i. The method was implemented using the MATLAB toolbox. k-means clustering with the features requires a low computational load and improves the quality of clusters with time-series data, as explained in Section 3.3.4.2. The *k*-means clustering algorithm used in the study is shown in Table 4.

Table 4. *k*-means clustering algorithm.

Define the value of *k*
Initial group centroids are randomly generated
while termination conditions are activated
Assign each object to the group with the nearest centroid
The group centroids are recalculated.
end while

3.3.3.5 Optimization formulation

This optimization problem is a class of derivative-free, unconstrained, bounded, and non-linear programming. The optimization problem arises in the reformulation of the constrained optimization problem where the constraints are replaced with a penalty term in the objective function. The number of design variables is only four, and the objective function of the problem is the weighted sum of operation time at the representative weather of the clusters. The optimization formula is

$$\max_{\vec{y}} \sum_{i=1}^{k} w_i f(\vec{y}, C_i) \qquad \text{(3-31)}$$
$$\text{Subject to } \mathrm{LB}_j \leq y_j \leq \mathrm{UB}_j$$

where k is the number of clusters; w_i is the weight of the cluster, which is the proportion of the class in the whole data set; and $f(\vec{y}, C_i)$ is the operation time which is defined in Eq. 3-18. LB and UB are lower bound and upper bound, respectively, and the values of the bounds are shown in Table 5. The function f used in Eq. 3-28 is the same function which was used at Section 3.3.3.2 for global sensitivity analysis and the definition of the function is exactly explained at Section 3.3.1. It is highly recommended to solve this class of optimization problem by a global optimization algorithm, the DIRECT algorithm [81, 82]. In general, DIRECT guarantees the global optimum of a function will be found within a given search area with enough function evaluations. Moreover, DIRECT is a deterministic solver that does not need to consider reproducibility, and it has fewer parameters than meta-heuristic algorithms such as the genetic algorithm (GA). More details on the theoretical background are available in [83].

Table 5. Optimization results.

design variables	unit	lower bounds	upper bounds	wavelet-based clusters					non-wavelet based clusters					multi-period		original
				4	8	12	16	20	4	8	12	16	20	4	12	-
fan capacity	m^3	2000	6000	4273	5528	5986	4658	4504	3719	3929	5564	3942	3988	3890	3184	4000
tube radius	m	0.005	0.02	0.02	0.02	0.02	0.02	0.02	0.02	0.02	0.013	0.02	0.02	0.02	0.02	0.0105
fin height	m	0.05	0.15	0.097	0.117	0.115	0.099	0.095	0.101	0.110	0.056	0.111	0.112	0.114	0.102	0.086
fin thickness	m	0.001	0.005	0.005	0.005	0.005	0.005	0.005	0.005	0.005	0.005	0.005	0.005	0.005	0.005	0.0025
performance*				+22.63	+22.57	+22.92	+22.82	+22.79	+21.52	+21.04	+17.11	+20.92	+20.95	+20.79	+20.00	-

*The performance is $\frac{\text{The objective value(operation time) of optimal design}}{\text{The objective value of original design (real AAV)}} \times 100$ at the same one-year dataset which was used for feature extraction (Fig. 11). The value of performance shows the effect of feature extraction and cluster size on the robust design. (The simulations of wavelet-based clusters and non-wavelet based clusters are performed in 4, 8, 12, 16, and 20 clusters. In addition, multi-period simulation is performed in 4, 12 intervals.)

3.3.4 Results and discussion

3.3.4.1 Sensitivity analysis

First, we used the Sobol' indices to calculate the global sensitivity index and find out which levels in each level of Haar function have the greatest effect on the AAV performance due to the weather conditions changing over a year. It can be inferred that a highly sensitive level of Haar function includes the important feature of time-series data through the objective function what we want to optimize. Fig. 14 shows that the higher the level, the greater the sensitivity to AAV performance. This is because the higher level is better for more macroscopic temperature and humidity behavior and the lower level is for higher frequency characteristics. Moreover, the proposed local sensitivity function $S_{p,q,j}$ is described in Fig. 15. Level 11 and the summer season (Jun.–Aug.) have the highest effect on global sensitivity. Notably, level 11 can extract the daily feature of temperature and relative humidity in terms of wavelength (day and night sequence is the representative feature of the daily feature). Both sensitivity analyzes conclude that level 11 has the greatest impact, which is consistent across the season. Therefore, it is reasonable to proceed with time-series k-means clustering using the 11th level of Haar function.

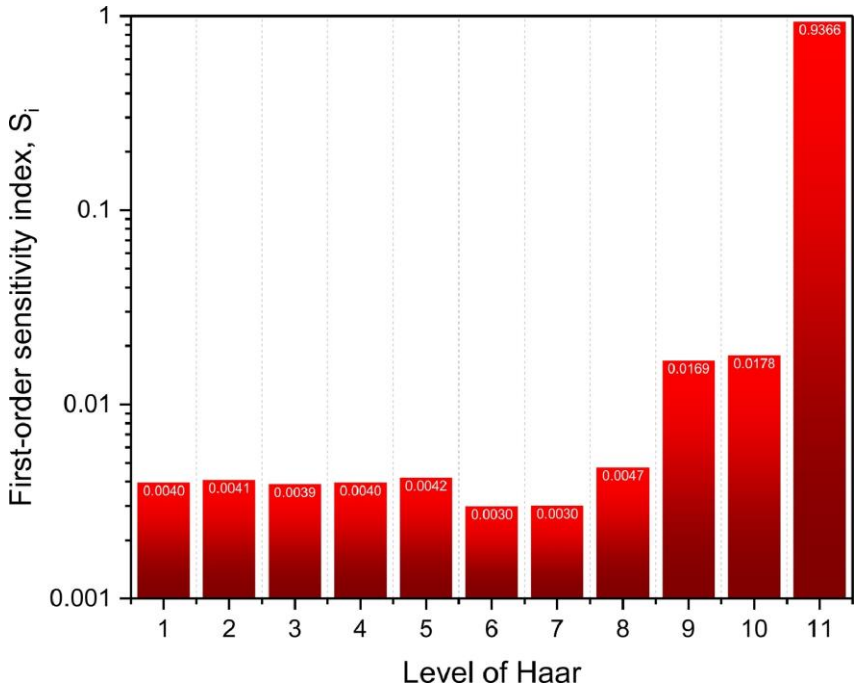

Figure 14. The first-order global sensitivity index of each level of Haar function by Sobol' indices.

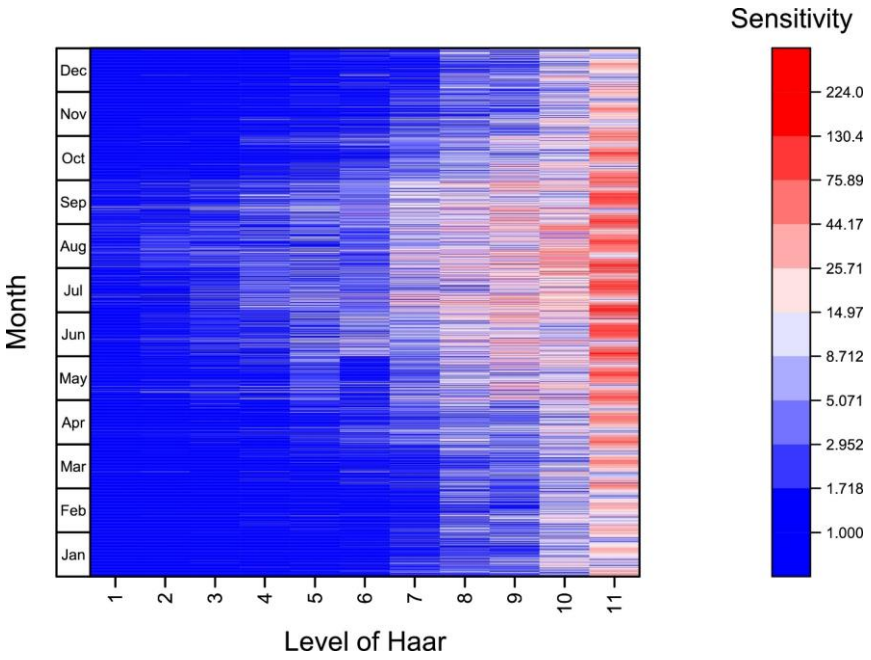

By fixing the other sets of the level of Haar function.

Figure 15. Monthly sensitivity heat map of the level of Haar function.

3.3.4.2 *k*-means clustering for the Haar wavelet function

Clustering with the level 11 of Haar function, whose data size is 1/1440 that of the original time-series data, requires low computing time that is approximately an order of magnitude smaller. The result of the k-means clustering for the Haar wavelet feature is shown in Fig. 16. To visualize the Haar wavelet function for relative humidity and temperature, the inverse Haar transform is performed after clustering the level 11 of Haar function. Each dot in Fig. 16(a) represents the day (366 data) feature represented by the level 11 Haar function, and because one-day data includes 1440 min data, 1440 data are encoded in each dot by using the level 11 of Haar function. To compare with the original data, we indexed the original data (minute-based data) with the clusters at level 11 and visualized them in Fig. 16(b). Much of the data are overlapped because the one-day data include day and night characteristics. Although representative values of temperature and relative humidity can be fixed in a scalar for optimization boundary conditions from non-wavelet based clusters, it is not proper for obtaining a robust AAV design. The representative values are not exact features because the temperature changes by more than 10 °C per day and the relative humidity also changes greatly. Therefore, we can obtain a more robust design by using the climate time-series obtained by inverse Haar transform on the basis of the centroid of the Haar cluster level, which is a more proper feature of temperature and relative humidity.

A representative one-day climate profile from the cluster centroids is shown in Fig. 17. The four feature vectors represent a year of weather conditions.

Because the features were extracted from the level 11 of Haar function, the profiles reflect a trend of a day. The profiles have the lowest humidity at approximately 800 min and the highest temperature at approximately 800 min. The similarity of an overall slope shows the trend. However, the average values of the graph are all different, which was caused by the different climatic conditions in each season. The *k*-means clustering can reflect the trend of climate change over a year. The four graphs respectively reflect the seasonal climate of a year, and each graph has the trend of a day, as shown in the slope.

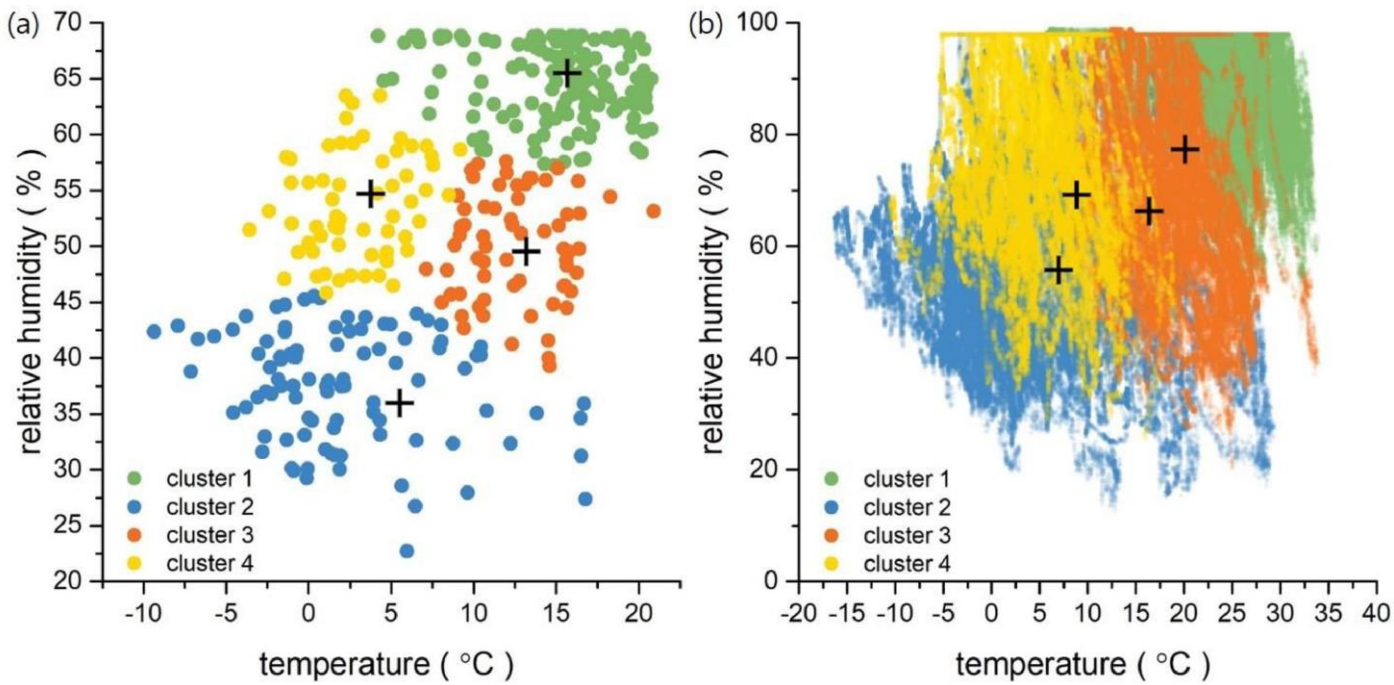

a) clustering at level 11 of Haar function, and b) inverse Haar transform clusters of the original data.

Figure 16. Result of *k*-means clustering for a Haar wavelet feature with four clusters.

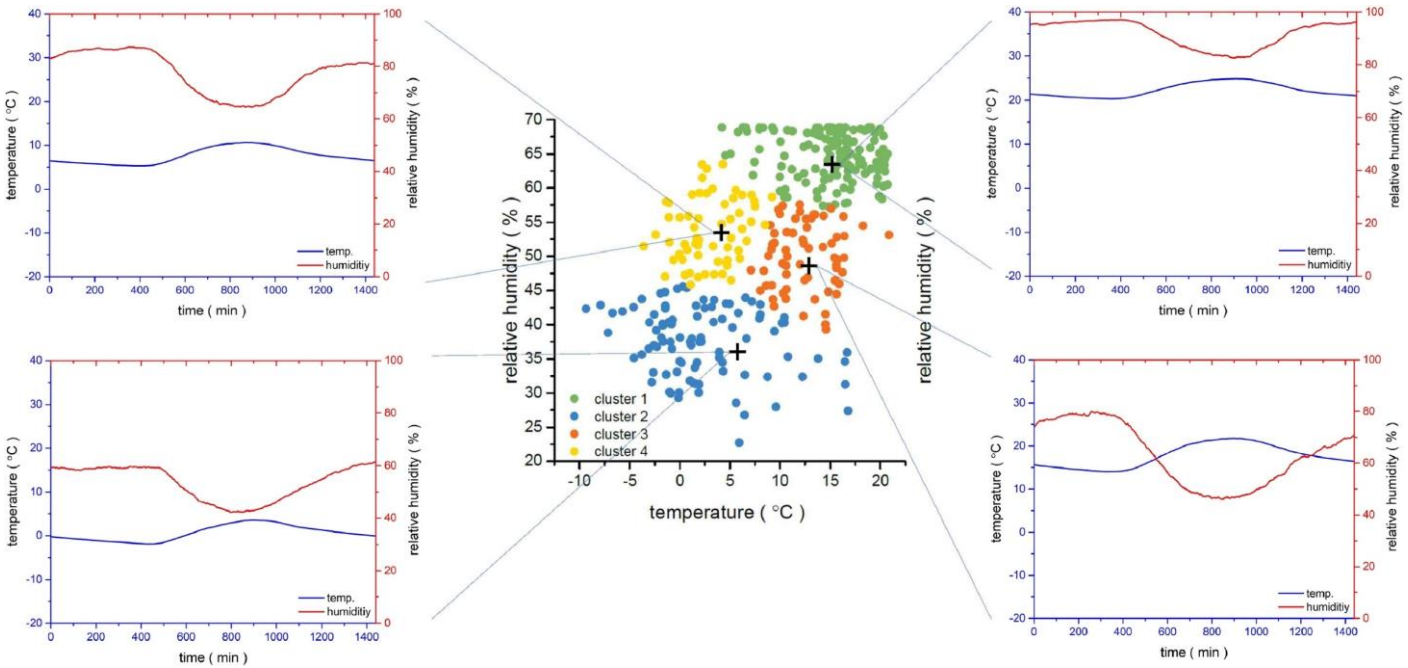

Figure 17. Feature vectors of centroids at each cluster.

3.3.4.3 Optimization results

The optimal design of the vaporizer is derived from the optimization problem mentioned above, which was solved with a DIRECT algorithm. Simulation is performed based on non-wavelet clusters, wavelet clusters, and multi-period. 12 case problems are solved to evaluate the effect of clustering method and size. For the non-wavelet clusters, k-means clustering is performed with raw weather data. For the multi-period optimization which is often used to obtain flexible design, the time- series dataset are divided according to season and month. Therefore, 4 and 12 representative weathers are obtained from the average of weather for each month. The 4 and 12 representative weathers have the same weight, respectively, and the objective function is a weighted sum of the AAV operation time under the representative days. Table 5 shows the results of the optimization. The design variables are converged in the range of bounds. The fin thickness and tube radius tend to converge to upper bounds in almost every case. In addition, the results of fan capacity from the number of wavelet-based clusters are somewhat larger than from the other type of cluster. The fin height converges near 0.1 m except for one case. The performance, which is defined below the table, is larger in the wavelet-based clusters than in other methods. This trend is also shown in Fig. 18. The performances of non-wavelet clusters and multi-period are volatile and sometimes fluctuates wildly depending on the number of clusters. However, the results from the wavelet show an almost equal performance at various clusters, which means optimal design from the feature extraction gives stable results with time-series data regardless of the number of clusters. In addition, the average performance increment of the wavelet-based clusters is 2.44%, 2.35%, and 22.75% larger

than the increments of the non-wavelet based clusters, multi-period, and original case, respectively. Wavelet-based clustering can extract dynamic characteristic of time-series dataset and the extracted dataset which is scalar at level 11 of Haar function can be vector using inverse Haar transform. However, non-wavelet clusters and multi-period only extract representative scalar weather condition which cannot reflect the dynamic characteristic of time-series dataset. Accordingly, the variability of the performance by month is lower at wavelet-based clusters which means the robustness of optimal design with wavelet-based clusters is better than an optimal design with non-wavelet based clusters and multi-period. For example, the ranges of performance increment are ±2.21% with non-wavelet based clusters and ±0.18% with wavelet-based clusters. The clusters based on a high-level of Haar function compress daily data into small pieces of data, which ignore a small proportion of the variability. The k-means clustering using the compressed data of a year better reflects the entire span of time. For this reason, the optimal design using the compressed data shows a small variability in performance during a year and better performance. On the other hand, in non-wavelet based clusters, a cluster can include two independent data, such as summer night data and winter noon data. Hence, the optimal design using the cluster is vulnerable to small fluctuations. The results of multi-period also show variability and lower performance because the representative days cannot reflect the trend of time-series dataset. The comparison of the results shows the robustness and effectiveness of an optimal design based on feature extraction with time-series weather conditions. In addition to the above two cases, *k*-means clustering in vectors can be also considered. However, it is already known that when the

complexity of the time-series data is projected onto the low- dimensional feature space, an explicit representative value can be obtained [73]. In addition, wavelet-based clustering is expected to have better efficiency for time-series data when the data is dependent on the intermediate level of Haar function rather than the lowest level of Haar function.

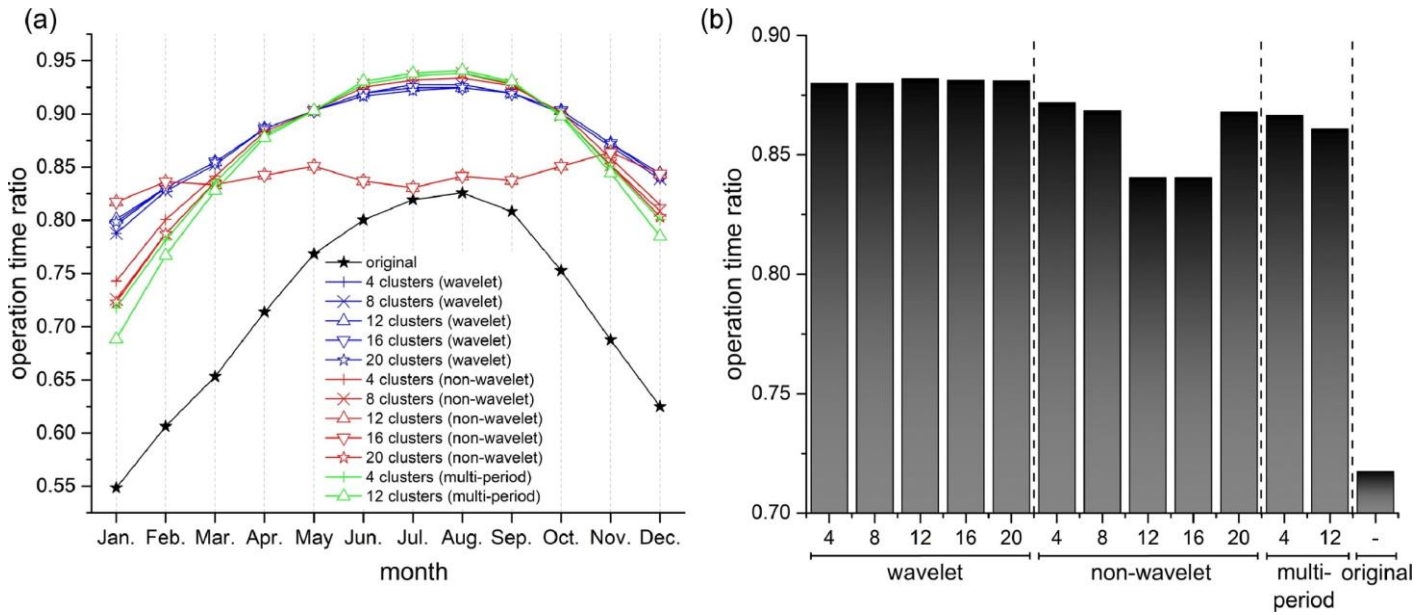

a) operation time ratio for each month b) average operation time ratio for different clusters. Operation time ratio is the ratio of operation time except defrosting time during a year when one year is 1.0.

Figure 18. Optimization results.

The correlations between design variables and performance were evaluated from the optimization results using Pearson's correlation coefficient [84]. The formula for the coefficient is

$$\rho_{A,B} = \frac{1}{N-1}\sum_{i=1}^{N}\left(\overline{\frac{A_i - \mu_A}{\sigma_A}}\right)\left(\frac{B_i - \mu_B}{\sigma_B}\right) \quad (3\text{-}32)$$

where μ_A, μ_B, σ_A, σ_B and N are the mean of A and B, the standard deviation of A and B and the number of dataset, respectively. The coefficient between fan capacity and performance is 0.2762 in wavelet-based clusters which is the larger than the coefficient of other variables and is −0.9996 in non-wavelet based clusters which are the lower than the coefficient of other variables. Therefore, the coefficients mean fan capacity is strongly linked to performance than other variables. The most of fan capacities at the wavelet-based cases are larger than those of the other cases in Table 5. The flow rate and the sensible heat transfer of the air stream are increased at high fan capacity which accelerates the growth of frost in the summer season (Jun.–Aug.) when the relative humidity is high. Hence, the performance of the wavelet-based clusters is kept low in summer. However, the trend is changed in the winter season (Dec.–Feb.). The relative humidity is lower, and a high flow rate only improves the sensible heat transfer and the case of wavelet-based clusters shows higher performance.

The variability of performance by month is related to the robustness of design and it is an important factor at the design of LNG vaporizer because the performance of LNG vaporizer should be not sensitive to weather fluctuations

for a constant supply of LNG. The variability of performance can be controlled by objective function modification.

$$\max_{\vec{y}} \sum_{i=1}^{k} w_i f(\vec{y}, C_i)$$
$$\rightarrow \max_{\vec{y}} \sum_{i=1}^{k} w_i f(\vec{y}, C_i) - \alpha \cdot Var\left(f(\vec{y}, C_i)\right) \quad (3\text{-}33)$$

which form is similar to stochastic optimization for maximizing the AAV performance through all clusters with weighted summation and simultaneously, minimize the variance of the AAV performance through all clusters boundary conditions. If clusters represent the macroscopic movement of the weather condition such as seasonal temperature change and humidity change, then the variability of the AAV performance via one-year simulation can be controlled by α.

As a result of the analysis, when α is less than 0.004, the larger α, the lower the performance during the summer season (Jun.–Aug.) and the greater the performance during the winter (Dec.–Feb.), the lower the overall variability. When α is greater than 0.004, in wavelet-based clusters, variability is lowered at all months, taking a loss in performance, as the weight of variance in the modified objective function increases. But, in non-wavelet based cluster, the larger the α, the performance decreases drastically, and variance increases. Non-wavelet based clusters show dominant performance over the particular alpha range, but show lower quality than wavelet cases in variance. Unlike non-wavelet, wavelet-based clusters are more intuitive to control the variability of design performance because the tendency of variance is monotonic as αincreases. Moreover, the variance of the AAV performance with wavelet

clustering is lower than that of non-wavelet clustering. Since wavelet clustering shows good results compared to non-wavelet clustering even when alpha is set to 0 in order to maximize the performance and wavelet clustering has a monotonic tendency and lower value of variance via changing α, the need to use wavelet clustering seems to be sufficient for robust design problem (Fig. 19).

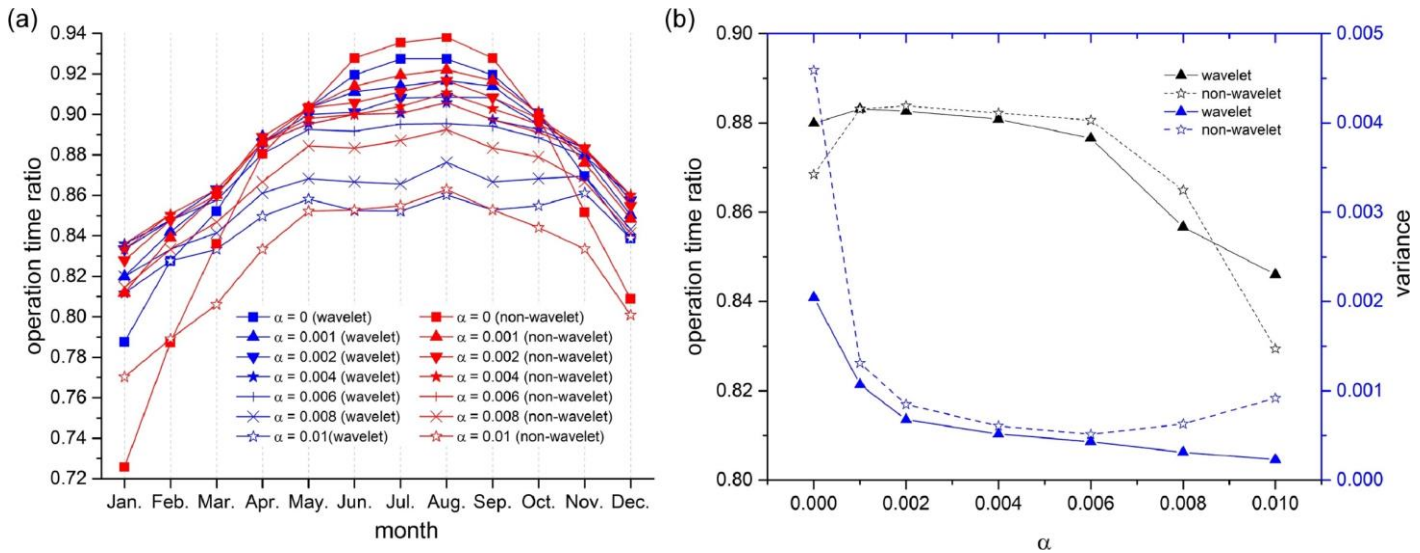

a) operation time ratio for wavelet-based and non-wavelet based clusters (8 clusters) through different **α** b) average and variance of the operation time ratio according to **α**.

Figure 19. Optimization results with the modified objective function.

3.3.4.4 Convergence of the problem

Fig. 20 shows the convergence of the problems. In the graph, the sign of the objective value is replaced with a minus. There are two types of clusters. The first one is a cluster of extracted features, so it includes a new time-series weather condition. The other is a cluster from the full data in minutes. It has a fixed weather condition point and does not reflect the time-series trend. In Fig. 20, the objective value of clusters with full data is lower than the value of clusters with features. It does not mean that the feature extraction causes poor performance because the weather condition C_i is different in each approach. Thus, the comparison should be derived from the one-year simulation to see if the performance is actually better. Furthermore, the extracted feature reflects the dynamic property of time-series data, which provides a harsh condition.

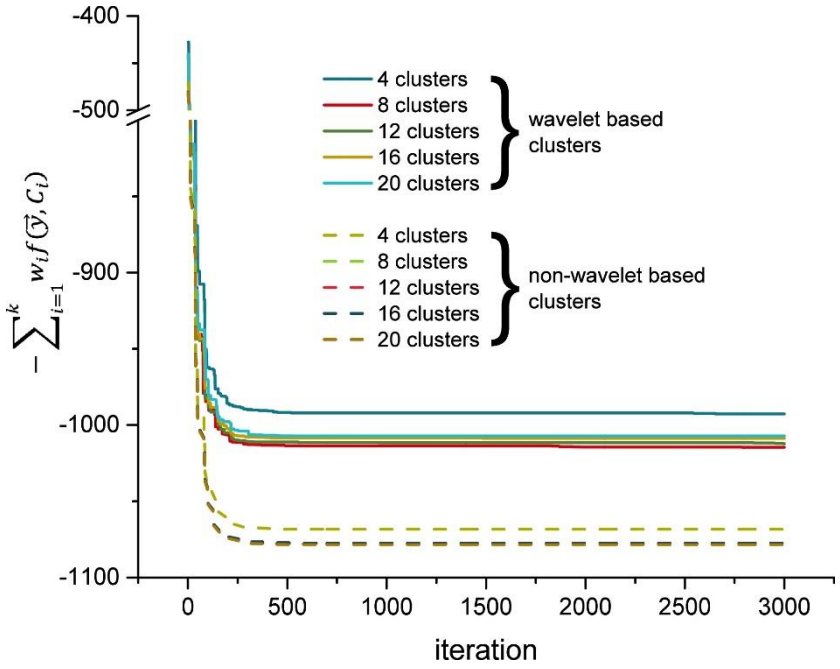

The graph shows the optimization problem is converged. Because the dataset which was used in the problem is different for two groups of clustering, lower minus objective value doesn't mean better performance.

Figure 20. Minus objective values at each iteration for the different cluster.

3.4 Conclusion

3.4.1 Modeling and analysis of AAV system

In a vaporizer, the growth of frost, vaporization of LNG, and convection of the air stream are closely related. This study proposed a numerical model to predict the dynamic performance of the vaporizer by analyzing these phenomena. The model determines the characteristics of the heat transfer phenomenon between air and LNG and the mass transfer phenomenon occurring on the frost surface according to the time and position. The temperature of the LNG and the frost thickness and density were calculated using the experimental conditions including the relative humidity and temperature of the ambient air and the flow rate and temperature of the LNG during operation. The model is validated using the experimental data of a pilot-scale AAV, Table 3 summarizes the ranges of the variated parameters used in the proposed dynamic numerical method.

The simulation results, which used the experimental conditions as the input, indicate that sensible heat contributes 7−12 times more to the total heat flux than latent heat. However, the difference in contribution between the two heat types reduces over time owing to frost accumulation. The computed frost thickness and density and temperature of the LNG account for the effect of the condensed frost around the tube on the performance of the vaporizer. As -150 °C, LNG enters the inlet of the vaporizer and frost begins to form on the tube at the front parts of the vaporizer. The frost accumulated in the vicinity of the inlet interferes with the heat exchange between the LNG and ambient air, causing cryogenic LNG to flow away without absorbing heat. Hence, the

position where the LNG is vaporized shifts to the back of the vaporizer with the lapse of time. As a result, the heat transfer performance at the front parts of the vaporizer is the maximum at the beginning of the operation owing to the temperature difference between the LNG and ambient air; however, the heat transfer performance at all the positions tends to converge to value over time. The performance of a vaporizer using upward draft air as a heat source is substantially affected by ambient air conditions such as the temperature, relative humidity, and velocity of air. The lower the relative humidity of the air, the weaker the influence of frost; consequently, the vaporizer can continuously maintain the heat exchange performance. A higher temperature of the ambient air also increases the amount of saturated water vapor, which accelerates the growth rate of frost; however, the simulation results demonstrate that the increase of the total heat flux owing to the difference in temperature is more influential than the heat transfer resistance of the frost layer. Dissimilar to the relative humidity and temperature of ambient air determined by the condition of the region where the vaporizer is located, the velocity of the air stream is attributed to the capacity of the fan. The effect of the air velocity on the frost deposition is negligible; however, it increases the sensible heat flux from the air to the LNG, enabling the continuous operation of the vaporizer.

In the study, the numerical model is validated by the pilot-scale vaporizer data; however, there are certain limitations. (1) In pilot-scale units, there are uncontrollable variables such as geothermal and solar heat. (2) The air stream causes physical movement of frost. (3) It is challenging to consider the influence of frost scattering and fog during operation. These limitations indicate that an AAV is highly vulnerable to external factors that are more or less

unpredictable. This is because, unlike the conventional heat exchanger that uses fixed heat transfer fluids, an AAV uses an atmosphere that varies with the weather, as the heat source.

The conclusions obtained from the research provide theoretical guidelines for enhancing the thermal performance of a vaporizer. Preliminary studies of the climate and regional conditions should be conducted for the design of an AAV, and it is critical to select the appropriate fan capacity. Moreover, by analyzing the frost growth and LNG-temperature profile, it is feasible to predict the appropriate operation time and defrosting time.

3.4.2 Robust design of AAV system

This study shows that by using wavelet-based optimization for designing a robust, wavelet-based clustering, which effectively reflects the trend at various time intervals, is suitable for reflecting the trends of a year at various scales. The features of temperature and relative humidity of a year are extracted using the Haar wavelet transform and *k*-means clustering. The Haar wavelet transform reflects the trend of a day, and it is evaluated by global sensitivity analysis. The level 11 of Haar function have a higher effect on global sensitivity analysis than level 1 of Haar function. Therefore, the level 11 of the Haar function was selected for *k*-means clustering. *k*-means clustering was used to group the level 11 of Haar functions, whose data size is 1/1440 that of the original time-series data. In addition, the computing time with the compressed data was approximately an order of magnitude less than that of the original time-series data. The weighted sum of the performance of the vaporizer based upon samples in clusters is the objective function of the optimization problem,

and the problem was solved with the DIRECT method. The evaluation of robustness in performance is based on simulation data of AAV model under the weather condition of a year. Comparison between multi-feature-based optimization and non-wavelet based optimization confirms the improvement of robustness and performance. The performance error in the different sizes of clusters is 0.18% with wavelet-based optimization, which was 1/12 that of the errors with non-wavelet based optimization. In addition, compared with the original case, the increment of average performance is 22.92% larger with wavelet-based clustering (12 clusters) which is 5.81% and 2.92% larger than the non-wavelet based clustering (12 clusters) and multi-period (12 periods) case, respectively. In wavelet-based clusters, the performance of the vaporizer shows low variability for the entire span of time, and better performance because the features used for optimization have compressed information about the trends of temperature and relative humidity. Accordingly, from the results of modified optimization, wavelet-based clusters reduce variability while minimizing loss of performance. The methodology can be used to design equipment and processes that are affected by volatile external conditions or unstable systems such as stock prices, weather conditions, biomedical measurement, and sound signals.

Chapter 4

Tunable protein crystal size distribution via continuous crystallization

4.1 Introduction

Despite their utility as combined solid-liquid separation, purification, formulation processes to convert active pharmaceutical ingredients (APIs) into final drug products, crystallization unit operations have been slow to benefit from the push towards Quality –by Design (QbD) and process analytical technologies (PAT). Industrial crystallizations are also still predominately performed under batch conditions, minimizing their operational flexibility, increasing capital equipment expenditures, and stymieing the realization of manufacturing efficiencies relative to a comparably productive continuous process [85, 86]. What is even worse, while the pharmaceutical industry routinely utilizes at- and on-line measurement tools such as mid-infrared spectroscopy probes and pressure sensors during the process development and pilot-plant stages, many of these real-time sensors are not employed at the industrial scale, thereby minimizing the extent to which control systems can deploy [87-89]. The pharmaceutical industry's reluctance to substitute for batch-wise unit operations throughout its API process trains—despite the successful experiences of the petrochemical, paper, and steel industries-exacerbates this problem [90-92]. As such, there exist opportunities not only to develop and demonstrate monitoring and control schemes for crystallization but also to design and implement novel continuous crystallizers [93].

Considerable progress has been made in the area of tubular continuous crystallizers designed for flow-through operation [94]. The first evidence supporting the crystallization of small-molecules flowing through a tube employed a pressure-driven pump scheme to combine a pentaerythritol tetranitrate-acetone solution with an aqueous anti-solvent through a short Kenics type static mixer positioned directly above a filter screen [95]. Approximately three decades later, Myerson and coworkers published the first demonstration of a multi-segment plug flow crystallizer [96]. Constructed from four jacketed glass tubes packed with Kenics mixers, this apparatus supported the crystallization of three different marketed APIs using multi-point anti-solvent addition to mediate the process. In the intervening years, Lemaître and colleagues developed the segmented flow tubular reactor (SFTR) using a 10 m length of 4 mm ID PTFE tubing [97, 98]. Peristaltic pumps were utilized to combine two aqueous solutions with air through a static mixer, forming alternating slugs of liquid and gas that traveled in unison through the system. Given its minimalist hardware and simplicity of operation, the basic SFTR has undergone a rapid re-design in recent years, enhancing its flexibility as a potential platform technology. Eder and colleagues probed the application of continuous seeding methods to SFTRs focusing on acetylsalicylic acid (ASA) crystallization [99, 100]. These same studies also demonstrated the first temperature gradient SFTRs (TB-SFTR), using a single length of silicone tubing coiled into multiple thermal baths set at predetermined temperatures, and showed the nucleation could be induced in particle-free solutions of ASA using small-scale insonation baths. Significantly, recent industry-led experiments applied a similar mesoscale version of this system to the mitigation of clogging

during flow-through pH-swing crystallizations [101]. Recently, using the model solute monosodium glutamate (MSG) and L-asparagine monohydrate (LAM), Braatz group further advanced the utility of TB-SFTRs by coupling them with novel flow-through seed generation methods leveraging rapid temperature shifts and directed, spatially localized ultrasonic irradiation [102, 103]. In parallel, they identified flow conditions and tubing dimensions that supported spontaneous, stable slug formation in the absence of multiple upstream mixers comprising more than two inlets [104].

Building upon these advances, this thesis suggests a scalable, tubular crystallizer designed to operate under continuous slug-flow and capable of on-line control of the entire cooling crystallization process for a small biomolecule (LAM) and demonstrate the system in a mathematical model coupling thermodynamic and kinetics of crystallization. First of all, a spontaneously induced slug-flow crystallization system was developed around modular counter-current heat exchangers (CCHEXs) comprising fully-disposable FDA compliant flow-paths of variable length and leveraging independent IMC-tuned PI controllers. Unlike the prior art in the tubular crystallization space, this system is not only useful as a process development tool but also amenable to both scale-up and scale-out strategies for increasing output. With the aid of a model-predicted controller (MPC), nucleation is induced, under stringently controlled temperature conditions, in fully-dissolved, particle-free solutions of LAM in a localized manner using an insonation probe. Nucleated material is then induced to spontaneously form liquid slugs, which traverse the heat exchangers. The images of product crystals from a large full-factorial design of experiments (DoE) are analyzed using our in-house analysis algorithm for

object segmentation, counting, and sizing. Finally, a first-principle mathematics model of the system coupling thermodynamic and kinetic model based on population balance model (PBM) is proposed and verified by the crystal size distribution (CSD) obtained earlier.

Furthermore, the fully automated system designed to operate under segment slug-flow and to capable of on-line control of the cooling process is applied to the continuous crystallization of the model protein HEWL. In addition to temperature, pH and buffered precipitant solution are used to control the supersaturation of HEWL at various defined points along the length of the crystallizer. These parameters are carefully combined to permit tuning particle size distribution (PSD) generated by the counter current heat exchanger (CCHEX) platform under controlled and seeded inlet conditions. The system is further demonstrated that this control is possible over a residence time as short as 25 – 30 minutes (2 – 4x shorter than similar recent reports). Powder X-Ray Diffraction (PXRD) and cross-polarized transmitted light microscopy are used to qualitatively score the relative ratio of amorphous-to-crystalline HEWL generated under each set of conditions tested. The images acquired using cross-polarized light is analyzed by the custom crystal image analysis algorithm designed for adjusting contrast and segmenting overlaid crystal image. Finally, the mathematical model including thermodynamic model and population balance model of the continuous protein crystallization is established and verified with the measured PSD.

4.2 Mathematical modeling and experimental verification of fully automated continuous slug-flow crystallizer

4.2.1 Experimental methods and equipment setup

4.2.1.1 Experimental apparatus

L-asparagine monohydrate (A8381; Sigma-Aldrich, St. Louis, MO), the commercially available material in powder form was used as the model small-molecule solute with deionized water ($\rho \geq 18$ MΩ-cm) for all crystallization experiments.

At the inlet, a 'pulse' of thermally equilibrated LAM solution is supplied to the crystallizer from a well-mixed, three-necked, round-bottom flask. The LAM solution is maintained at temperatures in excess of 70 ^{o}C for many hours, while preventing evaporation of the solvent, thereby ensuring that all experiments are performed with constant-concentration, particle-free feedstocks. After entering the crystallizer, the particle-free aqueous phase traverses a short segment of insulated tubing before transiting through the first CCHEX (the 'pre-HEX'; 2 m) and passing beneath a Sonics 13 mm insonation probe. The purpose of the pre-HEX which employed a model predictive control (MPC) is to rapidly cool the LAM feedstock from its grossly undersaturated condition at the system inlet to a temperature amenable to the formation of nuclei. To our knowledge, the implementation of such a continuous temperature control system upstream of an insonation-based nucleation stage represents a substantial design improvement over similar approaches published in recent years [99, 100, 103-106]. Following insonation, LAM solution is mixed with filter air to form stable liquid slugs and immediately enters the second heat exchange module ('HEX

1’). Slugs travel with gravity along the length (11 m) of the coil comprising HEX 1 and traverse the third (‘HEX 2’) and fourth (‘HEX 3’) shell and tube modules (both 14.8 m long) in a manner identical to their passage through HEX 1. Stable slug-flow was induced on the tube-side of the crystallizer using a method similar to that described by Jiang and colleagues [103, 104]. Combinations of air and liquid flow rates that yielded stable slugs were identified empirically, and all experiments were conducted under air and liquid flow rates of 6 mL/min.

Fig. 21 provides schematic representations of the system. The crystallizer comprises four modular shell and tube CCHEXs arranged in series. Crystallization occurs only in the tube portion of each module and coolant (DI water) is confined to the shell of each CCHEX. Coolant is driven through the shell-sides using pairs of peristaltic pumps. One pump in each pair withdraws cold DI water from a common recirculating batch and a second common recirculating batch provides hot DI water. This scheme allows the flow rate and temperature of the coolant within a given CCHEX shell to be maintained independently of all other modules.

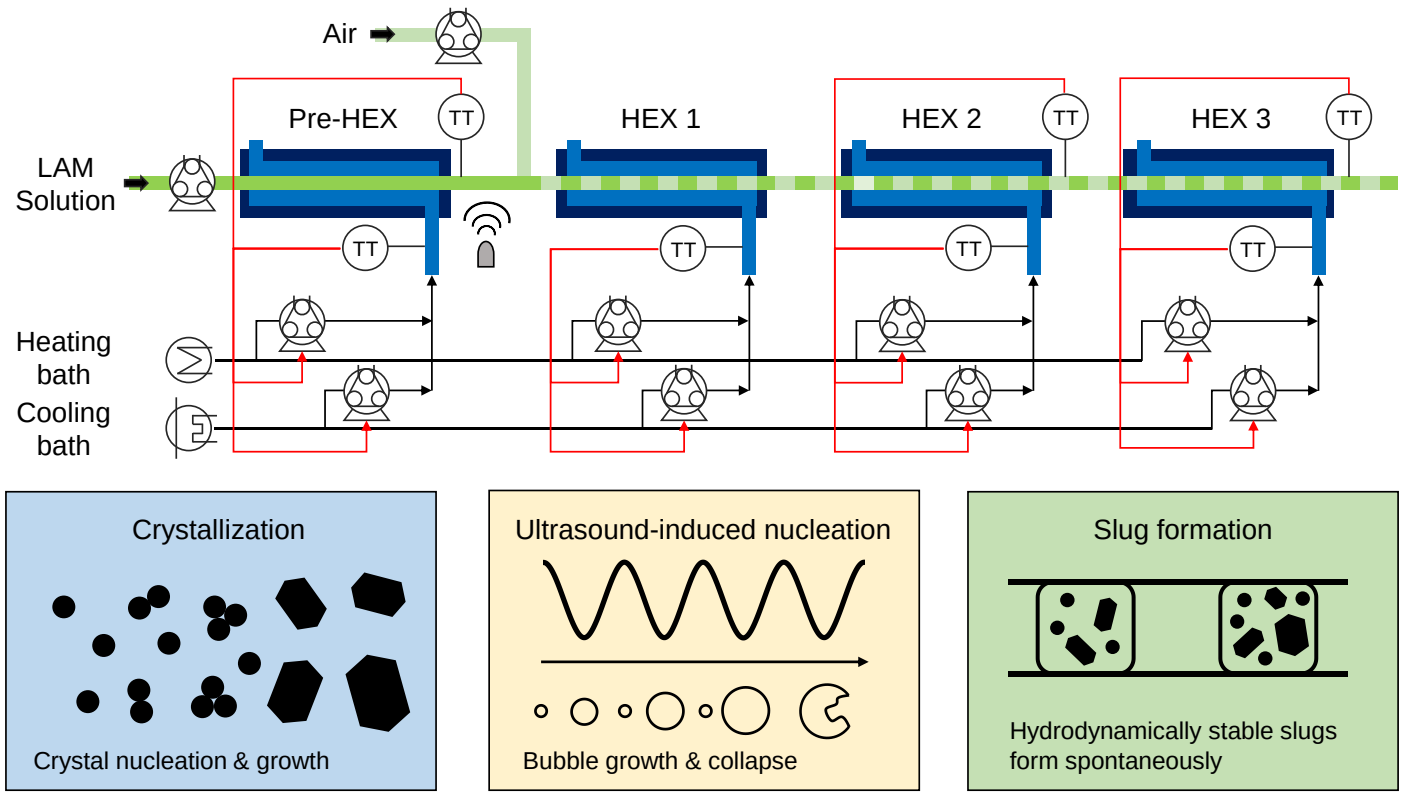

Figure 21. Schematic of the tubular continuous crystallizer.

Seven ungrounded transition-joint thermocouples provide real-time measurements of temperature at critical positions along the length of the crystallizer. Shell-side temperature readings are acquired by placing a thermocouple in direct contact with the flowing coolant. By contrast, to prevent errant nucleation, the temperature of LAM slugs is measured indirectly by fastening thermocouples to the outer wall of the tubing comprising tube-side of the system. An empirically-derived linear correlation implemented as part of the custom software required for overall system operation is used to calculate internal LAM slug temperatures from temperatures measured at the wall at the time of acquisition. Temperature setpoint tracking is achieved via the implementation of classical proportional-integral (PI) controllers that ratiometrically vary the relative flow rates of each pump in a given set. Every system hardware was operated via custom software written and implemented using MATLAB 2016b (v9.1.0.441655; The MathWorks, Inc.). The software includes standard signal processing subroutines. Leveraging the built-in timer class provided by MATLAB, the same series of methods runs at 1s intervals for the duration of an experiment: 1) all thermocouples are probed in a single call to a data acquisition module; 2) temperature signals are filtered; 3) vectorized PI controllers select new shell-side flow rates; 4) shell-side pumps are actuated sequentially; 5) new thermocouple and pump data is appended to the historian. All pumps are operated in an open-loop fashion. The use of MATLAB timers affords transparent low-level task scheduling functionality.

4.2.1.2 Full-factorial design of experiment (DoE)

The design of experiments was constructed with the aim of probing the effect of both insonation power output (probe vibrational amplitude, %) and

temperature on nucleation rate. The amplitude of ultrasonication equipment for nucleation located between pre-HEX and HEX 1, and the temperature set points of pre-HEX and HEX 1 were listed in Table 6. Shell-side temperature and flow rate setpoints were selected with the aid of the custom thermodynamic model to ensure that the slug-side temperatures equaled those in Table 6, and to mitigate temperature crossovers near the center of each heat exchanger as a result of energy losses to the surroundings.

Table 6. Full-factorial DoE designed to probe the dynamics and kinetics of LAM crystallization.

experiment number	1	2	3	4	5	6	7	8	9
ultrasonication amplitude set point (%)	0	30	90	0	30	90	0	30	90
pre-HEX temp. (°C)	32	32	32	32	32	32	32	32	32
HEX 1 temp. (°C)	32	32	32	42.6	42.6	42.6	51.2	51.2	51.2
experiment number	10	11	12	13	14	15	16	17	18
ultrasonication amplitude set point (%)	0	30	90	0	30	90	0	30	90
pre-HEX temp. (°C)	42.6	42.6	42.6	42.6	42.6	42.6	42.6	42.6	42.6
HEX 1 temp. (°C)	32	32	32	42.6	42.6	42.6	51.2	51.2	51.2
experiment number	19	20	21	22	23	24	25	26	27
ultrasonication amplitude set point (%)	0	30	90	0	30	90	0	30	90
pre-HEX temp. (°C)	51.2	51.2	51.2	51.2	51.2	51.2	51.2	51.2	51.2
HEX 1 temp. (°C)	32	32	32	42.6	42.6	42.6	51.2	51.2	51.2

For all 27 experiments the HEX 2 and HEX 3 shell-side inlet temperature set points were 21.75 and 13.5 °C, respectively. (The pre-HEX and HEX 1 temperature correspond to the slug-side temperature at the outlet.)

All LAM slugs entered the crystallizer at a concentration of 0.1058g LAM/g dH2O (Tsat = ~53 ºC), and the temperature of the solution is 93 – 95 ºC. The pre-HEX temperature set points were selected to correspond to the saturated, meta-stable, and supersaturated regions of the LAM solubility diagram [107].

4.2.1.3 Crystal size distribution (CSD) acquisition

The LAM slug collected was subsequently vortexed to induce settling in the suspension of LAM crystals. Thirty-two transmitted light photographs were taken using a stereomicroscope and color USB camera at maximum intensity and a magnification of 12.22 μm/px for each experiment.

The custom image analysis algorithm capable of detecting the size of all crystals is schematized in Fig. 22. The grayscale image was obtained by converting color photographs, and an alternating sequential filtering operation was employed to estimate and remove variations in background intensity. The image of objects in the foreground is obtained by subtracting the intensity of the background and scaling the divided image. The label matrix which assigns 0 to the background and different positive integers to each object was then converted into an RGB color image to visualize successfully segmented crystals. Each labeled region was identified as different objects and size of all crystals were accurately estimated in pixel level. By applying the same procedure to all experiments, the lumped crystal size distribution was obtained.

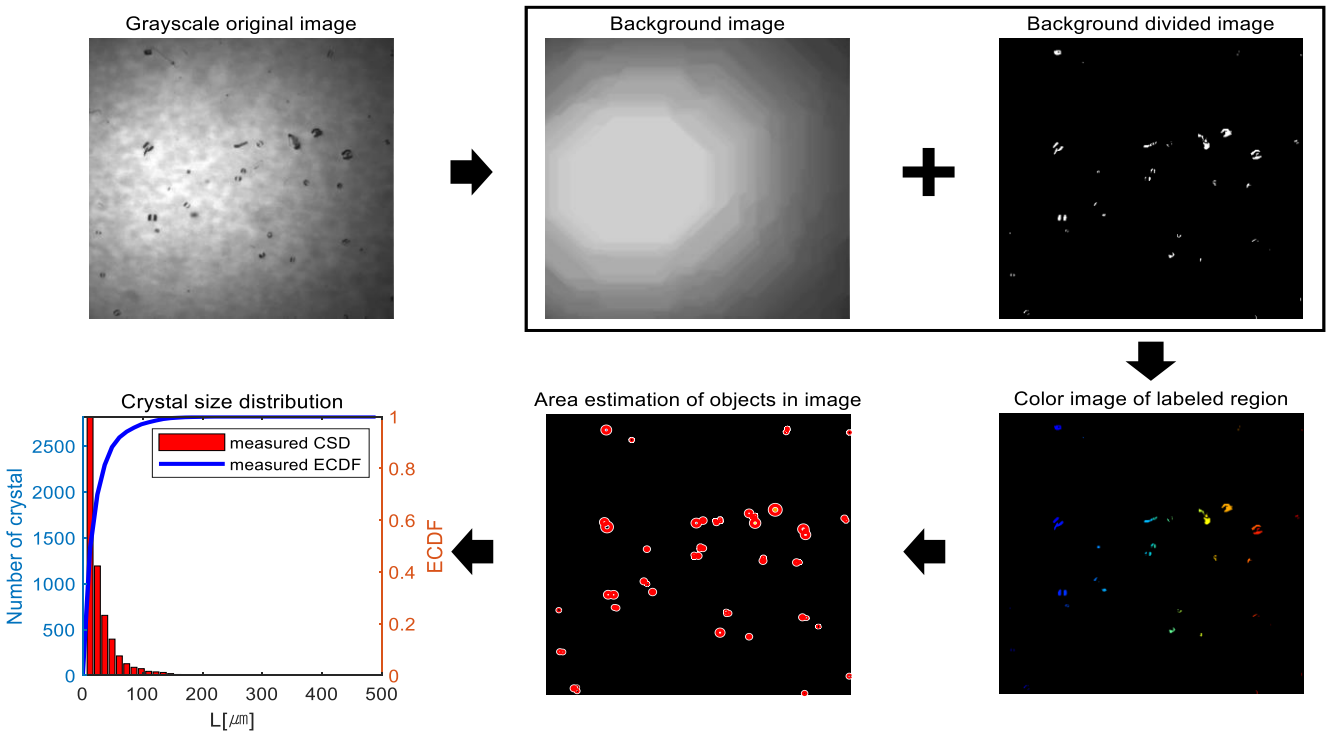

Figure 22. Graphical summary of the crystal image analysis algorithm.

Given that all experiments generating LAM CSDs described were conducted at steady state and operated under saturated outlet concentrations and the mass balance

$$\mathrm{C_{in}} = \rho_c k_v \int_0^\infty L^3 \alpha \hat{f}(z_N, L) dL + \mathrm{C_{sat}}(\mathrm{T_{out}}) \quad (4\text{-}1)$$

was used to calibrate CSD in a reasonable range, where the value of crystal density (ρ_c) is 5.6966×10^3 kg/m^3, the dimensionless shape factor (k_v) is 0.39551, and the difference in solution concentration between inlet and outlet, $\mathrm{C_{in}} - \mathrm{C_{out}}(\mathrm{T_{out}})$ is 84 kg/m^3, which is the experimental conditions. α is a dimensionless scaling factor that corrects for the sampling bias associated with acquiring crystal images in only one focal plane and $\hat{f}(z_N, L)$ is the observed CSD at slug segment from the outlet. The true CSD $f(z_N, L)$ is obtained by multiplying a scaling factor and the observed CSD. For discretely observed data, the mass balance equation (Eq. 4-1) is modified to

$$\mathrm{C_{in}} = \rho_c k_v \sum_{i=1}^{M} L_i^3 \alpha \hat{f}(z_N, L_i) \Delta L + \mathrm{C_{sat}}(\mathrm{T_{out}}). \quad (4\text{-}2)$$

When fitting α, wrongly detected data such as crystals whose size is more huge than others incomparably were removed.

4.2.2 Mathematical model of crystallizer

4.2.2.1 Thermodynamic model

In contrast with a co-current heat exchanger, the counter-current heat exchanger should be iteratively solved by predicting and evaluating the temperature of one side fluid because fluids flow in the opposite direction [108-110]. Based on heat transfer phenomena, a first-principles thermodynamic

model of a shell-and-tube crystallizer that explicitly accounts for all significant heat fluxes within the system is represented in this chapter.

As a characteristic of the continuous crystallizer, the time derivative terms are dropped, and separate energy balances around control volume within the shell- and tube-sides (also respectively 'cold' and 'hot') of the CCHEX were derived. Assuming 1) constant fluid heat capacity C_p and density ρ_c for both the shell- and tube-sides of the crystallizer, 2) the heat transfer between solution and air within slug-flow can be ignored because the indirect heat transfer coefficient between slugs and coolant is far bigger than former one, indicating that water plays a dominant role in the thermodynamics of the system, 3) the heat flux from slug to ambient air is negligible, and 4) the temperature distribution in radial direction in the slug tube is neglected. Generally, the concentration and temperature are uniformly distributed in a single slug. The outlet temperature of shell-side fluid should be predicted and updated for each iteration. When the predicted value at the shell-side inlet is matched with the observed data, the calculation is stopped. The discretized tube- and shell-side energy balance can be written by analogy to Eq. 4-3 and 4-4 employing a forward and backward differencing formulation to capture the counter-current operation of the CCHEX. In equations

$$T_{h,i+1} = T_{h,i} + \frac{\dot{Q}_{crystal,i} - \dot{Q}_{h,i}}{\rho_h V_h (1-\xi) C_{p,h}} \tag{4-3}$$

$$T_{c,i} = T_{c,i+1} + \frac{\dot{Q}_{h,i} + \dot{Q}_{c,i}}{\rho_c V_c C_{p,c}} \tag{4-4}$$

$$\xi = \frac{\dot{V}_{air}}{\dot{V}_{air} + \dot{V}_{water}}, \tag{4-5}$$

the discretized tube-side slug-flow is represented as h, and shell-side flow is expressed as c, where the volume correction factor, ξ is incorporated to adjust the heat capacity of slug-flow, and $\dot{Q}$ is the heat of crystallization or conductive heat fluxes at steady-state. All material properties are treated as constants, and a cylindrical coordinate system with the +z axis oriented along the direction of tube-side flow is assumed. In the equation of heat fluxes

$$\dot{Q}_{h,i} = \mathrm{UA}_{h/c,i}(T_{h,i} - T_{c,i}) \tag{4-6}$$

$$\dot{Q}_{c,i} = \mathrm{UA}_{c/air,i}(T_{c,i} - T_{air,i}) \tag{4-7}$$

$$\dot{Q}_{crystal,i} = \frac{\mathrm{m}\Delta\mathrm{H_c}}{\mathrm{M_c}}\frac{dC}{dz} \tag{4-8}$$

used in the thermodynamic model, UA is the product of the overall heat transfer coefficient and the surface area for heat transfer, m is the mass of a slug within tube-side, and $\Delta\mathrm{H_c}$ and $\mathrm{M_c}$ are the heat of crystallization and molecular weight of LAM which is -35700 J/mol and 0.150 kg/mol, respectively [111]. The convective heat transfer coefficient used to derive UA is determined by the convection correlations for flow in a circular tube [112]. The thermodynamics of the uninsulated connecting regions between heat exchangers and interaction between a heat exchanger and the ambient environment are also correctly considered. The heat of crystallization is ignored at first iteration due to the absence of solution concentration profile with the +z

axis, but once the gradient of the concentration is obtained at the kinetic model, it is automatically predicted and updated for next iteration.

4.2.2.2 Kinetic model

The mathematical treatment of liquid slugs as well-mixed batch crystallizers is a traditional technique supported by experimental evidence [104, 111]. As such, building upon the framework set forth, a population balance model (PBM) can be applied to yield a generalized description of the evolution of the crystal size distribution, $f(z,L)$ associated with a given liquid slug in time and space like

$$\frac{\partial f(L,\tau)}{\partial \tau}+\frac{\partial\{G(S,T;\boldsymbol{\theta}_{\mathrm{g}})f(L,\tau)\}}{\partial L}=B(S,T;\boldsymbol{\theta}_{\mathrm{b}})\delta(L). \qquad (4\text{-}9)$$

In the above equation, L is the characteristic length spanned by $f(L,\tau)$ with units of μm and $\delta(L)$ is the Dirac delta function [113]. $G(S,T;\boldsymbol{\theta}_g)$ and $B(S,T;\boldsymbol{\theta}_b)$ are the rate of crystal growth and the nucleation rate, respectively, and the rates significantly depend on the supersaturation ratio $S=C/C_{sat}$ and temperature with vectors of growth and nucleation kinetic parameters. The growth and nucleation are considered as the only dominating phenomena in the continuous crystallizer and no breakage or agglomeration occurs.

The primary nucleation occurs from the solution without the presence of crystals at high supersaturation. Although two-step mechanism of nucleation is consistently proposed to complement the limitations and the major assumptions, the nucleation derived from classical nucleation theory (CNT) has been enough to fit bulk data from the industrial case [114-116]. In CNT, the interaction and surface tension at the interface and interaction within the inner core of the

nucleus consist Gibbs energy of homogeneous nucleation, and the competition of the two aspects determines the critical size of the nucleus and the energy change needed to stabilizing [116, 117]. Thus, the kinetics of primary nucleation is

$$B_{pri.}(S,T;\boldsymbol{\theta}_{\mathrm{pri}}) = \mathrm{A}\exp\left(-\frac{4\beta^3\pi\sigma^3\Omega^2}{27\alpha^2\mathrm{k}^3T^3(\ln S)^2}\right), \tag{4-10}$$

where the α and β are surface and volume shape factors, σ is the surface tension of the nucleus, and Ω represents the molecular volume of solute. The pre-exponential factor A is a theoretically complicated function of molecular level parameters, but it can be derived by the rates of condensation and dissociation (Eq. 4-10). Since the time scales of formation and dissociation of smaller crystals are much shorter than the characteristic times for formation and growth of the critical size crystal, the nucleation process would attain a quasi-steady-state after a short lapse of time [118]. Then the equation is clearly expressed like

$$\begin{aligned} &B_{pri.}(S,T;\boldsymbol{\theta}_{\mathrm{pri}}) \\ &= \frac{1}{2\pi}\beta_0\mathrm{n}_0\left(\frac{\mathrm{k}T}{2\sigma\eta^2}\right)^{\frac{1}{2}}\exp\left(-\frac{4\beta^3\pi\sigma^3\Omega^2}{27\alpha^2\mathrm{k}^3T^3(\ln S)^2}\right), \end{aligned} \tag{4-11}$$

where η is core repulsion range and n_0 denotes the number density of the condensing molecules in solution at an infinite distance from the crystal.

Numerous publications have presented the effect of insonation on the induction period and width of the meta-stable zone [119, 120]. In ultrasonic nucleation, the specific surface area of the bubbles, the adsorption properties of the forming cluster, and the chemical potential for nucleation induction are

different from the not-initiated case [37, 38]. By modifying the primary equation, the equation

$$B_{ins.}(S,T;\boldsymbol{\theta}_{\mathrm{ins.}}) = \mathrm{A_{ins.}} T^{\frac{1}{2}} (\ln S + \mathrm{C_{ins.}}\Delta \mathrm{x}) \exp\left(-\frac{\mathrm{B_{ins.}}}{T^3 (\ln S + \mathrm{C_{ins.}}\Delta \mathrm{x})^2}\right) \quad (4\text{-}12)$$

can be given with three parameters $A_{ins.}$, $B_{ins.}$, and $C_{ins.}$ which could differ in particular insonation environment and $\Delta \mathrm{x}$ is the amplitude setpoint of ultrasonication.

The secondary nucleation is the dominant nucleation in industrial crystallization [121]. As the nucleation occurs under the presence of pre-existing crystals, the factors such as the supersaturation, the rate of cooling, the liquid velocity, and impurity concentration affect the generation of secondary nuclei [29, 40, 41]. Though several publications treat the secondary nucleation phenomena, the mechanisms and kinetics are not fully elucidated so the empirical power law model

$$B_{sec.}(S,T;\boldsymbol{\theta}_{\mathrm{sec.}}) = \mathrm{k_N} M_T^{\mathrm{j}} \left(C - C_{sat}(T)\right)^{\mathrm{n}} \quad (4\text{-}13)$$

with the suspension density

$$M_T = \rho_{\mathrm{c}} \mathrm{k_v} \int_0^{\infty} L^3 f(L) dL \quad (4\text{-}14)$$

have been usually used to fit experimental data.

Fundamentally, the crystal growth rate is expressed as the linear growth rate of a particular face. The rate of growth is mainly controlled by the cooling rate of the solution, the anti-solvent concentration, and pH but it is well known that the presence of impurities significantly affects the rate [122-124]. The key idea of

a popular analytical model for crystal growth is a screw dislocation with a surface developing growth of layer [125, 126]. The growth equation

$$G\left(S,T;\boldsymbol{\theta}_g\right) = K_1 T(S-1)ln(S)\, tanh\left[\frac{K_2}{Tln(S)}\right] \qquad (4\text{-}15)$$

known as the Burton-Cabrera-Frank (BCF) is most commonly used and established under the assumption that diffusion on the crystal surface is considered to be the rating rate step which is known as true in vapor growth [127].

In slug-flow, coaxial mixing in the slug promotes high spatial uniformity of temperature and solute diffusion so the diffusion on crystal surface can be considered as the rate determining step [104]. The dissolution step of crystals which occurs under negative supersaturation condition $C > C_{sat}(T)$ is simply calculated by reducing the total mass of crystals and shifting the distribution to the range of smaller size crystals.

Table 7. The simplified version of the first-principle model with two or three parameters.

Inputs to the PBM	Equations with parameters
Primary nucleation	$B_{pri.}(S,T;\boldsymbol{\theta}_{\text{pri}}) = \theta_{\text{pri.},1} T^{\frac{1}{2}} (\ln S) exp\left(-\frac{\theta_{\text{pri.},2}}{T^3 (\ln S)^2}\right)$
Primary nucleation due to insonation	$B_{ins.}(S,T;\boldsymbol{\theta}_{\text{ins.}}) = \theta_{\text{ins.},1} T^{\frac{1}{2}} \left(\ln S + \theta_{\text{ins.},3}\Delta\text{x}\right) exp\left(-\frac{\theta_{\text{ins.},2}}{T^3 \left(\ln S + \theta_{\text{ins.},3}\Delta\text{x}\right)^2}\right)$
Secondary nucleation	$B_{sec.}(S,T;\boldsymbol{\theta}_{\text{sec.}}) = \theta_{\text{sec.},1} M_T^{\theta_{\text{sec.},2}} \left(C - C_{sat}(T)\right)^{\theta_{\text{sec.},3}}$
Growth	$G\left(S,T;\boldsymbol{\theta}_{\text{g}}\right) = \theta_{\text{g},1} T (S-1) \ln(S) \tanh\left[\frac{\theta_{\text{g},2}}{T \ln(S)}\right]$

With the equations enumerated in Table 7 and discretization techniques, the partial differential PBM (Eq. 4-9) can be reduced to the ordinary differential equation (ODE)

$$\frac{\partial f(L_{n+1},z)}{\partial z}+\frac{G\left(S,T;\boldsymbol{\theta}_{\mathrm{g}}\right)}{v_z(L_n)}\left[\frac{f(L_{n+1},z)-f(L_n,z)}{\Delta L}\right] = \frac{B(S,T;\boldsymbol{\theta}_{\mathrm{b}})}{v_z(L_n)}\delta(L) \tag{4-16}$$

$$B = B_{pri.} + B_{ins.} + B_{sec.} \tag{4-17}$$

with the initial condition

$$f(\boldsymbol{L}, z=0) = \mathbf{0}. \tag{4-18}$$

The forward differencing scheme over characteristic crystal length (L) is used to convert the PBM and size independent growth with no growth dispersion is assumed. Since the mass reduction of total solute-induced by nucleation is negligible, the growth rate is solely involved in mass balance equations

$$\frac{dC}{dz} = 3\frac{G\left(S,T;\boldsymbol{\theta}_{\mathrm{g}}\right)\rho_{\mathrm{c}}k_{\mathrm{v}}\mu_2}{v_z} \tag{4-19}$$

$$\mu_2 = \int_0^{\infty} L^2 n(L) dL \tag{4-20}$$

$$C(z=0) = \mathrm{C_{in}} \tag{4-21}$$

of LAM solute, where μ_2 is the 2nd-order moment proportional to the total surface area of crystals. The Eq. 4-16 and Eq. 4-19 are solved simultaneously with boundary conditions given by Eq. 4-18 and Eq. 4-21 over the length of the

tubular crystallizer. Based on the spatial trajectory of temperature obtained from a thermodynamic model, the trend of LAM solubility

$$C_{sat} = 3.084 \times 10^{-2} - 1.373 \times 10^{-3}T + 5.214 \times 10^{-5}T^2, \quad (4\text{-}22)$$

supersaturation ratio, nucleation rate and growth rate for z-axis direction are derived and discretized in the same way as the population equation and the concentration equation.

4.2.3 Results and discussion

4.2.3.1 Experiments

The box-and-whisker plot shown in Fig. 23 summarizes the CSDs obtained from image analysis algorithm and calibration across all 27 experiments (section 4.2.1.3). From the plot, it is evident that the LAM CSDs produced under different CCHEX operating conditions exhibit substantial diversity in skewness and median crystal size (black point in a circle within each box). The resolution of tiny crystals is strictly limited by the optical train employed, producing a consistent cutoff in all CSD at ~12μm.

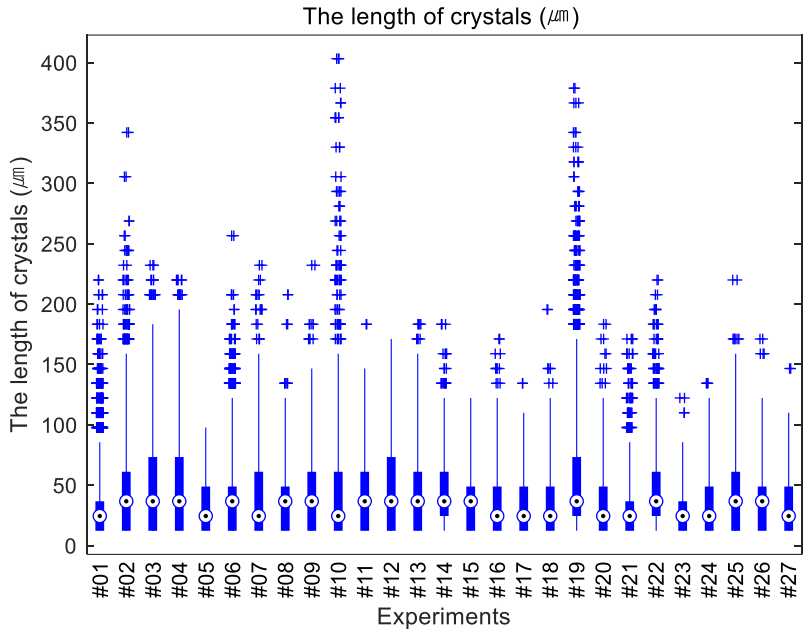

The black point in a circle within each box represents the median of the populations. The box edges represent the 25th and 75th percentiles. All data outside the 25th and 75th percentiles are shown explicitly as blue circles.

Figure 23. Box plot comparing the LAM CSDs obtained from all 27 studies in the full-factorial DoE.

In overall experiments, median lengths of sample distribution are almost same (24.44 μm or 36.66 μm), which is caused by the measurement limitation such as the low resolution of images (12.22 μm/pixel) and the error of image analysis algorithm where the sharp change of the contrast is recognized as crystals. About sonocrystallization, the past studies show the more nuclei were formed and the induction time of nucleation was shortened with ultrasonication [103, 128]. The effect of ultrasound consistent with the results on crystallization is also observed in Fig. 23. Under the indirect ultrasonication assisted monotonous cooling nucleation where the outlet temperatures of HEX 1 are equally set (Exp.1–3, Exp.10–12, and Exp.19–21), the temperature of pre-HEX determines the level of supersaturation where primary nucleation is induced (see Fig. 24). When the supersaturation is higher where the temperature of the solution is rapidly decreased (93–95 ^{o}C to 32 ^{o}C or 42.6 ^{o}C), the nucleation is hardly controlled with the use of ultrasonic irradiation (Exp.1–3, Exp.10–12). In contrast, when the nucleation is successfully induced at a lower level of supersaturation, the mean and standard deviation of the crystal size distribution is reduced as the amplitude of ultrasonication is higher (Exp.19–21). The mean and standard deviation length of the crystal of Exp.21 is 39 % and 42% smaller than Exp.19 and 16% and 9% smaller than Exp.20, respectively.

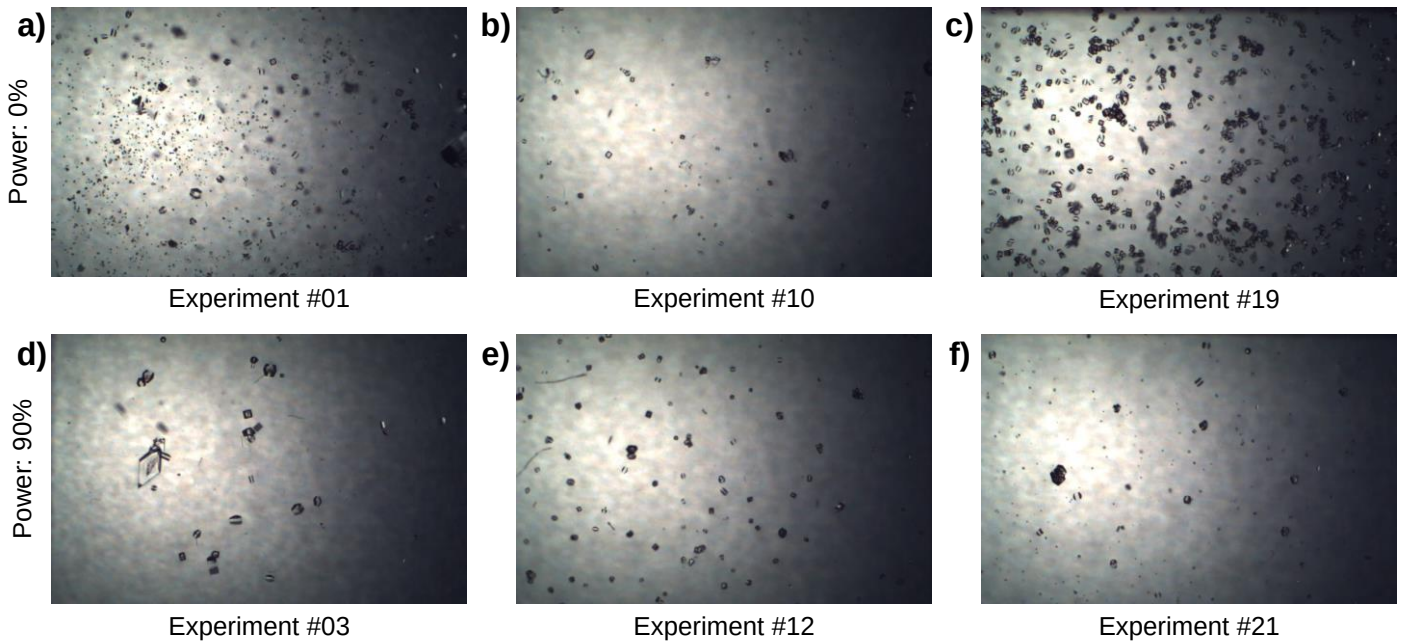

The ultrasonication amplitude, and outlet temperature of slug-flow at pre-HEX and HEX 1 are respectively (a) Exp.1: 0 %–32 ºC–32 ºC, (b) Exp.10: 0 %–42.6 ºC–32 ºC, (c) Exp.10: 0 %–51.2 ºC–32 ºC, (d) Exp.3: 90 %–32 ºC–32 ºC, (b) Exp.12: 90 %–42.6 ºC–32 ºC, (c) Exp.21: 90 %–51.2 ºC–32 ºC.

Figure 24. Representative micrographs 1 from LAM DoE experiments.

In the range of temperature of HEX 1 set points from 42.6 ºC to 51.2 ºC, there are some cases where the slug-flow is undersaturated due to the reversal in the operation condition (Fig. 25). When the local temperature is increased, the nuclei and crystals previously formed are expeditiously dissolved until the concentration of the solution is equivalent to the solubility. Once the crystals have been dissolved at intermediate crystallization, the large variability in the size of crystals (Exp.7–9) or the small size of crystals caused by not enough time for subsequent crystal growth is observed (Exp.16–18). For example, the sample distribution from Exp.27–29 has 5 %–24 % lower standard deviation than Exp.7–9 and 5 %–12 % larger mean size crystals than Exp.16–18.

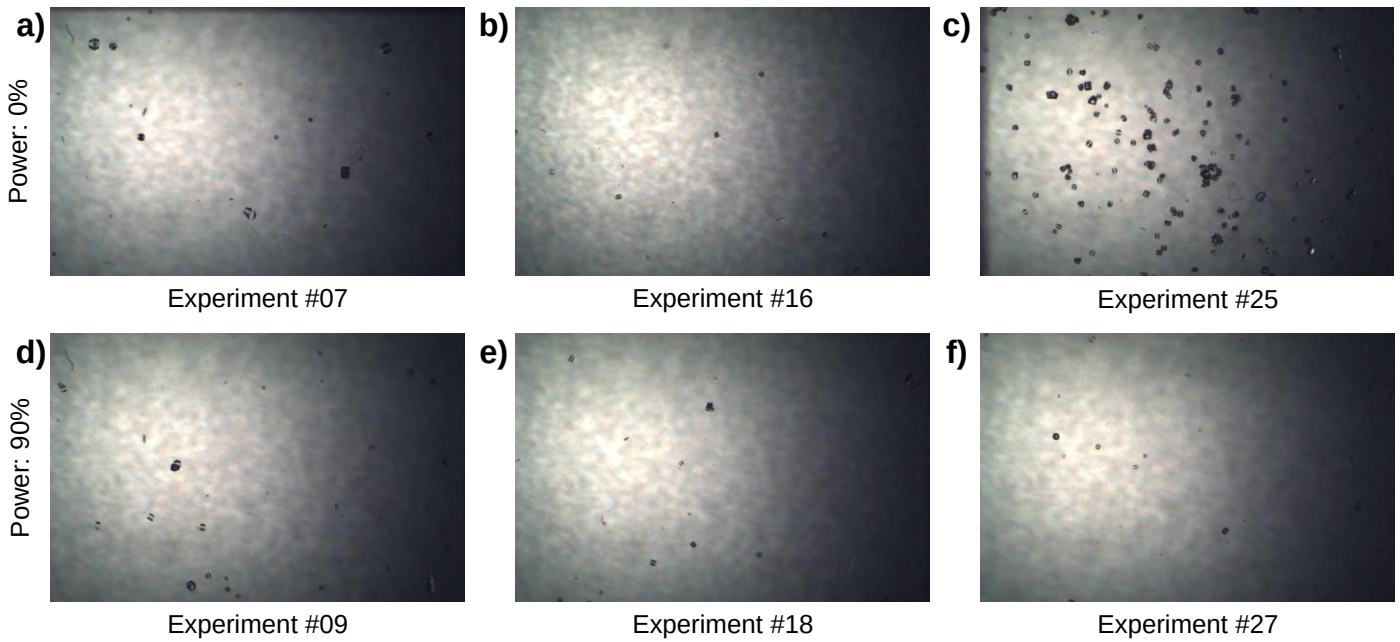

The ultrasonication amplitude, and outlet temperature of slug-flow at pre-HEX and HEX 1 are respectively (a) Exp.7: 0 %–32 ºC–51.2 ºC, (b) Exp.16: 0 %–42.6 ºC–51.2 ºC, (c) Exp.25: 0 %–51.2 ºC–51.2 ºC, (d) Exp.9: 90 %–32 ºC–51.2 ºC, (b) Exp.18: 90 %–42.6 ºC–51.2 ºC, (c) Exp.27: 90 %–51.2 ºC–51.2 ºC.

Figure 25. Representative micrographs 2 from LAM DoE experiments.

4.2.3.2 Verification of a mathematical model

Table 8. summarized the results of kinetic parameter estimation of the mathematical model of the continuous crystallizer. The CSDs from experiments operated in the insonation-free environment (Exp.1, 4, 7, 10, 13, 16, 19, 22, and 25) were fitted without a term of ultrasound-induced nucleation. For the overall experiments, the ECDF of observations was established by shape-preserving piecewise cubic interpolation with observed populations of crystals on a regular interval (12.22 μm) and precisely compared with model predicted ECDF point by point. The kinetic parameters that result in a minimum of the errors between the ECDFs were numerically estimated by genetic algorithm (GA) with parallel computing. Among parameters, the multipliers of primary nucleation ($\theta_{pri.,1}$ and $\theta_{\mathrm{ins.},1}$) show the insonation induced nucleation is basically about 500–1800 times faster than the stochastically generated nucleation. The exponent value ($\theta_{\mathrm{sec.},2}$ and $\theta_{\mathrm{sec.},3}$) of the suspension density of crystals and the concentration difference between bulk and saturated solution in secondary nucleation is reasonable when it compared with earlier correlation [113].

Table 8. Fitted kinetic parameters for the steady-state model of LAM crystallization.

Parameters	$\theta_{pri.,1}$	$\theta_{pri.,2}$	$\theta_{ins.,1}$	$\theta_{ins.,2}$	$\theta_{ins.,3}$
Units	$\frac{\#}{s\sqrt{K}}$	K^3	$\frac{\#}{s\sqrt{K}}$	K^3	–
0% amplitude	$10^{-8.57}$	217	–	–	0.814
30% amplitude			$10^{-5.32}$	57.4	
90% amplitude			$10^{-5.88}$	33.2	

Parameters	$\theta_{sec.,1}$	$\theta_{sec.,2}$	$\theta_{sec.,3}$	$\theta_{g,1}$	$\theta_{g,2}$
Units	$\frac{\#}{s \cdot \left(\frac{kg}{m^3}\right)^{\theta_{sec.,2}} \left(\frac{g_{solute}}{g_{solvent}}\right)^{\theta_{sec.,3}}}$	–	–	$\mu m/s$	K
0% amplitude	$10^{43.6}$	3.3	2.61	$10^{1.75}$	1000
30% amplitude					
90% amplitude					

Fig. 26 summarizes the comparison between experimental ECDF and model predicted ECFD. Generally, as the median length error is more substantial, the coefficient of determination (R square) is relatively small. Experiments with the dissolution process are not fitted well with observed data when they accompany ultrasonication induced nucleation. The predicted mean length of crystals at experiment 9 and 18 are 41.0% and 31.8% smaller than observed mean length, which means the effect of ultrasound on primary nucleation is overestimated when it is followed by the dissolution of crystals. Also, the model seems imperfect to the rapid decrease of the temperature inducing a high level of supersaturation. Under the environment, the small particles that look like precipitate are observed and are hard to be predicted with the population balance model because the kinetics of precipitation is significantly different from the nucleation kinetics. The measurements from other experiments implemented in the dissolution-free process and lower supersaturation correspond well to the results of the proposed model.

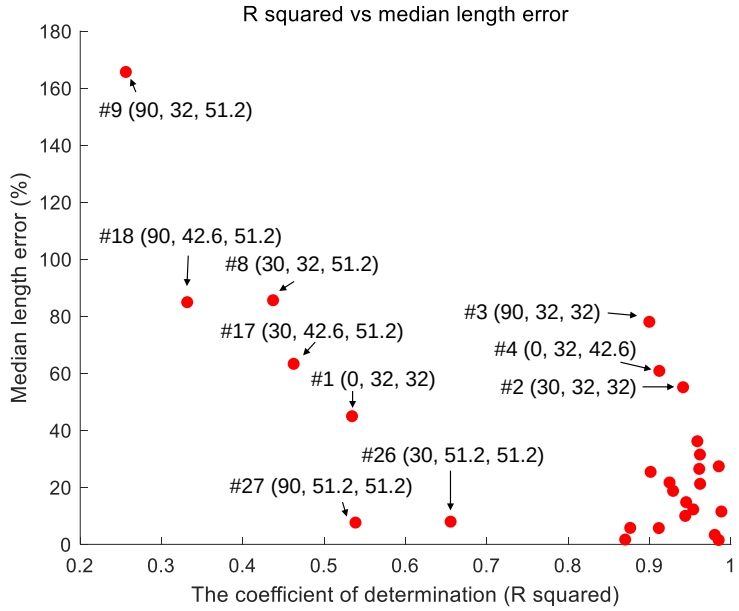

The numbers within the parentheses are amplitude of ultrasound, pre-HEX temperature, and HEX 1 temperature in order.

Figure 26. The R squared, and median length error between experimental ECDF and model predicted ECDF.

When comparing the predicted and observed data of crystals against 1:1 line with error line, most of the results from the model are fairly accurate with <20% prediction error except the outliers including dissolution process and high supersaturation condition (Fig. 27). The standard error (vertical error bar) of the properties of observed data which shows 99.7% confidence intervals (three sigmas) was calculated on a sampling basis. By repeated sampling on half of the whole and recording of properties (mean, standard deviation, median, and coefficient of variation) obtained, the sampling based distributions of the properties are estimated. The median lengths of crystals are less sparsely distributed than other properties of the product, which usually caused by skewness in the product CSDs (Fig. 27 (a) and (c)). The diverged data from 1:1 line in standard deviation are likely to be caused by an imperfection in the measurement technique and model misspecification (Fig. 27 (b)). Additionally, for intermediate ultrasonification activated experiments, the coefficient of variance is mostly smaller than the ultrasound-free crystals (Fig. 27 (d)).

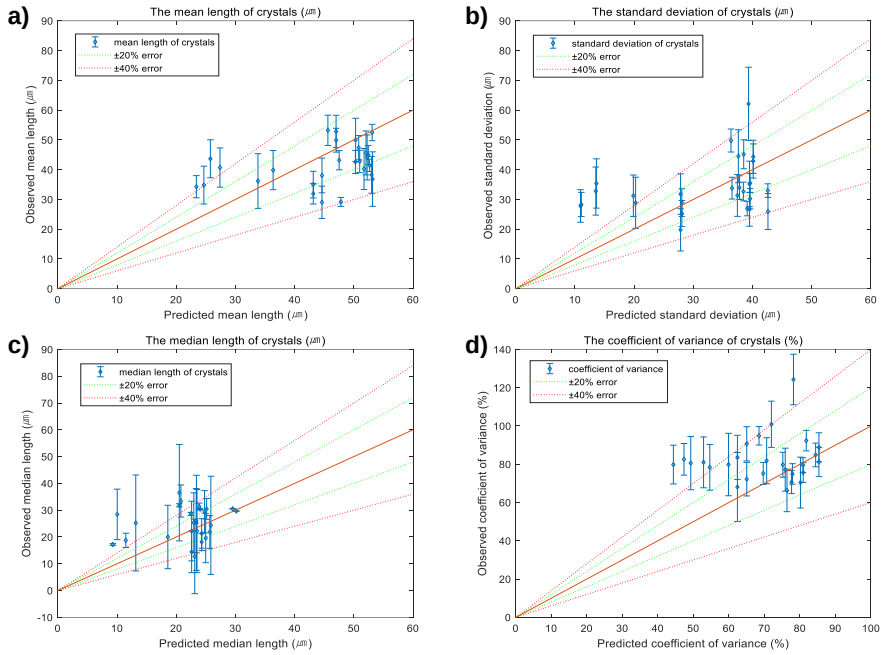

(a) the mean length of crystals, (b) the standard deviation of crystal length (c) the median length of crystals, and (d) the coefficient of variance of crystal length

Figure 27. Comparison of predicted and observed data against the 1:1 line with 20% and 40% prediction error line.

The temperature trajectory through slug-flow and CSD of representative experiments is shown in Fig. 28. The measured temperature from installed thermocouples is significantly coincident with the predicted values (Fig. 28 (a), (c), and (e)). Based on the profile, the solubility of the solution at overall slug-tube is estimated, and the population balance model is solved. At experiment 1, though the amplitude of ultrasound is zero, many observations are ranging from 0–50μm, which is attributed to precipitation induced by higher supersaturation as mentioned above (Fig. 28 (b)). The result of experiment 9 is opposite to the preceding case (Fig. 28 (d)). Since the temperature surge of the slug-flow in front of the HEX 1, the nuclei vigorously induced by the higher power of ultrasonication are dissolved, and the effect of ultrasonication is canceled out. In this case, the model does not sufficiently reflect the dissolution process, and the number of smaller size crystals in the distribution are overestimated. Except for the above cases, the proposed model predicts the distribution of product from continuous crystallizer operated under adequate cooling process without dissolution of crystals (Fig. 28 (f)).

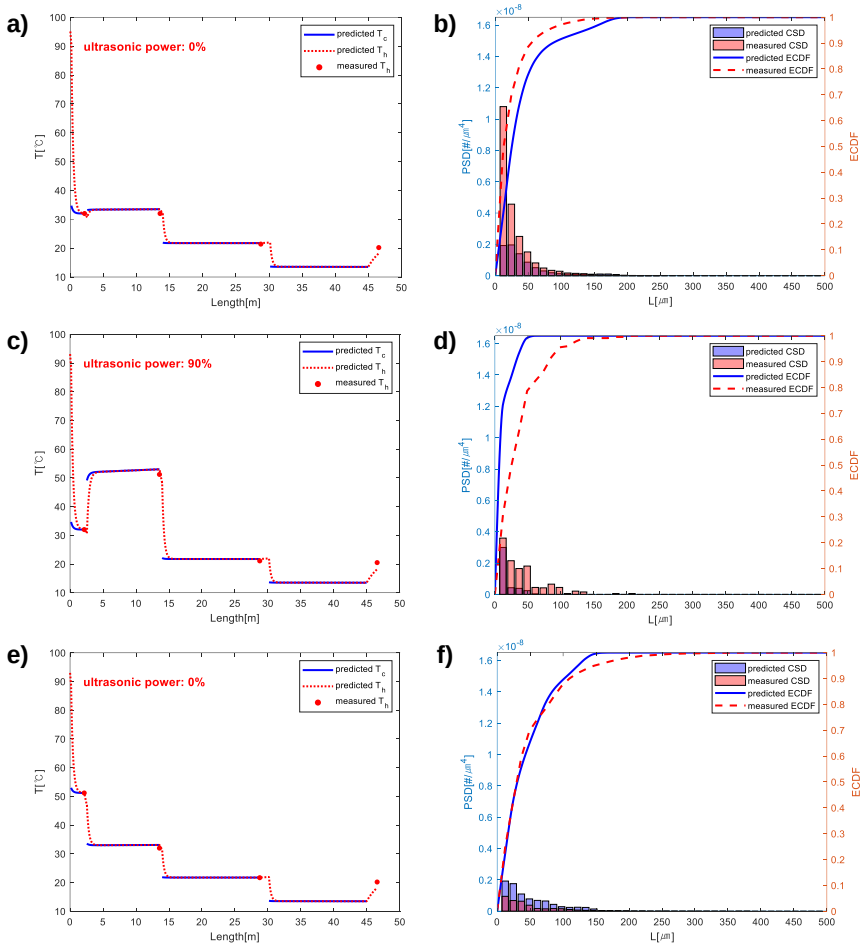

(a), (b): temperature trajectory and CSD (with ECDF) of experiment 1, (c), (d): temperature trajectory and CSD (with ECDF) of experiment 9, (e), (f): temperature trajectory and CSD (with ECDF) of experiment 19

Figure 28. The three representative graphs of the full-factorial design of experiments.

The graphs of the crystal size distribution show that the amount of crystals is reduced with the increase of crystal size. However, it is widely known, the analytic solution of the population balance model is one of the exponential functions [129]. Therefore, the solution should be graphed in log scale axis for advanced analysis. Because our experiments were done in lab-scale, the samples were not sufficient to be counted in log scale size. Also, our resolution of the camera used to take a picture of the microscope was not enough to capture the crystals whose size was smaller than 1μm, which makes the analysis in log scale difficult. I believe that the comparison of the distribution from an analytic solution and the result of the differential equation train done in this thesis can provide developed interpretation about this system.

4.3 Continuous crystallization of a protein: hen egg white lysozyme (HEWL)

4.3.1 Introduction

From an industrial perspective, an opportunity exists to develop scalable non-chromatographic protein separations methods that disrupt the traditional batch-wise paradigm and support continuous purification modes [130-132]. Despite efforts to demonstrate the future viability of sequential 'bind-and-elute' chromatography, resin-based adsorption processes are costly and widely perceived within the biomanufacturing sphere to be a major process bottleneck [130, 133, 134]. Recently, demonstrated methods such as periodic counter-current chromatography (PCC), simulated moving bed chromatography (SMB), and multi-column counter-current solvent gradient purification (MCSGP),

remove this bottleneck [135]. Each of these processes, however, employs more columns, valves, and pumps than sequential chromatography, substantially increasing both system complexity and capital equipment costs [131, 136, 137].

Furthermore, given that they require the same number of stages as sequential chromatography to achieve the same purification efficiency—but operate at higher throughputs using more resin—PCC, SMB, and MCSGP have OPEX costs that scale linearly with respect to conventional techniques. In contrast, non-chromatographic protein purification methods such as precipitation, aqueous two-phase extraction (ATPE), and crystallization are relatively simple to execute, require a small initial capital investment, and boast OPEX costs (primarily buffers/solvents) that scale sub-linearly with throughput [131, 135]. A single example of the application of each of these three techniques to continuous protein purification has been published [138-140]. In addition to reducing facility footprints, precipitation, ATPE, and crystallization have the potential to dramatically increase equipment utilization, allowing the biopharmaceutical sector to realize higher productivities and improved operational flexibility [131, 132, 135]. These methods could also support the robust control of short product residence times, allowing for the rapid recovery of labile protein and standardization of critical quality attributes across a lot of datasets [132, 135]. Finally, the improved purification efficiency gleaned by coupling these techniques with 'clean' expression hosts (e.g. K.phaffi), as well as their amenability to scale-out by parallelization, makes them all the more applicable to technologies like the InSCyT platform.

Despite its potential cost-effectiveness and scalability, however, the intrinsic difficulty of optimizing and controlling protein crystallization has stymied its

broad adoption as a preparative purification technique [135, 141]. Specifically, a generalized set of heuristics governing the myriad physical, chemical, and biochemical factors that can impact protein crystal nucleation and growth has yet to be realized [141-143]. Consequently, while a wide range of proteins has been crystallized at the μL scale for structure determination using various combinatorial screening approaches (e.g. sitting drop vapor diffusion, free interface diffusion, and dialysis), to date recombinant insulin LysB28ProB29 is the only biopharmaceutical reported to be purified by crystallization at the industrial scale [135, 144]. Studies surrounding the batch crystallization of enzymes (e.g. hen egg white lysozyme (HEWL), lipase) and monoclonal antibody fragments from both homo- and heterogeneous mixtures at volumes ranging from 100 mL to 1L represent promising demonstrations of this technique as a method for 'at-scale' purification, but fall short of proving industrial applicability [141]. Additionally, a recent set of experiments conducted by Neugebauer and Khinast provided the first evidence that tubular apparatuses were viable technologies for protein crystallization [140, 145]. Using a simple setup designed around disposable plastic components and syringe pumps, these authors reported the crystallization of HEWL from a purified solution at a rate of 0.72 g/h. This work, however, neither demonstrated robust feedback process control nor implemented online measurements to monitor crystallization progress in real-time. Additionally, the work was ended in experiments without the established model which can describe the overall continuous crystallization system reasonably. Therefore, sufficient intellectual space exists to leverage optimization/ control theory, build off prior art surrounding the tubular crystallization of small molecules and active

pharmaceutical ingredients, and develop a flexible flow-through system for the continuous crystallization of therapeutically relevant proteins under feedback control.

4.3.2 Experimental method

4.3.2.1 Materials and design of experiments

Hen egg white lysozyme was used as the model protein for all experiments as described. Buffer preparation also involved sodium acetate, hydrochloric acid, HPLC-grade distilled deionized water, and disposable 0.2 μm vacuum filtration systems. A 1 M solution of sodium hydroxide was used to flush the CCHEX crystallizer at the beginning and end of each day of experiments. Seed solutions for all experiments were prepared by first suspending HEWL in a refrigerated solution of 2 % w/v NaCl and 100 mM NaOAc (pH 4.0) to a concentration of 70 g/L. The suspension was then placed in a water batch held at 30 ^{o}C and stirred for 3.5 hours. The resulting hazy solution was subsequently vacuum filtered, placed back in the water bath, and allowed to cool spontaneously overnight. Before first use, the seed solution was heated to the appropriate temperature as indicated in Table 9.

Table 9. HEWL design of experiments parameters and set points.

Exp.	Rep.	Seed Bath T	Flow rates				Temperatures			
			Precipi. FR*	HEX 1	HEX 2	HEX 3	Pre-HEX	HEX 1	HEX 2	HEX 3
1	1	32.6	0	400	400	150	5	5	5	23
1	2	32.35	0	400	400	150	5	5	5	23
2	1	28.65	0	150	400	400	14	20	11	7
2	2	28.45	0	150	400	400	14	20	11	7
3	1	23.8	0	400	400	400	17	15	11	8
3	2	23.9	0	400	400	400	17	15	11	8
4	1	42	2.61	400	400	400	5	5	5	5

All temperatures are listed in units of °C. All flow rates are given in units of mL/min. T = temperature. FR = flow rate. *Precipitant was 15% w/v NaCl, 57.7 mM NaOAc, pH 4.0 buffer held at 3.0 °C.

Each of the four sets of experimental conditions tested was designed to expose HEWL transiting the continuous system to markedly different supersaturation conditions while holding the residence time of slugs constant. All temperature and the concentration of precipitant set points were determined with the aid of empirical models fitted to solubility data [146]. Specifically, experiment 1 was designed to 'crash cool' the HEWL solution immediately upon entering the pre-HEX module by exposing it to a maximum instantaneous supersaturation difference ($\Delta\sigma_{max}$) equal to ~18. Experiment 2 sought to reduce $\Delta\sigma_{max}$ to ~6.4 and promote dissolution in HEX 1 following primary nucleation in the pre-HEX. Experiment 3 was designed to expose slugs of dissolved and crystalline HEWL to a shallow temperature-and by extension, supersaturation-gradient with a $\Delta\sigma_{max}$ of ~4.3 in an effort to favor the growth of seed crystals relative to the nucleation of new particles. Finally, experiment 4 represented a situation in which $\Delta\sigma_{max}$ was varied aggressively (~220) using a combination of concentrated precipitant (i.e. NaCl) addition and crash cooling. Each of experiments 1 – 3 was performed in duplicate, while only a single replicate of experiment 4 was carried out. Given that the current understanding of macromolecular crystallization processes generally holds that supersaturations of ~10 – 100x above Csat are necessary for nucleation of protein crystals, the goal of varying $\Delta\sigma_{max}$ over 3 orders of magnitude was to establish the feasibility of tuning HEWL PSDs using the CCHEX [142]. Further, relative to experiments 1 – 3, experiment 4 was designed to exploit the generalized phase behavior of protein solutions, which predicts that extreme values of $\Delta\sigma_{max}$ will preferentially induce the formation of amorphous precipitates over well-ordered crystals [147]. In this way, disordered aggregates

of HEWL are generated intentionally as a control to aid in distinguishing crystalline from non-crystalline samples by both cross-polarized microscopy and PXRD.

4.3.2.2 Experimental apparatus

The system utilized to crystallize HEWL is identical to that documented in the thesis of Mozdzierz (Chapter 6), with the exception of an additional peristaltic pump fitted with platinum-cured silicone tubing driving the in-line mixing of a 0.2 μm-filtered 15% w/v NaCl, 57.7 mM NaOAc, pH 4.0 precipitant solution as depicted in Fig. 29 [3]. The precipitant pump was not integrated into the larger control system, preferably, in those instances when in-line precipitant mixing was manually set at the beginning of the experiment. The precipitant solution was stored in a magnetically stirred, jacketed, 1L, glass, two-necked round-bottom flask plumbed in series with the cold coolant reservoir and seed/feedstock solution Allihn condenser. The temperature controlled HEWL solution enters the crystallizer from the round-bottom flask at left and traverse a short segment of insulated tubing before transiting through the pre-HEX and mixing with a slipstream of concentrated, chilled, and buffered NaCl. The mixture of HEWL and precipitant then traverse under an indirect insonation probe and mixes with filtered air to form stable liquid slugs. The slugs then move through HEXs 1, 2, and 3 prior to being collected for imaging and PXRD analysis at the outlet. For all experiments that did not employ concentrated precipitant addition, the air and liquid flow rates into the slugging tee were both 7 mL/min. The air and liquid flow rates into the slugging tee during experiments that involved concentrated precipitant addition were 7 and 9.61 mL/min, respectively. The flow rate through the shell-side of the pre-

HEX was determined by the MPC algorithm and varied throughout the course of an experiment. Additionally, for the other HEXs, the shell-side flowrate from the peristaltic pumps are given by the classical proportional-integral (PI) controllers to achieve the set point of temperature.

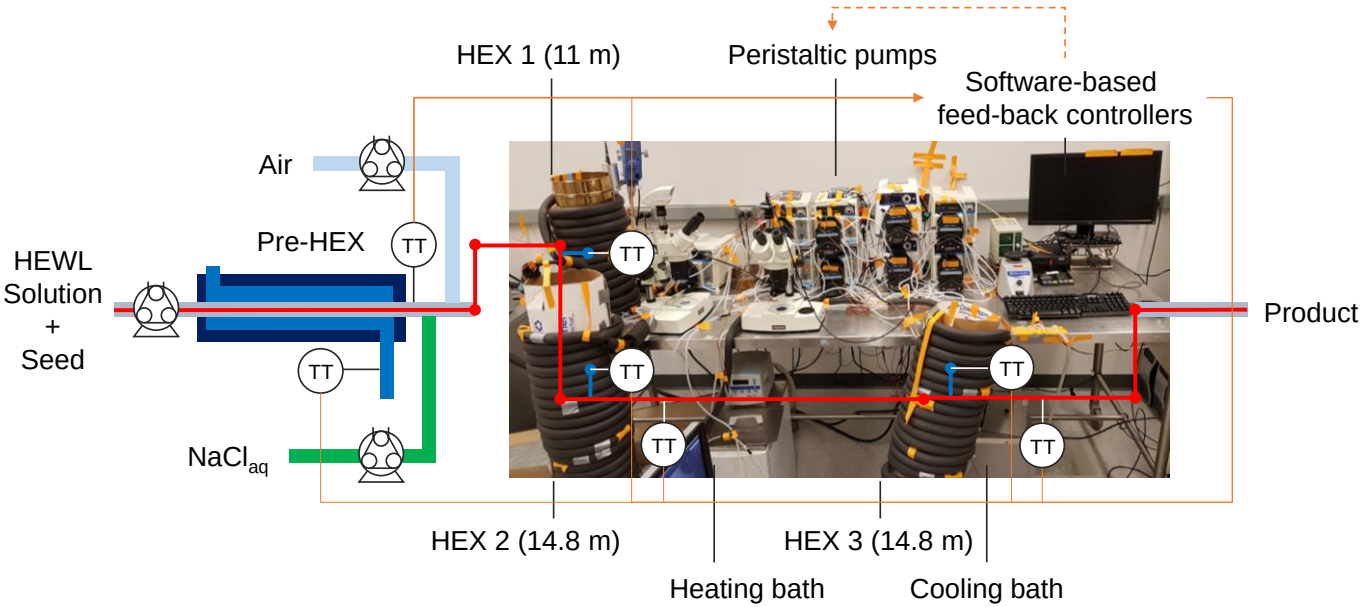

Figure 29. A pictorial illustration of the continuous crystallizer with in-line precipitant mixing capabilities.

4.3.2.3 Measurement of particle size distribution

For each experiment, a single pulse of HEWL (Table 1) was fed into the continuous crystallizer. Pulses of air (each 10 s long) bracketed the HEWL to aid in identifying crystal-containing slugs at the outlet. All slugs of HEWL were collected as they exited the crystallizer in a single sterile 50 mL conical tube. Four 45 μL droplets of the collected slurry were immediately transferred to an air-dusted microscope slide and protected from evaporation with cover glasses. A set of position matched images of each droplet was then acquired using a microscope fitted with a digital camera, a 10X trinocular eyetube, and 4X/0.10 HI PLAN objective. The resolution of this optical setup was 1 μm/pixel. Light intensity, aperture, and condenser settings were kept constant across all images and all experiments.

Each of the four cross-polarized micrographs corresponding to a given experiment was analyzed using the watershed algorithm with markers and boundaries described in Fig. 30. First of all, the original color image is mapped to grayscale for adjusting the contrast. The adjusted image is dilated with a structuring element neighborhood where pixels are connected along the horizontal or vertical direction for protecting tiny size crystals from eroding process. The boundaries of segmented objects are calculated in pixels and separate the threshold of regions for the watershed method. The foreground markers in the objected are obtained by a closing followed by erosion and are superimposed on the grayscale image with the boundaries of regions. The magnitudes of markers are modified to regional minima of the objective region and scaled to different integer values. The flooding process is performed from the marker (the regional minima), and the borderline is constructed between the

extended regions of different labeled markers. Finally, the area and length of crystals are estimated and used to acquire particle size distribution.

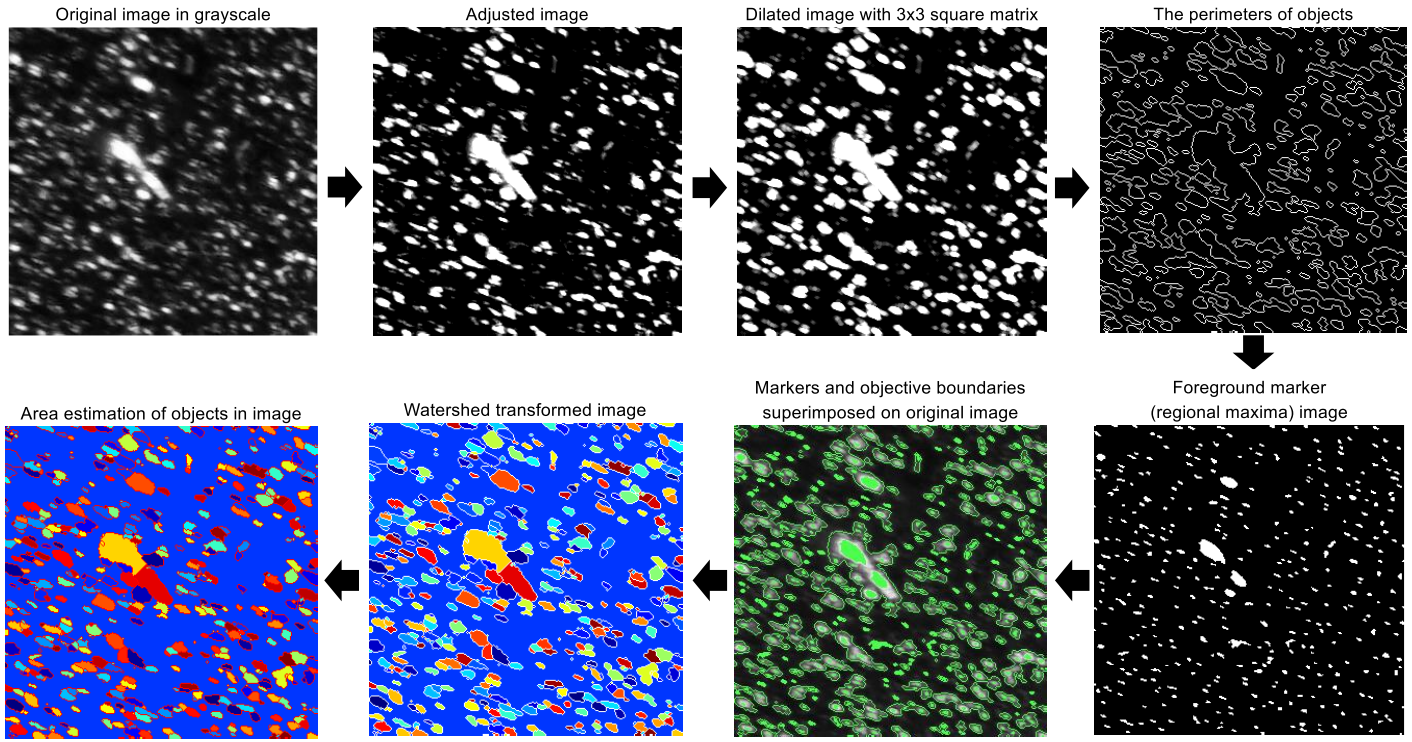

Figure 30. Graphical summary of the image processing algorithm which is a modified version of marker-controlled watershed segmentation for sorting out overlaid crystals.

4.3.2.4 Powder X-ray diffraction

Approximately 10 minutes after collection (the time required to perform all imaging described in section 4.3.2.3), the remaining slurry from a given experiment was divided into 12 – 15 x 1.0 mL aliquots and centrifuged at 10,000 x g and 22 ºC for 2minutes. The resulting supernatant was subsequently aspirated off and discarded. A second identical centrifugation step was employed in the case when bulk liquid remained after aspiration. Pellets were then stored under ambient conditions for ~4 hours prior to analysis by PXRD.

PXRD was performed using a PANalytical X'Pert PRO diffractometer. The instrument was configured as described in the study of *Siepermann* and operated at a tension of 45 kV and an anode current of 40 mA [148]. All scans were conducted under the following programmable settings to maximize resolution at low angles: 3.507º – 13.5º 2θ range; 0.0167113º step; 455.295 s step time; 0.004661º/s scan speed; and 1 rps spinner stage rotation speed. Each scan analyzed the equivalent of at least 8 pellets pressed onto a zero-background sample tray. A blank sample tray diffractogram was acquired under these same settings.

A negative control diffractogram of the 2% w/v NaCl and 100 mM NaOAc (pH 4.0) buffer used to prepare all HEWL solutions were obtained using the same instrument and hardware configuration noted above. 75 mL of the buffer was first boiled on a hot plate under stirring for 2 hours to evaporate most of the bulk liquid. The remaining slurry was then dried in a vacuum oven overnight to yield a powder of crystalline NaCl and NaOAc in a mass ratio identical to that in the original buffer. Given that inorganic molecules typically

give PXRD signatures at 2θ range; 0.1° step; 382.27 s step time; 0.0333°/s scan speed; and 1 rps spinner stage rotation speed.

4.3.3 Results and discussion

4.3.3.1 Protein crystal population

The image in each set was acquired using cross-polarized light and yielded the representative images shown in Fig. 31. Particles of HEWL that appear white exhibit anisotropic long-range order are birefringent and are very likely crystalline [149]. Particles that appear dark are either amorphous precipitates of HEWL or crystals possessing a cubic (*i.e.* isotropic) lattice instead of the desired tetragonal structure. In micrograph of experiment 3, the numerous small dark particles observed indicate the precipitates were included in the seed of associated experiment. The lower temperature of the bath for prompting appropriate supersaturation gradient at the starting point of system($\Delta\sigma_{max}$: ~4.3) makes the higher supersaturation environment at the bath of feedstock and seed which causes the formation of a precipitate at the seed (Fig. 31 (c.1)). Certainly, the well-grown crystals are also discovered in the outlet of experiment 3, but most of background is full of amorphous precipitates not responded by cross-polarized light (Fig. 31 (c.2)).

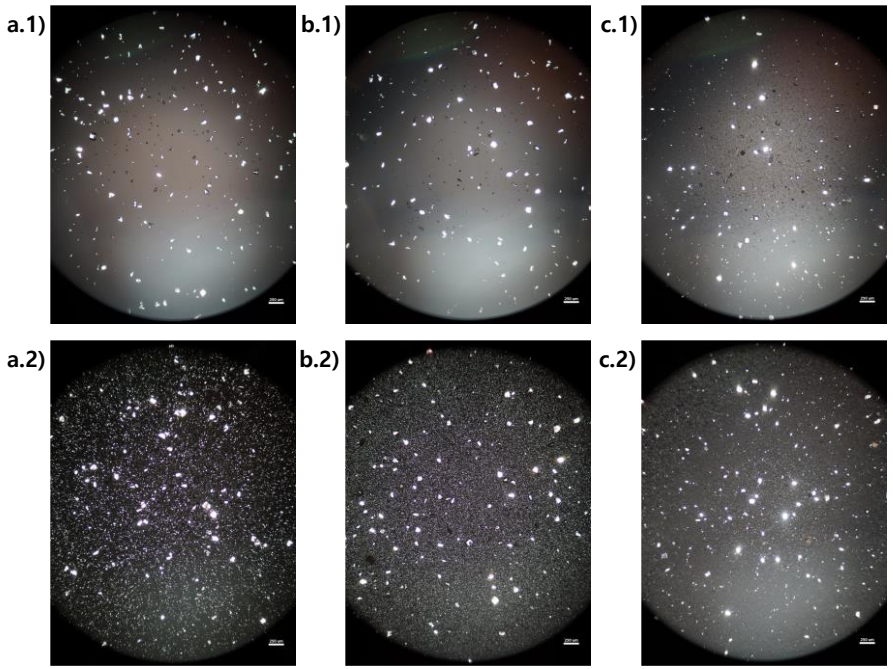

The upper image in each set is representative of the seed PSD used in the associated experiment. The lower image in each set is representative of the outlet PSD generated by the associated experiment. All images were acquired under cross-polarized lighting conditions using identical microscope aperture, condenser, and magnification (40X) settings. a.1) Seed of experiment 1. a.2) Outlet of experiment 1. b.1) Seed of experiment 2. b.2) Outlet of experiment 2. c.1) Seed of experiment 3. c.2) Outlet of experiment 3.

Figure 31. Representative micrographs from HEWL DoE experiments 1-3.

The experiment 4, as extremely high $\Delta\sigma_{max}$ case, yielded only amorphous precipitate as predicted (Fig. 32). The crystalline is hardly observed in seed and outlet at both images acquired under cross-polarized and plane polarized light. The higher temperature condition in feedstock causes the dissolution of particles in the bath, which disturbs the formation of nuclei and tiny crystals attributed to secondary nucleation. The rapidly occurring precipitation is typically not affected by the existence of solute crystalline and thus does not involve secondary nucleation [113].

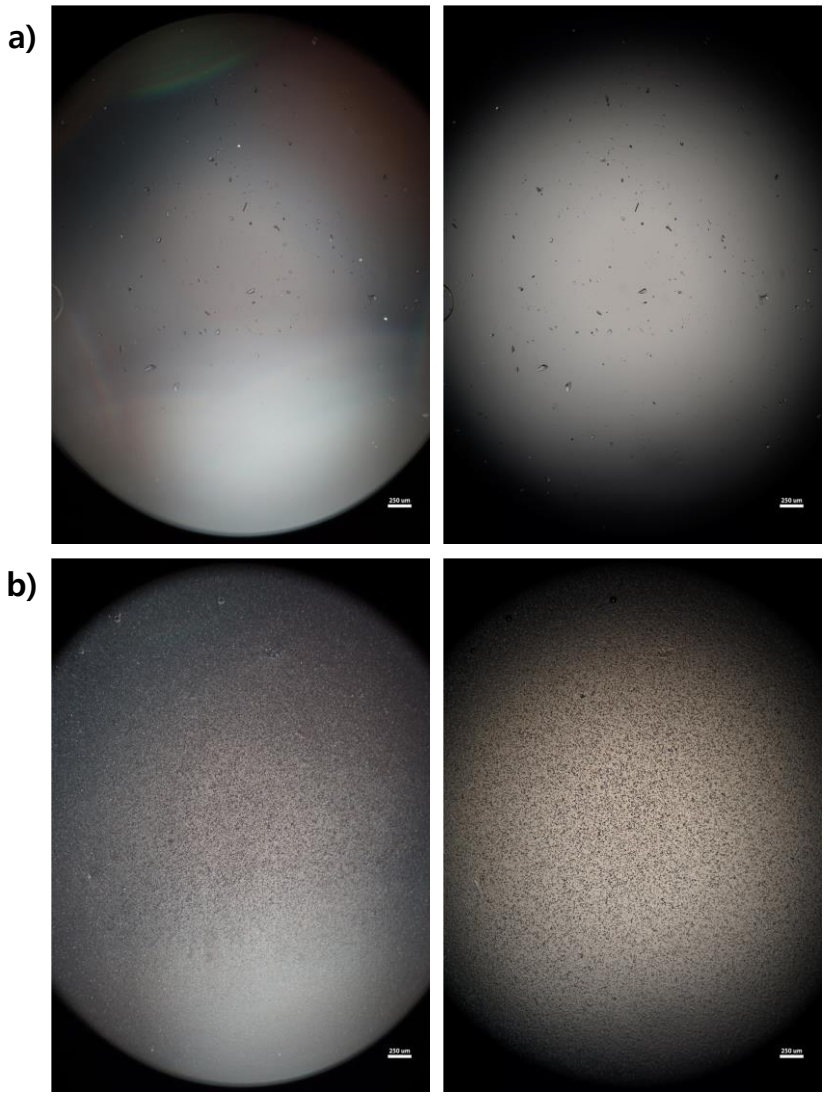

The left image in each set was acquired under cross-polarized lighting conditions, while the right image was captured using plane polarized light. The crystal sample as not repositioned between image acquisitions. Identical microscope aperture, condenser, and magnification (40X) settings were used for all four images. a) Seed. b) Outlet.

Figure 32. Representative micrographs from HEWL DoE experiment 4.

With the image process circumstantially described in section 4.3.2.3, the representative micrographs of experiment 1, 2, and 3 are analyzed and estimated for acquiring PSDs of generated crystalline and nuclei. The experiment 4 where the precipitation process majorly occurs and any particles appearing in white are not observed are excluded from the analysis (Fig. 32). Taken collectively, Fig. 33 provide convincing evidence that even over residence time as short as 25 – 30 minutes, the continuous protein crystallization system can be used to tune the characteristics of protein crystal populations. The upper plots depict histograms of the overall seed (left y-axis; blue bars) and outlet (right y-axis; orange bars) PSDs associated with a given experiment (summation of replicate thereof). As mentioned in section 4.3.2.3, only particles that exhibited high-intensity constructive interference under cross-polarized light (Fig. 31) were considered crystals to calculate these PSDs. The lower plots show the ECDF for the corresponding matched histograms on a standard set of axes.

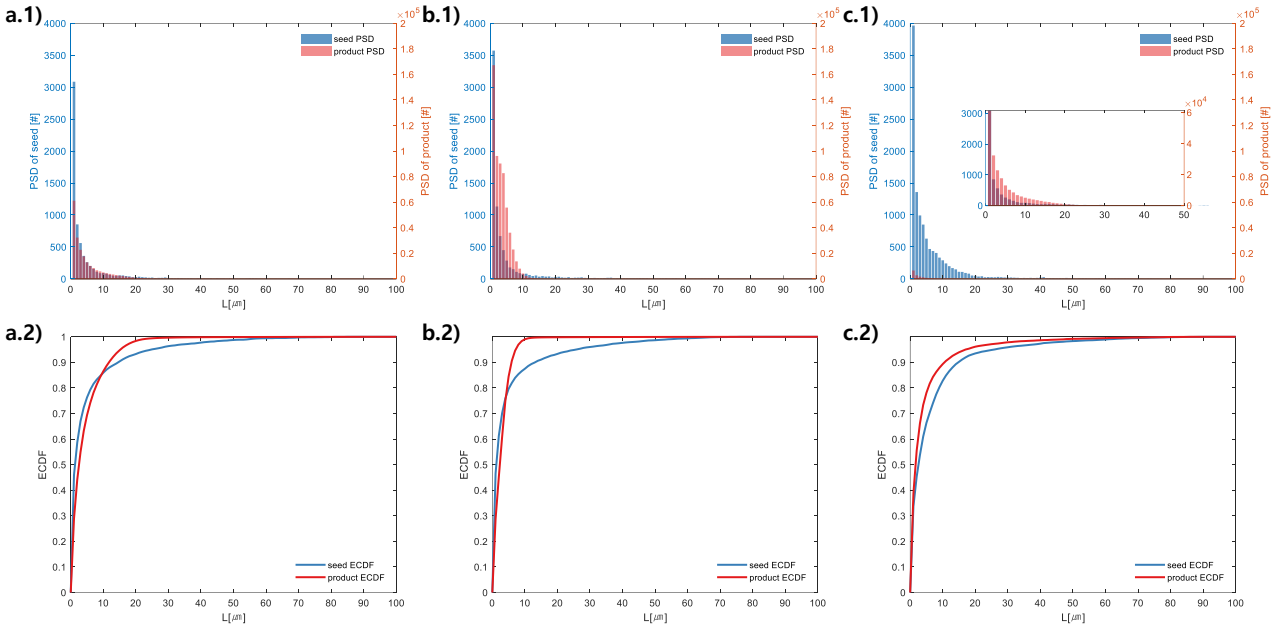

a.1, b.1, and c.1 are PSD of seed and product for experiment 1, 2, and 3, and a.2, b.2, and c.2 are ECDF of experiment 1, 2, and 3, respectively.

Figure 33. Particle size distribution of seed and product (upper) and estimated cumulative distribution function (lower) generated by the associated experiments.

Continuously differentiable analytical expressions for these ECDFs were fitted using piecewise cubic Hermite interpolating polynomials and were used to calculate the summary statistics given in Table 10 via equations

$$f(L) = n(L)/N_T \tag{4-23}$$

$$\bar{L}_{p,0} = \int_0^\infty L^p f(L) dL, \tag{4-24}$$

where $f(L)$ is the number normalized PSD and $\bar{L}_{p,0}$ represents various population-weighted mean measures of crystal size [150].

Comparing plots of Fig. 33, it is immediately apparent that the crystallization conditions tested in experiment 1 and 2 yielded markedly different final PSDs than those employed in experiment 3. Indeed, the leftward shift of the ECDFs for experiments 1 and 2 from relatively heavy-tailed seed populations to substantially more monodisperse final distributions of small crystals (L < 30 μm) suggests that at an initial $\Delta\sigma_{max} \geq 5$, nucleation of new HEWL crystals favored the overgrowth of existing particles. In contrast, little shift and subsequent broadening of the ECDF for experiment 3 from the inlet to the outlet clearly points to growth being favored over nucleation at $\Delta\sigma_{max}$ values within ~400% of C_{sat}.

Table 10. Summary statistics for seed and product populations used in HEWL DoE experiment 1 – 3.

	Experiment 1		Experiment 2		Experiment 3	
Moment	Seed	Product	Seed	Product	Seed	Product
N_T	6.7×10^3	2.1×10^5	7.6×10^3	5.8×10^5	1.2×10^4	1.7×10^4
$\bar{L}_{1,0}$	5.7	5.0	5.4	3.3	6.8	4.9
$\bar{L}_{2,0}$	1.3×10^2	5.5×10^1	1.3×10^2	1.9×10^1	1.6×10^2	9.3×10^1
$\bar{L}_{3,0}$	5.7×10^3	1.1×10^3	5.4×10^3	3.1×10^2	7.4×10^3	3.9×10^3

N_T is the total number of crystals in a given experiment (summation of replicate thereof). Similarly, $\bar{L}_{1,0}$, $\bar{L}_{2,0}$, and $\bar{L}_{3,0}$ are the population weighted mean crystal length (μm), surface area (μm^2), and volume (μm^3) in a given experiment, respectively. All population weighted mean size statistics were calculated using moments of the analytical derivatives of the ECDFs reported in Fig. 5. All N_T values were determined directly from the PSDs reported in these same figures.

These conclusions are also borne out by the summary statistics listed in Table 10. Given that all PSDs were acquired from consistent total volumes of well-mixed slurries, the fact that $\frac{N_{T,product}}{N_{T,seed}} > 10$ for experiments 1 and 2 and ~ 1 for experiment 3 implies that the former two experiments produced a larger number of smaller crystals than the latter experiment. Further, in the case of experiments 1 and 2, nucleation appears to be so strongly favored that the number of new small crystals formed is on the same order (10^5) as the volume of the largest observed crystals, causing a drastic decrease in $\bar{L}_{3,0}$ ($<$ 0.2x)between the inlet and outlet of the system. The observed 0.5x decrease in $\bar{L}_{3,0}$ between the PSDs of experiment 3, coupled with the substantial proportion of large crystals, signals that a large fraction of seed crystals ultimately grew to major axis lengths. However, the less number of small particles than experiment 1 and 2 implies secondary nucleation process rarely occurred and the precipitation process took place. These facts are also discovered in Fig. 31 (c.2). The lump of dark particles generated by aggregation of small size crystals composes the background of the micrograph.

The ability of the platform to exert even subtler control over protein crystallization is evident in a comparison of experiments 1 and 2. Specifically, despite the ~3x difference in $\Delta\sigma_{max}$ between these two sets of conditions, the data plotted in Fig. 33 show a few clear differences. A close inspection of Table 10 illustrates that although the two aforementioned experiments employed similar seed populations and yielded comparable numbers of crystals at the crystallizer outlet, $\bar{L}_{2,0,product}$ and $\bar{L}_{3,0,product}$ were all roughly 2x smaller for experiment 2 versus experiment 1. This result likely reflects the use of HEX

1 as a dissolution stage during experiment 2 and supports the claim that the unique ability of the system to robustly control the temperature trajectory through which a slug journey is valuable from a molecular processing perspective.

4.3.3.2 Structural characterization of HEWL

PXRD was employed as an orthogonal method to assess the qualitative crystallinity of all samples generated and confirm the results of cross-polarized microscopy. Fig. 34 plots low angle diffractograms for each of experiments 1 – 4 from top to bottom. Where appropriate, diffractograms for replicate experiments are plotted on common axes. Additionally, an idealized powder diffractogram (bottom panel; purple line) for tetragonal HEWL served as a reference. All samples collected at the outlet of the crystallizer during experiments 1 – 3 exhibit relatively defined diffraction peaks that match reference peak positions to within $\pm 0.5^{o}$ 2θ, suggesting that a substantial fraction of the particles formed in each run was crystalline tetragonal HEWL. This small offset in 2θ can likely be attributed to the higher resolution and signal-to-noise ratio of single-crystal to powder XRD [151]. Differences in the number of structure bound water molecules between samples could also convolute the traces. The systematic translation in 2θ evident between each pair of traces for experiments 1 – 3 is the result of small ($O(mm)$) differences in the positioning of each sample within the focusing circle of the diffractometer [152]. While the PXRD data unequivocally corroborate the formation of crystals in experiments 1 – 3, all six diffractograms exhibit a broad parabolic baseline (‘halo’) that indicates the presence of additional undesirable amorphous or short-range ordered nanocrystalline phases of matter [153].

Although techniques for estimating the relative ratio of amorphous to crystalline material in PXRD traces exist (*e.g.* the Rietveld method), they are generally regarded as being difficult to implement and subject to large uncertainties [154]. A comparison of the top three panels of Fig. 6 to the black trace (Exp. 4; confirmed amorphous precipitate) in the bottom panel of the said figure, however, bolsters the claim that experiments 1 – 3 yielded HEWL particles exhibiting significant crystalline character. It should be mentioned that HEWL analyzed as received from the manufacturer (Fig. 34; bottom panel; gray line) also produced a purely amorphous diffractogram. This result is significant, in that it demonstrates the utility of end-to-end seed population preparation and crystallization process for generating long-range ordered protein particles from otherwise disordered precursor materials.

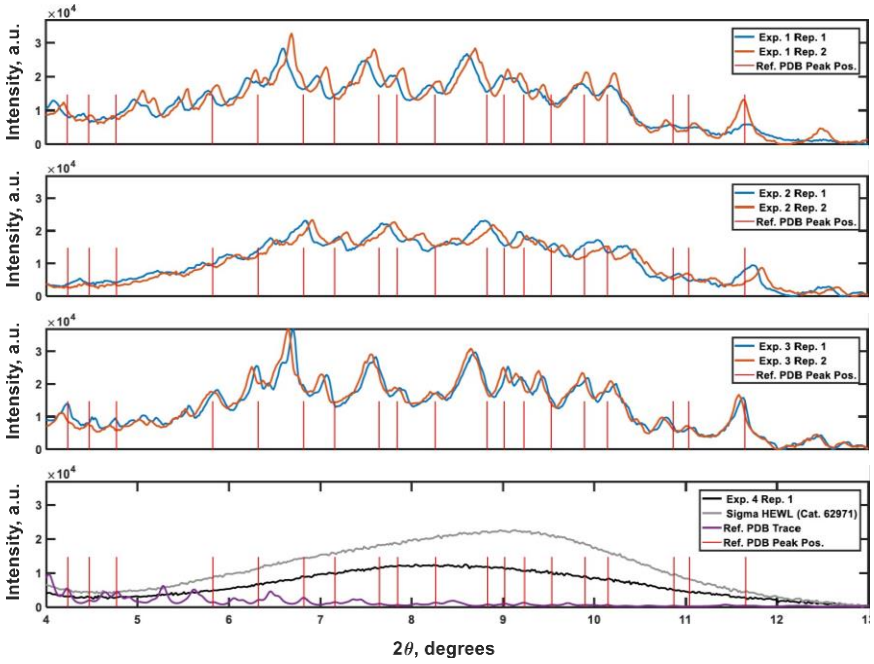

As noted in the legends, plots 1 – 3 (top to bottom) present the PXRD traces gathered for material generated in HEWL DoE experiments 1 – 3, respectively. The 4th plot presents reference non-crystalline spectra for manufacturer-supplied HEWL, and HEWL intentionally precipitated out of solution using the CCHEX platform (black; Exp. 4). The purple trace in the bottommost plot is an idealized PXRD diffractogram calculated using publicly-available single-crystal XRD data banked in the RCSB Protein Data Bank (ID: 3wun). The vertical red lines in each plot correspond to the positions of a subset of the critical peaks in the idealized PXRD trace. The intensity of these lines is arbitrary.

Figure 34. Powder X-ray diffraction traces characterizing the crystallinity of samples generated during the HEWL DoE.

Lastly, negative control diffractograms for a blank sample tray and vacuum dried HEWL dissolution buffer are presented in Fig. 35. The diffractogram for the blank sample tray exhibits a flat baseline for $2\theta \geq 3^{o}$. Similarly, the HEWL dissolution buffer diffractogram exhibits only a single peak within the range $9.5^{o} \leq 2\theta \leq 10^{o}$, which is characteristic of NaOAc. These controls indicate that neither the dissolution buffer nor the sample tray is expected to obscure the PXRD peaks of HEWL under the measurement conditions employed [155].

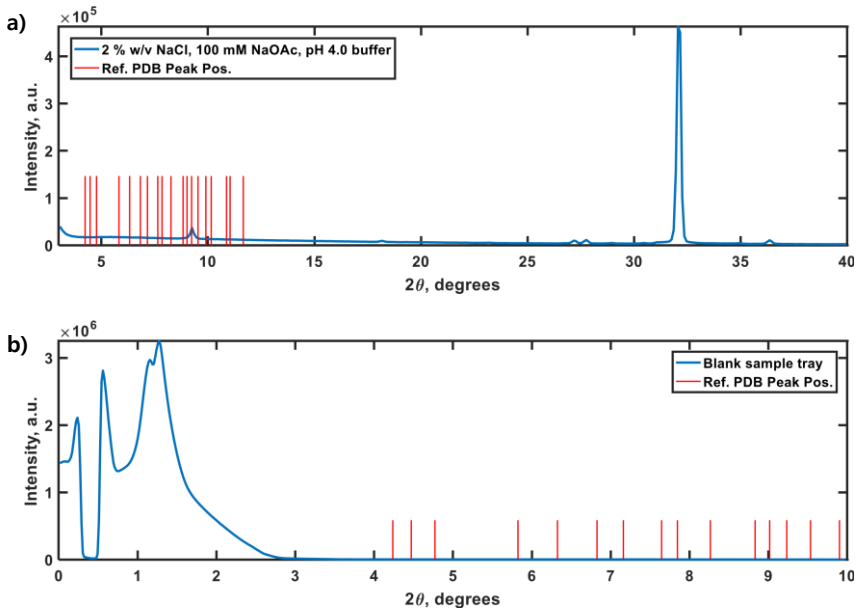

The vertical red lines in each panel correspond to a subset of the critical peak positions in an idealized diffractogram calculated from single-crystal XRD data for tetragonal HEWL (PDBid: 3wun). a) The doublet at ~ 27.5° $2\boldsymbol{\theta}$ are characteristic of NaCl. The low intensity peak at ~ 9° $2\boldsymbol{\theta}$ is characteristic of NaOAc (and is subject to shift above 10° $2\boldsymbol{\theta}$ due to variations in molecular hydration). b) The high intensity baseline below 3° $2\boldsymbol{\theta}$ is likely the result of direct beam scattering off of the sample tray itself at these extremely shallow angles.

Figure 35. Control PXRD diffractograms of (a) HEWL dissolution buffer and (b) zero-background sample tray.

4.3.3.3 Population balance model and parameter estimation

The mathematical model of continuous protein crystallizer is developed to verify and simulate the PSD and ECDF obtained by watershed segmentation method (Fig. 33).

A thermodynamic model for predicting temperature profile on a traverse of HEWL solution should be coupled with a kinetic model composed of secondary nucleation and crystal growth. The effect of primary nucleation on crystalline formation is negligible compared with secondary nucleation. Also, the HEWL crystallization process is operated with the initial population

$$f(L, z = 0) = \alpha \mathbf{f_{seed}} \tag{4-25}$$

of feed in the feedstock, which is given by image analysis step (section 4.3.2.3). In Eq. 4-25 α is a calibration factor for adjusting the total number of population. The correlation between HEWL solubility and temperature are empirically obtained by polynomial fitting with measured data [146]. The details of the model are described in section 4.2.2.

Only the results from the experiment 1 and 2 are applied to the model for guaranteeing the conservation the total mass including HEWL solute mass in bulk solution and the number and size of the protein crystals (Exp.3; precipitates are present). With parameter estimation with ordinary least square, the parameters of kinetic are calibrated and suitable for simulating the formation of HEWL crystalline in the continuous platform. In total, seven parameters are used to minimize the error between the developed model and observed data. Two parameters for seed population are used for adjusting the

mass balance of experiment 1 and 2; three parameters for secondary nucleation (Eq. 4-13); and the others for crystal growth equation (Eq. 4-15) are estimated and listed at Table. 11.

Table 11. The seed calibration and kinetic parameters estimated using data from experiment 1 and 2.

	Seed calibration (Eq. 4-25)		Secondary nucleation (Eq. 4-13)			Crystal growth (Eq. 4-15)	
Parameters	$\alpha_{Exp.1}$	$\alpha_{Exp.2}$	k_N	j	n	K_1	K_2
Units	–	–	$\frac{\#}{s \cdot \left(\frac{kg}{m^3}\right)^j \left(\frac{g_{solute}}{m^3}\right)^n}$	–	–	μm/s	K
Values	$10^{-8.72}$	$10^{-7.18}$	$10^{-0.58}$	4.21	1.82	$10^{1.26}$	0.83

The results of the simulation are compared with observed data points and sample distribution in Fig. 36. The constructed temperature profile based on the thermodynamic model of CCHEX and uninsulated intermediate slug-tube is reasonably well fitted to the data point except one outlier at experiment 2 caused by underestimation of the length of the uninsulated region at the outlet or heat transfer between slug-flow and ambient air (Fig. 36 (a.1) and (b.1)). The disconnected regions of blue lines indicate the boundaries of the short segments of uninsulated tubing connecting CCHEX modules. The dotted line in Fig. 36 (a.2) and (b.2) obtained by the random sampling in outlet solution. The mean distribution of 8 samples is used in order to estimate the parameters in Table. 11, but the results are compared with overall sampling data. The continuous crystallizer model predicts qualitatively similar ECDFs at both experiments and fits the experimental data reasonably closely. In Fig. 36 (b.1) and Fig. 36 (b.2), the dissolution effect of nuclei and crystals from the pre-HEX to HEX is estimated and propagated to the sharp PSD at the outlet, which shows the model is quite capable of predicting the drastic decrease and increase of the temperature in slug-flow; the level of supersaturation based on solubility difference in solution; and the influence of temperature reversal on the product specification.

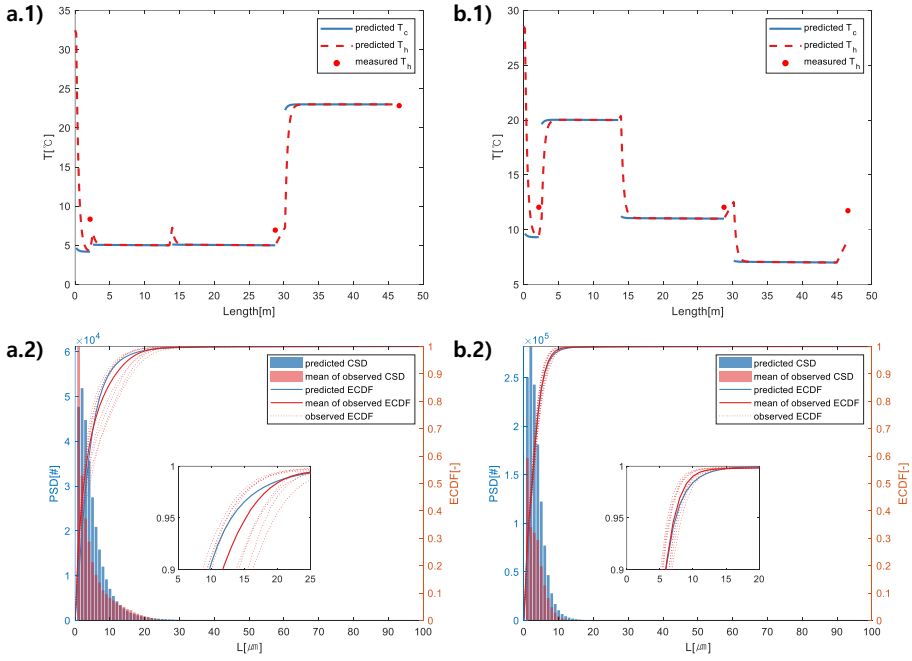

The dotted red lines in bottom plot represent the constructed ECDF from each sample (8 samples per experiment). a.1) and b.1) temperature profiles on slug-flow of experiment 1 and 2. a.2) and b.2) PSD and ECDF for experiment 1 and 2.

Figure 36. The temperature trajectory through slug-flow and particle size distribution with an estimated cumulative distribution function for each experiment.

4.4 Conclusion

4.4.1 Mathematical model of continuous crystallizer

This thesis proposes the mathematical model of continuous tubular crystallizer that exploits modular counter-current heat exchangers and indirect ultrasonication to manipulate nucleation and growth process. The 27 fully automated experiments are performed under hydrodynamically stable slug-flow, and real-time process control to crystallize L-asparagine monohydrate. The population balance model coupled with thermodynamic containing first-principle kinetic model is fitted to the results of a full factorial design of experiments.

From the length distribution of crystals obtained from the image process algorithm (section 4.2.1.3), the effects of the temperature trajectory of slug tube and the amplitude of indirect ultrasonication on the crystal generation are observed. The primary nucleation is effectively induced by ultrasound under the lower level supersaturation environment, and the high uniformity of smaller crystals are formed with increasing the power of ultrasound, which is consistent with past studies [103, 128]. Additionally, the product crystals generated by intermediate dissolution process caused by the reversal of temperature have about 5 %–24% wider size distribution or are 5 %–12% smaller in mean length regardless of ultrasonication.

With the estimated parameters, the mathematical model reasonably predicts the crystal length distribution close to the sample dispersion for <20% prediction error without dissolution process of crystals and precipitation. The effects of ultrasonication on mean length and variation are also appeared in the proposed model and verified with the sample distribution.

The population balance modeling of tubular crystallization on the basis of the first principles facilitates the comprehension about the effects of the cooling process and insonation on crystallization process; the precisely controlled continuous crystallization for manufacturing the tightly qualified product; and further development and design of process based on optimization and evaluation of the model.

4.4.2 Tunable continuous protein crystallization process

A continuous slug-flow crystallizer comprising reconfigurable, feedback controlled, counter-current heat exchangers and designed for the purification of small-molecules is applicable to mediating protein crystallization protein. An abbreviated design of experiments using hen egg white lysozyme as the model protein showed that, under the appropriate buffer and pH conditions, particle size distributions could be reproducibly manipulated using temperature gradients alone over a residence time of only 25 – 30 minutes. Moreover, the formation of XRD-crystalline particles of HEWL was robust to maximum relative supersaturation gradients spanning two orders of magnitude, but that $\Delta\sigma_{max}$ values ≥ 5 favored the nucleation of new crystals over the growth of existing ones. In addition, the in-line mixing of the concentrated precipitant solution allowed $\Delta\sigma_{max}$ values as large as 220 to be achieved in concert with steep temperature gradients. Preliminary work indicated that $\Delta\sigma_{max}$ of this magnitude overwhelmingly favored the formation of amorphous precipitates. Finally, the mathematical model combined with thermodynamic and population balance model is verified with the multiple observation from the DoE, which

provides substantial evidence that the fully automated system is largely agnostic to the physicochemical properties of the crystallization at play.

Future work in this space would likely involve more detailed DoEs that provide a finer resolution on the tuning of HEWL PSDs with the development of the mathematical model. System expansions that support longer residence times consistent with other recently demonstrated crystallizers in the literature are another obvious avenue worth exploring. Lastly, first-in-class experiments showing the crystallization of biopharmaceuticals under CCHEX modulated cooling conditions would provide compelling evidence for integrating platforms such as the proposed process with continuous bioreactors facilitate genuinely flow-through purification schemes.

Chapter 5

Multi-compartment model of high-pressure autoclave reactor for polymer production: combined CFD mixing model and kinetics of polymerization

5.1 Introduction

The ethylene–vinyl acetate (EVA) polymerization process has been used for many years because of the broad applicability and stress-crack resistant characteristics of the product copolymer. The EVA copolymer is used in the wire and cable industry, as a packaging film and a hot melt adhesive, and also in drug delivery devices [156, 157]. As the vinyl acetate (VA) content of the copolymer increases, the toughness and clarity increase but the stiffness and surface hardness decrease [158]. The reaction is typically carried out in a high-pressure autoclave reactor at pressures ranging from 1300 to 3000 kg/cm^2 and temperatures from 150 to 300 °C, and this setup is widely preferred over the use of a tubular reactor to produce resin with a high VA concentration [159, 160]. The average molecular weight, molecular weight distribution, and short and long chain branching indexes, which determine the product properties, can be changed by manipulating several operating conditions in the autoclave reactor, such as the temperature, pressure, initiator, and chain-transfer agent concentration [161]. To maintain the temperature of ethylene and vinyl acetate monomers in the reactor within the desired range, it is essential to keep the EVA polymerization reaction, which is highly exothermic, under strict control. For

this reason, theoretical models of the polymerization process have been developed to allow the prediction of polymer properties under given operating conditions. For example, the kinetic mechanism of free-radical polymerization has been proposed in earlier studies, and the method of moments has been used for the calculation of molecular-weight averages [162-164]. In addition, the polymerization kinetic model represented by moments has been combined with a multi-zone reactor model in which each zone is considered to be a well-mixed continuous stirred-tank reactor (CSTR) for the calculation of the temperature distribution from reactor top to bottom [165-168]. However, in these studies, the zones were directly arranged from the inlet to outlet because the flow pattern was unknown; thus, the back-mixing flowrate from the lower to the upper zones was determined by the user. However, the flow pattern induced by the stirrer can be efficiently solved and analyzed using computational fluid dynamics (CFD), and there are several earlier examples of the simulation of low-density polyethylene (LDPE) production in a high-pressure autoclave reactor using CFD models. The mixing and reaction were coupled by solving the polymerization kinetics, mass balance, and energy balance simultaneously. The results of the coupled model reveal an initiator concentration profile close to the inlet, as well as the axial temperature profile inside the reactor, but the proposed model was not validated and was computationally costly [169-172]. In particular, it is challenging to use CFD models for stability analysis with a sufficient number of cells, even though this is necessary to provide spatial detail.

Multi-compartment models divide the entire reactor into multiple compartments, and each compartment is assumed to be perfectly mixed. The model simplifies the hydrodynamic information of the cells and is much faster

than full CFD simulation while retaining the spatial detail of the CFD solution [173-175]. The flow pattern and velocity profile are solved by CFD using a sufficient number of cells, and the entire domain is divided into multiple compartments. The flow information between cells at the interface of adjacent compartments is merged to obtain the net flowrate between the cells. In addition, the perfect mixing assumption in each compartment allows the reaction to be solved with fewer subdomains. However, a technical issue facing the multi-compartment model concerns the specification of the area of each compartment comprising cells with similar properties, which exerts a strong influence on the process behavior [176, 177]. The multi-compartment model has been applied to the analysis of equipment and regions where hydrodynamics and other important phenomena such as chemical reactions, mass transfer, and shear stress are combined in complex ways. For example, the effects of mixing and shear stress on mass transfer in an aerobic bioreactor and a photobioreactor were by using the multi-compartment model and CFD modeling [178-181]. The hydraulic behavior of a biokinetic process model in a waste stabilization pond system was predicted using the multi-compartment model, and the recirculation patterns in the pond were determined at low computational cost [182]. In addition, the hybrid large eddy simulation (LES) with multiple compartments was applied to simulate uranium oxalate precipitation in a vortex reactor at the industrial scale, and the impact of the vortex on the solid particle properties was predicted [183]. A stirred tank reactor model based on multiple compartments was used to make predictions of the turbulent energy dissipation rate and mass transfer coefficient, and the results showed good agreement with experimental data [184, 185]. In addition, the multi-compartment model using hydrodynamic

information from a CFD model has been used to model other equipment, such as a high shear granulator, and processes, such as fluid catalytic cracking (FCC) and crystallization [186-188].

In this study, the polymerization process in a high-pressure EVA autoclave reactor was numerically simulated by combining the moment equation for polymerization reaction kinetics with the computationally derived hydrodynamic characteristics of the reactor. By using CFD, the local flowrate and micromixing of the fluid, as well as the global continuity of the fluid and macromixing effects, were obtained and divided using a user-specified standard into the multi-compartment model. The inherent flow information for the cells in each compartment was merged and converted to numerical quantities and combined with the terpolymerization kinetic model. The kinetic model based on hydrodynamics can predict the critical properties of a product such as a number-averaged molecular weight ($\overline{M}_n$), the weight-averaged molecular weight ($\overline{M}_w$), and percentage by weight of vinyl acetate (VA, wt%) with the conversion and local temperature of the reactor. The proposed model was used for property prediction and the results are compared with a dataset obtained from the real industrial-scale process.

5.2 Method

5.2.1 EVA autoclave reactor

A multi-zone reactor is typically a vertical cylindrical vessel with 10 to 20 length/diameter (L/D) ratio [167], and the conversion ranges from 10% to 30% [189]. The EVA autoclave reactor in the present study is composed of three

zones separated by disks, and the polymerization reactions and mixing by a stirrer occur simultaneously in each zone. Fig. 37 shows a schematic of the autoclave reactor considered in the present study. The feed, mainly ethylene and vinyl acetate monomer (VAM), is split into several branches and fed into the inlet and each zone of the reactor to control the temperature distribution in the autoclave reactor. Both an excess amount of initiator and inadequate mixing can cause hot spots in the reactor caused by high local reaction rates, leading to thermal runaway and the decomposition of ethylene [190].

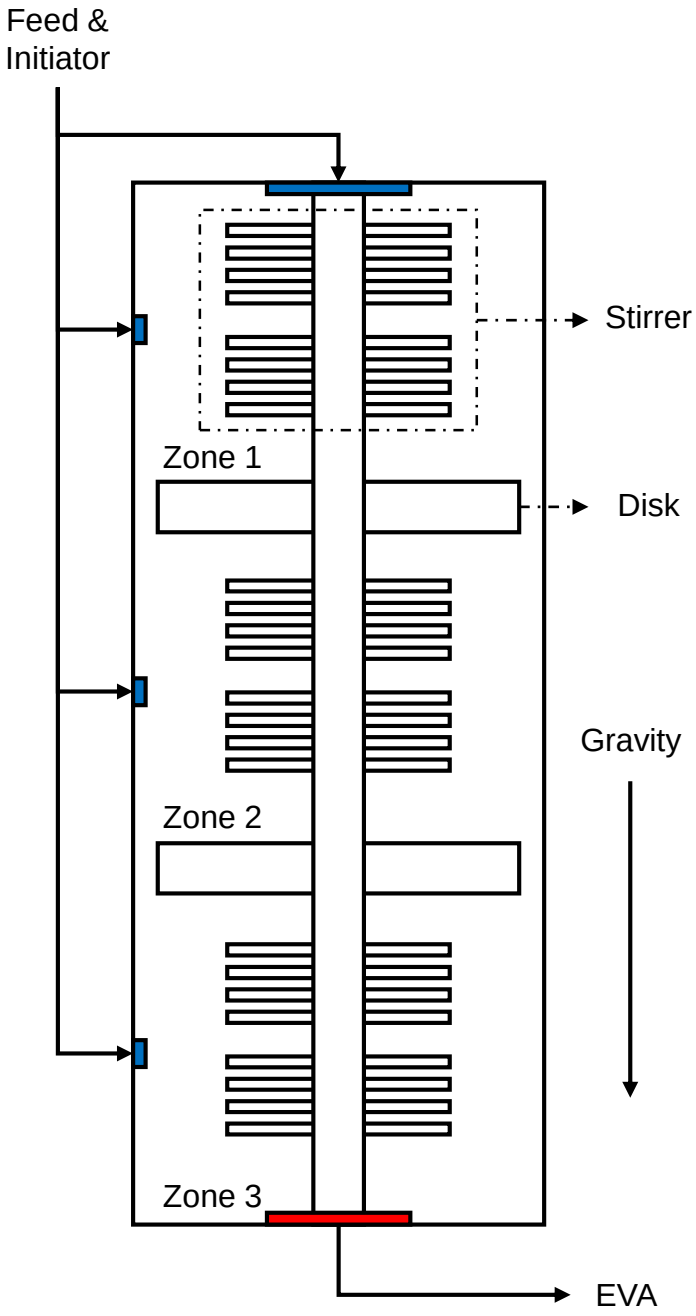

Figure 37. Schematic of the autoclave reactor.

5.2.2 Multi-compartment model of the autoclave reactor

Fig. 38 shows the schema of the multi-compartment model built in this study, which was simulated in a sequential manner. First, the hydrodynamic phenomena were calculated using CFD, yielding the mass flowrate and direction in the fluid domain. The cells generated by a meshing tool each contain flow information and volume. To generate compartments that model a continuous stirred-tank reactor (CSTR), cells having almost equal flow velocities were assembled and divided from the other groups. A separating algorithm, denoted the "region-based dividing algorithm" in this study, was used to calculate the mass flowrates at the interface between the compartments. The information about the mass flowrate between adjacent compartments, which have been constructed to contain the condensed hydrodynamics of the fluid in the autoclave reactor, is combined with a polymerization kinetic model developed using the moment method. Finally, the mass, momentum, and energy balance equations are simultaneously solved for the multi-compartment system, and the calculated results are compared to the data from an industrial EVA autoclave reactor.

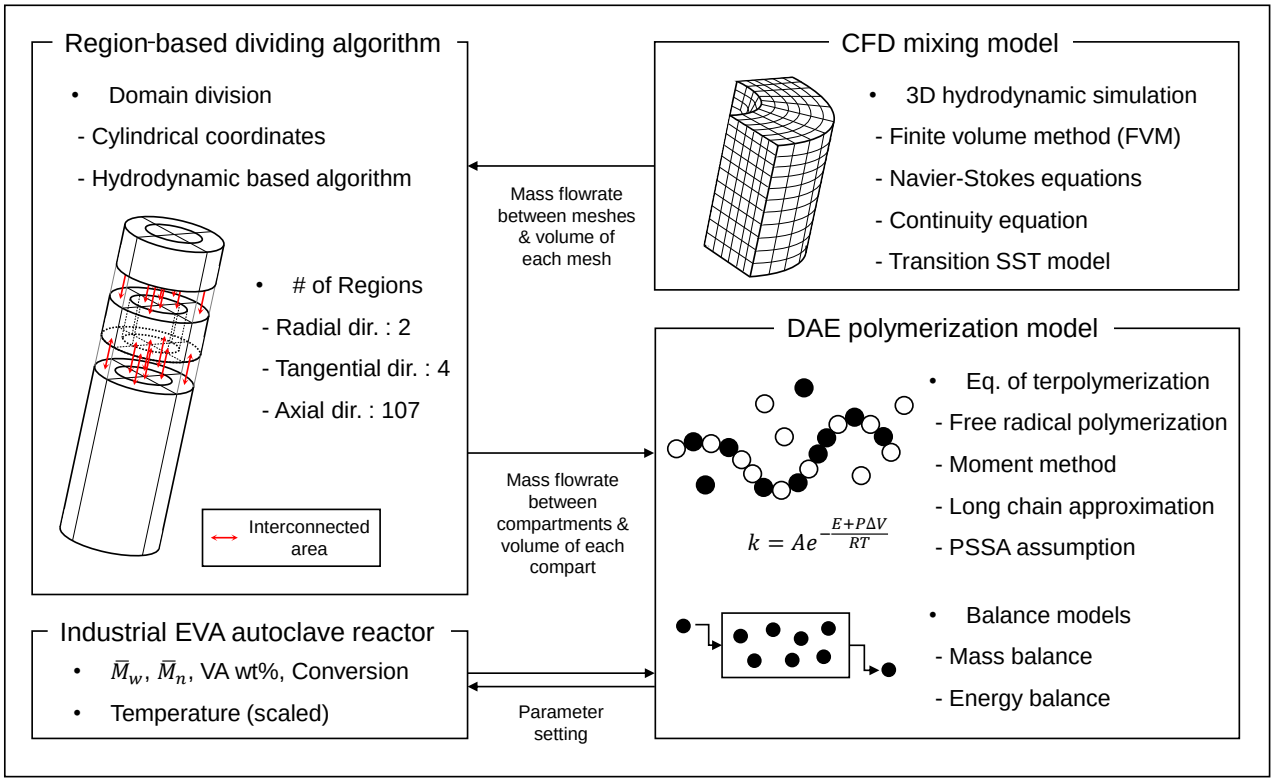

Figure 38. Schematic representation of the multi-compartment model combined with CFD mixing model and kinetic of polymerization.

5.2.3 CFD simulation of mixing effects in the autoclave reactor

A CFD model of the industrial autoclave reactor was used to determine the hydrodynamic phenomena induced by the stirrers. Structural details are not provided in this paper because it is proprietary information. In the numerical CFD simulation, all the unsteady fluctuations of the turbulent model were averaged out, and the multiple reference frame (MRF) model was used to handle the moving geometry, i.e., the stirrer. The transitional shear stress transport (SST) turbulence model, which is based on the SST k-ω transport equation coupled with two other transport equations, was used for the simulation.

For the intermittency (γ),

$$\frac{\partial(\rho\gamma)}{\partial t}+\frac{\partial\left(\rho U_j\gamma\right)}{\partial x_j} = P_{\gamma1}-E_{\gamma1}+P_{\gamma2}-E_{\gamma2}+\frac{\partial}{\partial x_j}\left[\left(\mu+\frac{\mu_t}{\sigma_\gamma}\right)\frac{\partial\gamma}{\partial x_j}\right] \tag{5-1}$$

For the transition momentum thickness Reynolds number ($Re_{\theta t}$) [191, 192],

$$\frac{\partial\left(\rho\widetilde{Re}_{\theta t}\right)}{\partial t}+\frac{\partial\left(\rho U_j\widetilde{Re}_{\theta t}\right)}{\partial x_j}=P_{\theta t}+\frac{\partial}{\partial x_j}\left[\sigma_{\theta t}(\mu+\mu_t)\frac{\partial\widetilde{Re}_{\theta t}}{\partial x_j}\right] \tag{5-2}$$

In the above equations, $P_{\gamma1}$ and $E_{\gamma1}$ are the laminar-turbulent transition source terms, respectively, $P_{\gamma2}$ and $E_{\gamma2}$ are the destruction and relaminarization source terms, respectively, and $P_{\theta t}$ is a source term designed to force the $\widetilde{Re}_{\theta t}$ to match the local value of $Re_{\theta t}$ derived from an empirical correlation. The local transition is triggered by the transport equation for the intermittency (Eq. 5-1), whereas the nonlocal influence of the turbulence

intensity is captured by the equation for the transition Reynolds number. ANSYS 18.2 with Fluent 18.2 was used to solve all CFD equations, and the simulations were performed on an Intel Xeon E5-2667 CPU 3.20 GHz processor.

The viscosity and density of the fluid, which are contained in the continuity momentum equation, were assumed to be constant (7.2 mPa s and 520 kg/m^3, respectively [193]) because the changes are sufficiently small because of low monomer conversion [194-196]. The inlet velocities of multi-feed streams and pressure outlet were considered as the boundary conditions of the model.

The CFD results are shown in Fig. 39. Because the distribution of turbulence kinetic energy is defined as the variance of the velocity fluctuations, the contours in the cross section in Fig. 39 (a) shows the macromixing near the stirrer. The effect of macromixing is the largest in the rotating regions where the impellers are located. The velocity of the fluid at the cross section perpendicular to the product outlet is shown in Fig. 39 (b). Despite the small space between the end of the impeller and the wall, the velocity near the wall is nearly zero because of the no-slip boundary condition. The high rotational speed of the stirrer makes the velocity of the fluid uniform through regions at equivalent distances from the stirrer.

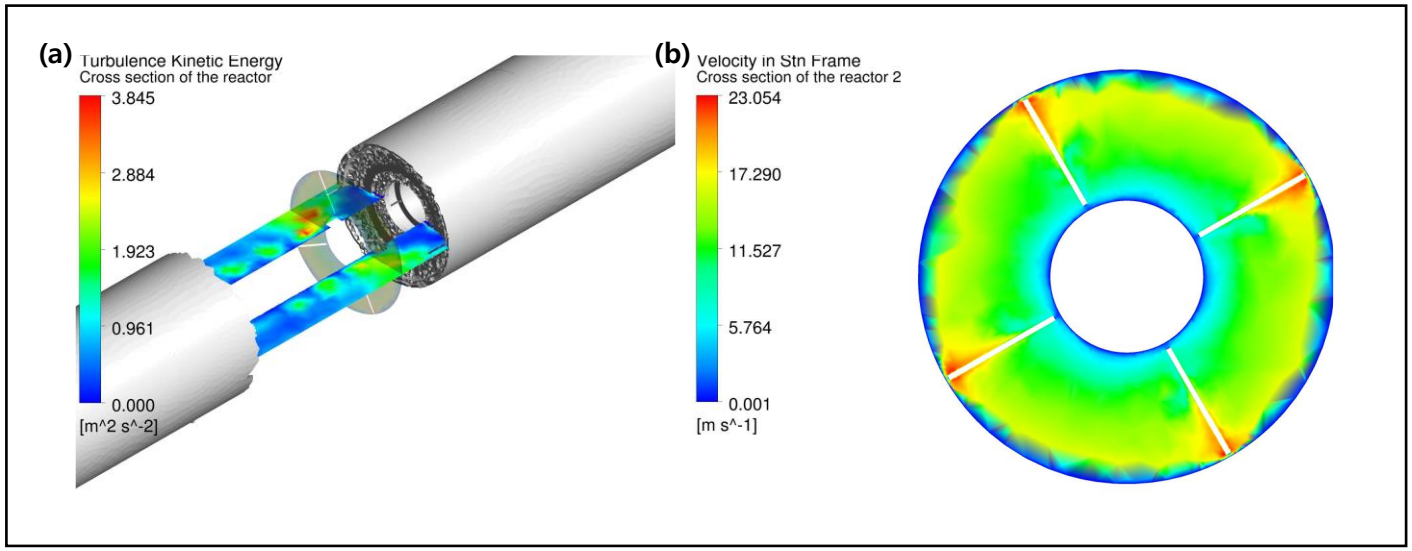

Figure 39. Distributions of (a) turbulence kinetic energy and (b) velocity in cross sections of the autoclave reactor.

The CFD results shown above are used to build the multi-compartment model. The autoclave is divided based on the velocity field in the reactor, and the flowrate among compartments are defined. The detail about the algorithm for dividing domain and agglomerating the cells is described in section 5.2.4.

5.2.4 Region-based dividing algorithm

There are two methods for dividing the cells in the fluid domain into multiple compartments. First, the compartment can be automatically defined by agglomerating cells with similar properties, such as velocity, pressure, and temperature, within a specific tolerance to form one compartment. The other method, the so-called "manual method," defines a compartment based on the intuition and decision of a user who has prior knowledge of the hydrodynamic characteristics in the reactor. Factors such as the structure of the target equipment, computer power, grid structure, and simulation data are considered to designate a compartment region [176, 178]. There are a few limitations of applying the automatic dividing method to the autoclave reactor. The complex hydrodynamics of the fluid inside the reactor cause large and small compartments to be created because the velocity of the fluid varies widely by location. Under such circumstances, cells far away from each other can be included in the same compartment and assumed to be perfectly mixed. The imbalance in the sizes and shapes of the compartment extends computation time and impedes the convergence of the combined model. Another limitation is that the calculation of the flow direction is challenging under the imbalance, considering that the flow direction in the 3D model should be more intuitive than the 2D model for defining the mass flowrate of fluid at the interfaces and integrating the properties of cells in the same compartment. For these reasons,

the "manual method" was used instead of the dividing compartment method based on the fluid property parameters.

5.2.4.1 Compartment range setting

First, the compartment range must be set before the aggregation of cell information because the rotating impellers result in rotating turbulent flow around an axis under a cylindrical coordinate system. The three coordinates (r, θ, z) represent the rotating flow easily and prevent the loss of flow information. The computational domain in the radial direction was divided into two halves in this study. The region where the r coordinate is smaller than $\frac{R-R_{min}}{2}$ is denoted the *inner part* of the reactor and the other region is denoted the *outer part* of the reactor. The symbol R represents the radius of the reactor, and R_{min} is the minimum value of the r coordinate in the computational domain. In the inner part, the fluid flows backward by collision with the disks, which are located between zones, but the backflow of the fluid is very small in the outer part. Although the fluid flow tends to have a similar velocity in the tangential direction, the region is divided into four equal-size subregions in the tangential direction to consider the effects of side feed streams on the tangential velocity; this choice reflects a compromise between the accuracy of the multi-compartment model and computational load. In the axial direction, the domain is divided depending on the velocity distribution of the fluid obtained from CFD simulation, which is affected by the impeller and inlet locations, resulting in 107 subregions and 106 interfaces between subregions in the axial direction. The total number of subregions is 856 (four

subregions in the theta direction) after division based on the three coordinates in the cylindrical coordinate system.

5.2.4.2 Cell aggregation

In CFD simulation, the geometry is discretely represented by the cells, in which the partial differential equations, including Navier–Stokes equations and continuity equation, are approximated. The set of the cells created by the mesh generation method in CFD is defined as $\mathbf{C}$. The cells that belong to the same n^{th} subregions are assigned to the subset $\mathbf{C}_n$, as follows:

$$\mathbf{C}_n = \{c_n(r,\theta,z) \in \Re:\ r_{n,min} < r < r_{n,max},\ \theta_{n,min} < \theta < \theta_{n,max}, z_{n,min} < z < z_{n,max}\} \quad (5\text{-}3)$$

where each c_n denotes the cell belonging to the subregion, and its cylindrical coordinates are represented by the center-coordinates: r_n, θ_n, and z_n. Every cell in the domain must belong to at least one subset $\mathbf{C}_n$, and no cell is included in the intersection of either of the two subsets $\mathbf{C}_n$ or $\mathbf{C}_n{}'$, which can be mathematically expressed as follows:

$$\mathbf{C_n} \cap \mathbf{C_{n'}} = \emptyset \qquad \forall n, n' \in N. \quad (5\text{-}4)$$

The union of all subsets $\mathbf{C}_n$ is defined as follows:

$$\mathbf{C} = \bigcup_{n\in N} \mathbf{C}_n. \quad (5\text{-}5)$$

Additionally, the volume of each compartment, V_n, is the sum of the volume of cells in subset $\mathbf{C}_n$:

$$V_n = \sum_{c\in \mathbf{C}_n} v_c. \quad (5\text{-}6)$$

5.2.4.3 Interface aggregation

The interfaces between the subsets should be defined to calculate mass flowrate in the interconnected compartment system. If the face of cell c is called f_c, the whole face of the cells in subset $\mathbf{C}_n$ becomes

$$\mathbf{F}_n = \bigcup_{c \in \mathbf{C}_n} f_c. \tag{5-7}$$

In the collection of the face sets, an interface set $\mathbf{I}_{nn'}$ of the two subsets $\mathbf{C}_n$, and $\mathbf{C}_{n'}$ is expressed by

$$\mathbf{I}_{nn'} = \mathbf{F}_n \cap \mathbf{F}_{n'}. \tag{5-8}$$

In addition, the net mass flowrate at interface set $\mathbf{I}_{nn'}$ is the sum of the differential values of a fluid mass at cells that belong to the interface set, defined as

$$\dot{m}_{nn'} = \sum_{i \in \mathbf{I}_{nn'}} \dot{m}_i \qquad \forall\ n, n' \in N \tag{5-9}$$

where the sign (positive or negative) of $\dot{m}_{nn'}$ indicates the direction of the fluid flow. Because the polymerization process in this study is operated at the steady state, the sum of the mass flowrate in any zone n^* must satisfy the following equation without consideration of the flow of inlet and outlet:

$$\sum_{n \in N} \dot{m}_{n^* n} = 0 \qquad \forall n^* \in N, n \neq n^* \tag{5-10}$$

Here, $\dot{m}_{nn'}$ is an element of the $N \times N$ matrix $\dot{\mathbf{M}}$, and V_n is an element of the $N \times 1$ matrix $\mathbf{V}$. Both matrices are fundamental when building a multi-compartment system in which the properties of the fluid in each compartment dynamically change over time. Because quantitative information on the hydrodynamics of the EVA reactor is inherent in the generated matrices, a

combination of the mixing effect of the impellers and the EVA polymerization reaction becomes possible.

5.2.5 Polymerization kinetic model

Several general kinetic models have been developed for free-radical polymerization [164]. The EVA polymerization follows a free-radical polymerization mechanism for which the elementary reactions have already been proposed [166, 167, 197]. The mechanism includes the decomposition of the initiator, propagation, termination by combination and disproportionation, chain transfer to the monomer and polymer, and β-scission of the radicals. Table 1 shows the elementary reactions of the polymerization where *I*, *R*, *M*, and *P* represent initiator, live radical, monomer, and dead polymer, respectively; *x* and *y* are the number of monomer units in the radical or polymer; and subscripts *i* and *j* indicate the number of chain branch.

Table 12. Kinetic mechanism for EVA polymerization.

reactions	mechanisms
initiation	$I \xrightarrow{k_d} 2R_1(0)$
propagation	$R_i(x) + M \xrightarrow{k_p} R_i(x+1)$
termination by combination	$R_i(x) + R_j(y) \xrightarrow{k_{tc}} P_{i+j-1}(x+y)$
termination by disproportionation	$R_i(x) + R_j(y) \xrightarrow{k_{td}} P_i(x) + P_j(y)$
chain transfer to monomer	$R_i(x) + M \xrightarrow{k_{cm}} P_i(x) + R_1(1)$
chain transfer to polymer	$R_i(x) + P_j(y) \xrightarrow{k_{cp}} P_i(x) + R_{j+1}(y)$
β-scission of radicals	$R_i(x) \xrightarrow{k_\beta} P_i(x-1) + R_1(1)$

The mechanism of the β-scission of radicals includes the reactions at the terminal radical that form a dead polymer with double bonds at the end of chain and a primary free radical that strongly influences the molecular weight of polymer [166, 198]. In this study, propylene was used as a chain transfer agent (CTA), and it is also copolymerized into the chain; thus, the EVA copolymerization system extends to terpolymerization [199, 200].

To simplify the mathematical equations, pseudo-kinetic rate constants were used. The rate constant of each elementary reaction was calculated as weighted sums based on the fraction of radical or monomer, as shown in Table 13.

Table 13. Pseudo-kinetic rate constants of each elementary reaction.

reactions	equations
propagation	$K_p = \sum_{i=1}^{3}\sum_{j=1}^{3} k_{pij}\varphi_i f_j$
termination by combination	$K_{tc} = \sum_{i=1}^{3}\sum_{j=1}^{3} k_{tcij}\varphi_i\varphi_j$
termination by disproportionation	$K_{td} = \sum_{i=1}^{3}\sum_{j=1}^{3} k_{tdij}\varphi_i\varphi_j$
chain transfer to monomer	$K_{cm} = \sum_{i=1}^{3}\sum_{j=1}^{3} k_{cmij}\varphi_i f_j$
chain transfer to polymer	$K_{cp} = \sum_{i=1}^{3}\sum_{j=1}^{3} k_{cpij}\varphi_i F_j$
β-scission of radicals	$K_{beta} = \sum_{i=1}^{3} k_{betai}\varphi_i$

k: see Appendix 5.5, φ_i: mole fraction of type i polymer radical, f_i: mole fraction of monomer i in monomers, and F_i: mole fraction of monomer i in the polymer

In the pseudo-kinetic rate constants, the parameters f_i and F_i used for the rate constant calculations are expressed as

$$f_i = \frac{M_i}{M_1 + M_2 + M_3} \tag{5-11}$$

$$F_i = \frac{\psi_i}{\psi_1 + \psi_2 + \psi_3}, \tag{5-12}$$

where M_i and ψ_i are the molar concentration of monomer *i* in the bulk phase and in the polymer phase, respectively. f_i evaluates the influence of the mole fraction of monomer *i* on the type of polymer radical, whereas F_i dominantly determines the percentage of monomer *i* in the total weight of product polymer.

The mole fraction (φ_i) of type *i* polymer radical, in which monomer *i* adheres to the end of polymer chain, is obtained using the long chain approximation, as follows [201-203]:

$$k_{pij}\varphi_i f_j + k_{pik}\varphi_i f_k = k_{pji}\varphi_j f_i + k_{pki}\varphi_k f_i, \tag{5-13}$$

where φ is defined as follows:

$$\varphi_1 = \frac{\theta_1}{\theta_1 + \theta_2 + \theta_3} \tag{5-14}$$

$$\varphi_2 = \frac{\theta_2}{\theta_1 + \theta_2 + \theta_3} \tag{5-15}$$

$$\varphi_3 = 1 - \varphi_1 - \varphi_2 \tag{5-16}$$

where

$$\theta_1 = k_{p21}k_{p31}f_1^2 + k_{p21}k_{p32}f_1f_2 + k_{p23}k_{p31}f_1f_3 \tag{5-17}$$

$$\theta_2 = k_{p12}k_{p31}f_1f_2 + k_{p12}k_{p32}f_2^2 + k_{p13}k_{p32}f_2f_3 \tag{5-18}$$

$$\theta_3 = k_{p12}k_{p23}f_2f_3 + k_{p13}k_{p21}f_1f_3 + k_{p13}k_{p23}f_3^2. \tag{5-19}$$

From the kinetic mechanisms of EVA polymerization listed in Table 12 and the pseudo-kinetic rate constants listed in Table 13, the production rates of the radical and polymer can be obtained. However, because there are many species of polymers and radicals depending on the combination of monomers and branches, the moment method is essential to simplify the reaction rate equations. The moment of the live polymers or radicals is

$$\lambda_{m,n} = \sum_{i=1}^{\infty} i^m \sum_{x=1}^{\infty} x^n R_i(x), \tag{5-20}$$

and the equation for the dead polymer is

$$\mu_{m,n} = \sum_{i=1}^{\infty} i^m \sum_{x=1}^{\infty} x^n P_i(x), \tag{5-21}$$

where subscripts *m* and *n* indicate branch distribution and length distribution, respectively. The moments of the radicals and dead polymers can be expressed by applying the moment equation. Because the concentration and decomposition rate of the initiator are negligible compared to those of the other monomers and dead polymer and because each zone acts like the CSTR in the stationary state, the quasi-steady-state approximation (QSSA) can be applied to the 0^{th}, 1^{st}, and 2^{nd} moments of the radicals and the reaction rates for the 0^{th}, 1^{st}, 2^{nd}, and 3^{rd} moments of the dead polymers [163, 164, 166], as shown in Table 14:

Table 14. 0th, 1st, and 2nd moment equations of radicals and 0th, 1st, and 2nd moment balance for polymers.

moments	expressions
0th radical	$\lambda_{0,0} = \left(\frac{2fk_d[I]}{K_{tc}+K_{td}}\right)^{0.5}$
1st radical	$\lambda_{\mathbf{0},1} = \frac{K_P[M]\lambda_{0,0} + K_{cm}\lambda_{0,0}[M] + K_{cp}\lambda_{0,0}\mu_{0,2} + K_{beta}\lambda_{0,0}}{K_{tc}\lambda_{0,0} + K_{td}\lambda_{0,0} + K_{cm}[M] + K_{cp}\mu_{0,1} + K_{beta}}$
2nd radical	$\lambda_{0,2} = \frac{K_P[M](\lambda_{0,0} + 2\lambda_{0,1}) + K_{cm}\lambda_{0,0}[M] + K_{cp}\lambda_{0,0}\mu_{0,3} + K_{beta}\lambda_{0,0}}{K_{tc}\lambda_{0,0} + K_{td}\lambda_{0,0} + K_{cm}[M] + K_{cp}\mu_{0,1} + K_{beta}}$
0th dead polymer	$\frac{d\mu_{0,0}}{dt} = \sum\frac{\mu_{0,0}F_{in}}{V} - \sum\frac{\mu_{0,0}F_{out}}{V} + \frac{1}{2}K_{tc}\lambda_{0,0}^2 + K_{td}\lambda_{0,0}^2 + K_{cm}\lambda_{0,0}[M] + K_{beta}\lambda_{0,0}$
1st dead polymer	$\frac{d\mu_{0,1}}{dt} = \sum\frac{\mu_{0,1}F_{in}}{V} - \sum\frac{\mu_{0,1}F_{out}}{V} + \frac{1}{2}K_{tc}\lambda_{0,0}\lambda_{0,1} + K_{td}\lambda_{0,1}\lambda_{0,0} + K_{cm}\lambda_{0,1}[M] - K_{cp}\lambda_{0,0}\mu_{0,2} + K_{cp}\lambda_{0,1}\mu_{0,1} + K_{beta}(\lambda_{0,1} - \lambda_{0,0})$
2nd dead polymer	$\frac{d\mu_{0,2}}{dt} = \sum\frac{\mu_{0,2}F_{in}}{V} - \frac{\sum\mu_{0,2}F_{out}}{V} + \frac{1}{2}K_{tc}(\lambda_{0,0}\lambda_{0,2} + \lambda_{0,1}^2) + K_{td}\lambda_{0,2}\lambda_{0,0} + K_{cm}\lambda_{0,2}[M] - K_{cp}\lambda_{0,0}\mu_{0,3} + K_{cp}\lambda_{0,2}\mu_{0,1} + K_{beta}(\lambda_{0,0} - 2\lambda_{0,1} + \lambda_{0,2})$
3rd dead polymer	$\mu_{0,3} = \left(\frac{\mu_{0,2}}{\mu_{0,1}}\right)^2\sqrt{2\mu_{0,2}\mu_{0,0} - \mu_{0,1}^2}$

The 3rd moment is obtained from the other moments of polymers.

On the basis of the moments in Table 3, the number-averaged molecular weight ($\bar{M}_n$) and the weight-averaged molecular weight ($\bar{M}_w$) are expressed as follows:

$$\bar{M}_n = \frac{\mu_{0,1} + \lambda_{0,1}}{\mu_{0,0} + \lambda_{0,0}} \bar{M}_{mon} \tag{5-22}$$

$$\bar{M}_w = \frac{\mu_{0,2} + \lambda_{0,2}}{\mu_{0,1} + \lambda_{0,1}} \bar{M}_{mon}, \tag{5-23}$$

where $\bar{M}_{mon}$ is the average molecular weight of the three monomers: ethylene, VAM, and propylene.

As the polymerization process proceeds, related to the rate of production of the polymer, the concentrations of the monomer and initiator decrease. The reaction rates of the monomer (M_i), initiator (I), and moles of monomer i in polymer (ψ_i) are given in Table 15.

Table 15. Components reaction rates.

components	expressions
monomer *i*	$r_{M_i} = -\sum_{j=1}^{3} k_{pji}\varphi_j\lambda_{0,0}[M_i]V$
moles of monomer *i* bound in the polymer	$r_{\psi_i} = \sum_{j=1}^{3} k_{pji}\varphi_j\lambda_{0,0}[M_i]V$
initiator	$r_I = -k_d[I]V$

The rate equations of the components are combined with the mass, momentum, and energy balance equations. The mass balance for each monomer i and bound monomer i in the polymer, and energy balance equation are as follows:

$$\frac{dm_{M_i,k}}{dt} = \sum_{a^{in}} m_{a^{in}} F_{M_i,a^{in}} + \sum_{a^{out}} m_{a^{out}} F_{M_i,k} + [M_i] r_{M_i,k}, \quad (5\text{-}24)$$

$$\frac{dm_{\psi_i,k}}{dt} = \sum_{a^{in}} m_{a^{in}} F_{\psi_i,a^{in}} + \sum_{a^{out}} m_{a^{out}} F_{\psi_i,k} + [M_i] r_{\psi_i,k}, \quad (5\text{-}25)$$

$$m_k Cp_k \frac{dT_k}{dt} = \sum_{a^{in}} m_{a^{in}} Cp_{a^{in}} T_{a^{in}} + \sum_{a^{out}} m_{a^{out}} Cp_k T_k + \sum_i \Delta H_i [M_i] r_{M_i,k}, \quad (5\text{-}26)$$

where subscript a^{in} indicates the mass flowrate of the fluid into the compartment, and a^{out} is the mass flowrate of the fluid from the compartment. With the above equations, the effects of the cold feed streams on the polymerization kinetics such as the decomposition of the initiator and propagation can be properly considered at the expense of computational load because of the dynamical change in the composition and properties of the fluid near the inlet streams.

The dynamic model of the EVA polymerization, which contains the equations in this section can predict the critical factors needed to evaluate the performance of autoclave reactor such as conversion, the weight ratio of monomer in the product, the number-averaged molecular weight ($\bar{M}_n$), and the weight-averaged molecular weight ($\bar{M}_w$).

5.3 Results and discussion

The polymerization kinetic models described in Section 5.2.5 are simultaneously solved with the results of the CFD mixing model using the ordinary differential equation (ODE) solvers implemented in SUNDIALS [204-

[208]. The identities and the kinetic coefficients of the initiators used in the model are given in the Appendix (Table A.1). In addition, the kinetic coefficients of monomers and reactivity ratios between the components are also listed in Table 5.A.2. Among the parameters, the kinetic coefficients and reactivity ratio of propylene were estimated to fit the product specification of the model to those observed in the industrial-scale process. The parameters were iteratively estimated with a popular genetic algorithm for stochastic global optimization. The objective function is composed of the errors in 10 local temperatures of the reactor, the conversion, VA%, $\bar{M}_n$, and $\bar{M}_w$ for two operating points. However, the conversion, VA%, and the locally distributed temperature of the results are already well matched with the actual dataset; thus, the parameters were mainly calibrated to fit $\bar{M}_n$ and $\bar{M}_w$ of the product resin. The results of parameter estimation using the genetic algorithm are consistent with the results of surrogate optimization using radial basis function interpolation for global minimization of the objective function. The same estimated parameters for propylene were applied to two models with different numbers of compartments for two different operating conditions (cases 1 and 2). One model consists of 214 compartments (107 in the axial direction and 2 in the radial direction) and the other has 856 compartments (107 in the axial direction, 2 in the radial direction, and 4 in the tangential direction). A detailed description of the procedure is given in Section 5.2.4.

The influences of the kinetic parameters on the simulation output were analyzed by changing the values of the factors. First, the increase in the initiator decomposition rate decreases the conversion of ethylene and decreases the local temperature of the reactor. The propagation and termination reactions between

molecules also affect the conversion. The vigorous propagation of molecules accelerates the growth of the polymer chain and the termination process changes live polymers into dead polymers. On the other hand, $\bar{M}_n$ and $\bar{M}_w$ are predominantly determined by chain transfer to the monomer, chain transfer to the polymer, and β-scission. Increasing any of these three parameters causes a reduction in $\bar{M}_n$ in the product polymer but the growth of $\bar{M}_w$ is deteriorated by the increase in chain transfer to the monomer and β-scission. Only active chain transfer to the polymer can increase the value of $\bar{M}_w$.

The results of CFD simulation for the two cases were divided into 214 and 856 compartments to condense the hydrodynamic characteristics. Then, the collapsed data for both cases where the mass flowrate at the interfaces and the volumes of regions are included were simultaneously solved for mass and energy balance at each time step. The converged results of the dynamic calculation were verified with data from the industrial-scale autoclave reactor (Table 16). The model is accurate (<7.0% except VA% in case 1 and $\bar{M}_n$ in case 2) in the prediction of the product properties, such as VA%, $\bar{M}_w$, and $\bar{M}_n$, and the performance of the autoclave reactor. The prediction for 856 compartments yielded higher accuracy in $\bar{M}_w$ than that using 214 compartments. Using an identical set of parameters, the average weights of the polymer increase in both cases because of the addition of tangential flow. However, there are no notable changes in the other properties with increase in the number of compartments. Because cases 1 and 2 are operated with different initiators, feed flowrate, and composition of monomer in the feed, these cases have different initiator decomposition kinetics, collapsed flow data, and inlet flowrates for each substance. In case 1, there was considerable error in VA% .

On the other hand, there was substantial error in $\bar{M}_n$ in case 2, but the error became negligible with increase in the number of compartments.

With pre-allocated mass flowrates, all properties (mass of monomer and polymer, temperature, and moments of 214 compartments) achieved a steady state in 5 min, which is a dramatic reduction in time compared to earlier reactor models [169, 170]. The time required for the simulation to converge on a stable solution was six times shorter for the model with 214 compartments than that of the model with 856 compartments. Although the use of a larger number of compartments increases the computational time, it has several advantages.

Table 16. Comparison between the observation of industrial-scale reactor and the prediction of the developed multi-compartment model.

case 1	observation	prediction (214)	error* (214)	prediction (856)	error* (856)
conversion	–	–	1.24	–	0.41
VA%	18	0.1598	11.22	0.1596	11.36
$\bar{M}_w$	141575	131674	6.99	135136	4.55
$\bar{M}_n$	13211	13167	0.33	12738	3.58
temp+ (top)	1.085	1.098	1.15	1.094	0.81
temp+ (middle)	1.084	1.090	0.54	1.077	0.66
temp+ (bottom)	1.126	1.118	0.69	1.088	3.41
case 2	observation	prediction (214)	error* (214)	prediction (856)	error* (856)
conversion	–	–	1.95	–	4.27
VA%	28	28.03	0.11	28.07	0.25
$\bar{M}_w$	99994	93415	6.58	95921	4.07
$\bar{M}_n$	10226	11269	10.19	10244	0.18
temp+ (top)	1.079	1.066	1.17	1.045	3.10
temp+ (middle)	1.123	1.109	1.25	1.110	1.11
temp+ (bottom)	1.254	1.220	2.78	1.218	2.89

*: percentage error, +: scaled representative temperature, and conversion values is not listed

A total of 10 temperature data points were observed from the inlet of the reactor to the outlet where the EVA polymer is obtained. The values of the data point located nearest the inlet do not coincide with the predicted values of the overall compartment model (Fig. 40). The errors between observation and prediction are due to the simplification of the hydrodynamics near the inlet (see Section 5.2.4). The inlet temperature (around room temperature) is used to inhibit the explosive reaction between the initiator and live polymers; thus, the temperature rapidly changes in the region adjacent to the inlet. The temperature change is not smoothly reflected in the multi-compartment model when the mixing effect of the stirrer is summarized into large lumps of cells. For a similar reason, the temperature variability is not minutely predicted in the 20–60 compartment (axial direction). The temperature profiles of all cases were not significantly affected by the number of compartments, except for the gradient of the slope for data from the regions near the inlets. Because the two cases represent operation in the same autoclave reactor, the profiles are very similar. However, the model of case 1 shows better overall predictive performance.

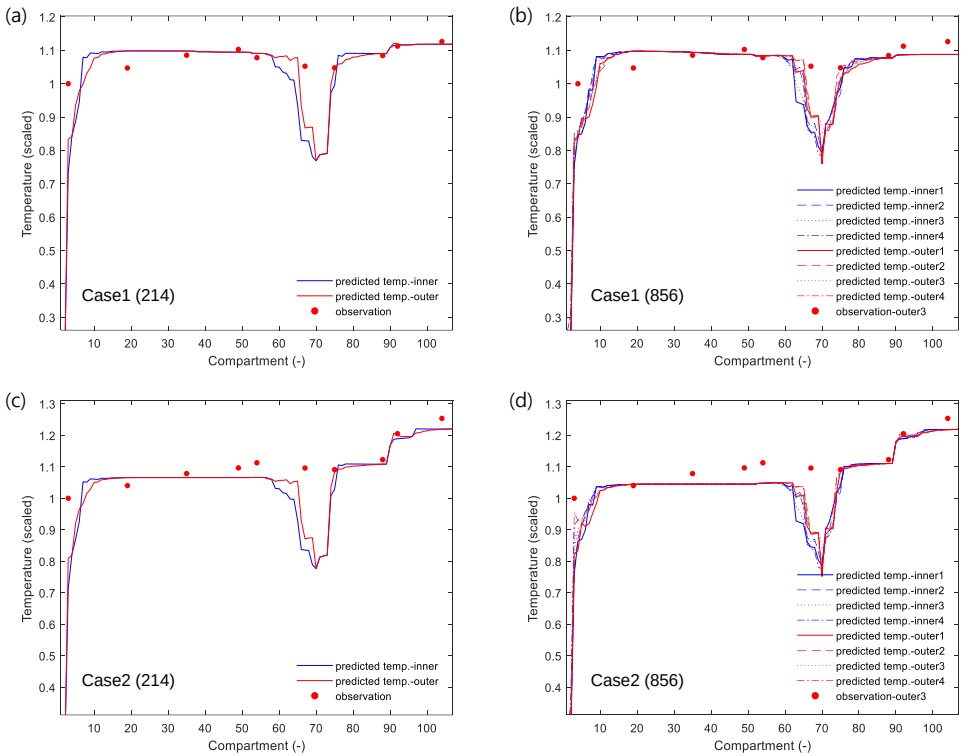

Axial temperature profile of the fluid (mixture of initiator, monomer, and polymer) for a) 214 compartments in case 1, b) 856 compartments in case 1, c) 214 compartments in case 2, and d) 856 compartments in case 2. The observation point is located in the outer part (specifically, it is located in outer 3 in the 856 compartments case) of the reactor (blue line: inner temperature; red line: outer temperature).

Figure 40. Axial temperature profile of the fluid.

The weight ratio of vinyl acetate showed more volatile behavior compared to that of the temperature (Fig. 41). In case 1, the ratio changes slowly, and, in case 2, the magnitude of the change is much bigger. Furthermore, the appearance of the profiles of the two cases is totally different. These differences between the profiles are caused by the differences in the contribution of the reaction rate of vinyl acetate to the overall reaction rate. In case 1, vinyl acetate reacts with radicals faster than propylene, resulting in a high weight ratio distribution around the inlet where the feed and initiator are supplied. In contrast, the propagation of propylene in case 2 is dominant over the other reactions, leading to a low weight ratio of VA around the inlet. However, in the middle of the reactor, unreacted vinyl acetate monomer belongs to the polymer chain. In both cases, the volatility of the ratio is dependent on how much the reaction rate of vinyl acetate differs from the other reactions. Fig. 41 (c) and 41(d) show that the rate of vinyl acetate is considerably lower than those of the other reactions in case 2.

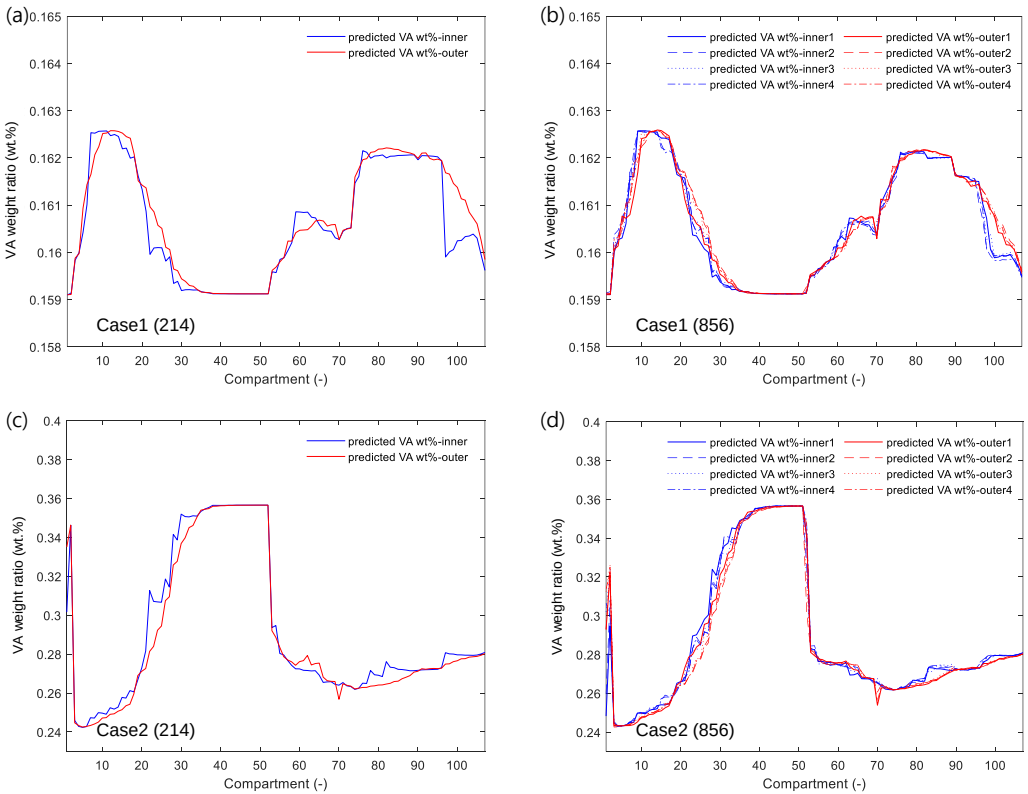

Here, a) and b) are those of case 1 and c) and d) are those of case 2.

Figure 41. VA% of the polymer in cases 1 and 2.

The $\bar{M}_w$ of the dead polymer steadily increases from the inlet to the outlet of the reactor (Fig. 42). The model consisting of 856 compartments showed a faster increase in the value of $\bar{M}_w$ throughout the reactor than that of the 214-compartment model because of the consideration of tangential direction flow. The mixing effect of the stirrer in the tangential direction is only considered in the 856-compartment model, which increases the fluid residence time. In the axial direction, the $\bar{M}_w$ of compartments in the same position are almost the same, but the values are scattered near inlets. This is caused by the broad distribution of the temperature and velocity near the inlets before the stirring effect is still applied. The profile of $\bar{M}_n$ throughout the reactor showed a different trend to that of $\bar{M}_w$ (Fig. 43). The behavior is similar to that of the temperature profile shown in Fig. 4. The temperatures near the inlets are lower than those of other locations and the same trend is also observed in the $\bar{M}_n$ profile, which means the 1st moments of the live and dead polymers are highly affected by the temperature. Unlike the trend in $\bar{M}_w$, the large number of compartments reduces $\bar{M}_n$. However, for both $\bar{M}_w$ and $\bar{M}_n$, the slopes of the profiles became smooth and gentle on increasing the model size to 856 compartments.

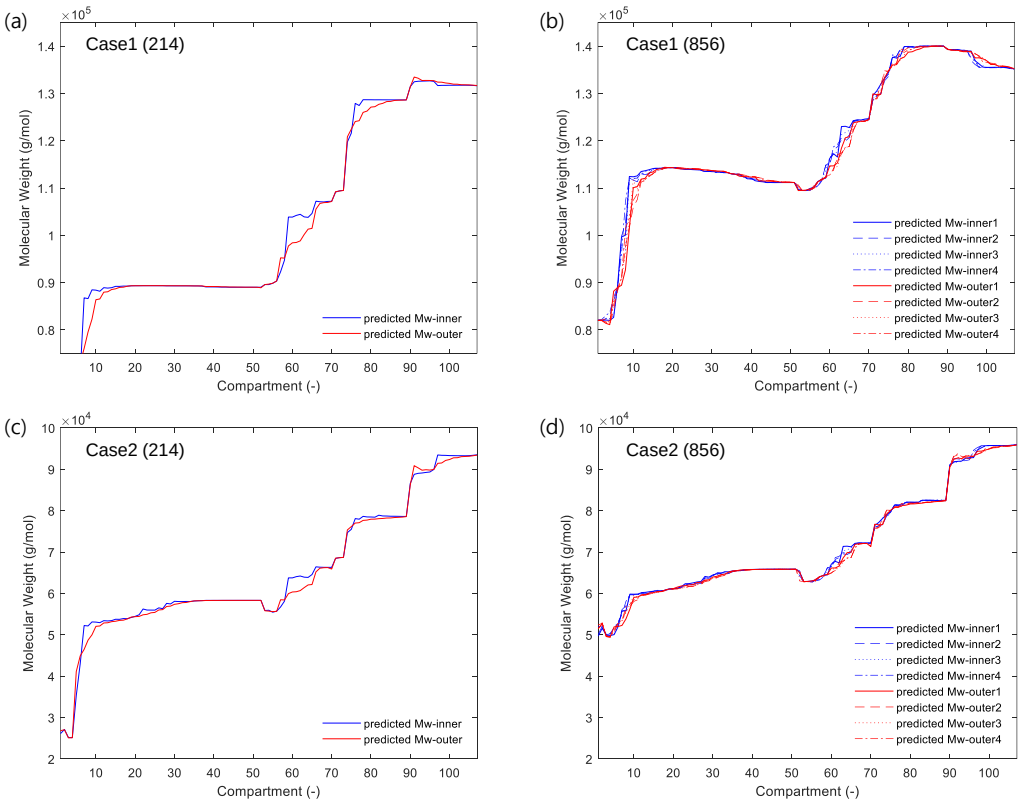

Here, a) and b) are those of case 1 and c) and d) are those of case 2.

Figure 42. Weight-averaged molecular weight of the polymer ($\bar{M}_w$) in the autoclave models.

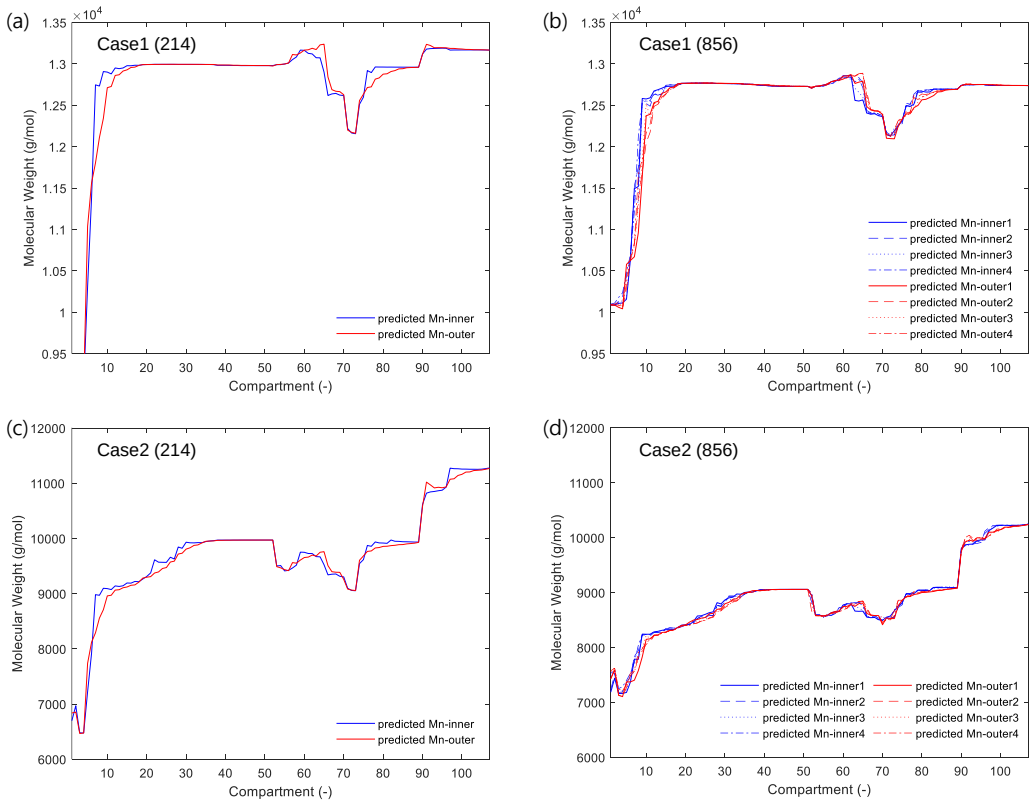

Here, a) and b) are those of case 1 and c) and d) are those of case 2.

Figure 43. Number-averaged molecular weight of the polymer ($\bar{M}_n$) from the autoclave models.

The model presented in this thesis use CFD simulation to calculate turbulent flows in the autoclave reactor. As described in section 5.2.3, the method for transition prediction is based on two transport equations which is fully compatible with modern CFD simulations [209]. Because the average size of coarse grid used in our CFD model is much larger than the smallest scale where turbulent energy is dissipated into heat (i.e. Kolmogorov length scale), the turbulent model should be applied to this simulation, unlike direct numerical simulation (DNS) [210]. In this system, the average Kolmogorov length of this system is estimated to be about 10–100μm and the minimum length of the cell is 4000μm. This reveals that the large number of control volumes are required to calculate turbulence flows without any turbulent model. Furthermore, the average length of compartments presented in this thesis can be estimated to be 0.1m (=100000μm). This implies that the information of the smallest turbulence flows are nearly lost so the presented model is hard to reflect the polymer chain growth occurred on the microscale.

5.4 Conclusion

A multi-compartment model of a high-pressure EVA autoclave reactor has been proposed. In the model, the stirrer-induced mixing effect is numerically simulated using CFD and simplified by grouping and assembling the numerous cell data. The encapsulated hydrodynamics are integrated with the moment equations of polymerization kinetics and simultaneously solved to predict the local temperature and significant properties of the polymer product.

In the study, the CFD model described in Section 5.2.3 was divided into 214 and 856 compartments to evaluate the effect of hydrodynamic simplification and tangential flow. Furthermore, the moment equations were used to model two cases having different numbers of compartments. Both models were compared with data from an actual industrial scale EVA autoclave reactor. Although the rate of convergence of the 856-compartment model is six times slower that of than of the 214-compartment model, the results are more consistent with the experimental data points. The conversion, VA%, $\bar{M}_w$, $\bar{M}_n$, and 10 distributed temperature points were compared with the predicted values for the two cases, and most of the absolute errors were found to be less than 7.0%. The errors are mainly present in the weight ratio of vinyl acetate and the number-averaged molecular weight. There was no significant improvement on increasing the number of compartments, despite the longer computational time, and only the trends in $\bar{M}_w$ and $\bar{M}_n$ were slightly affected.

As reported by others, the multi-compartment model is known to shorten the calculation time required to solve complex problems including interactions between dynamic fluids and chemical or biological reactions [178, 182, 211, 212]. Because of the overwhelming computational load when considering all physical and chemical phenomena, some assumptions are used to facilitate effective prediction within a short period of time; consequently, the method has some limitations; for example, 1) micromixing is disregarded in the reactor to compress and simplify the flow information in the reaction, 2) the short chain branching induced by the backbiting mechanism is not considered because it is hard to simplify using the method of moments, and 3) only the moments of the molecular weight distribution are obtained because of the use of the method of

moments. Nevertheless, our developed multi-compartment model of a polymer reactor using CFD and moment equations enables the margin optimization of the polymerization process and will improve the product quality and operating stability and allow real-time process monitoring.

5.5 Appendix

The identities and kinetic coefficients of the initiators used in the model are shown in Table 17. For two different operating points, two different kinetic coefficients of initiators were used.

Table 5.A.1. Identities and kinetic coefficients of initiators used in the model

Initiator	Symbol	A (L/mol·s)	E/R (K)
TBPEH (case 1)	k_d	1.54×10^{14}	15023
TBPND (case 2)	k_d	1.52×10^{14}	13888

Additionally, the kinetic coefficients of the monomers and the reactivity ratios between each monomer, as well as some simplifying assumptions are used to calculate the pseudo-kinetic constants, are shown in Table 12. The reactivity ratios between each monomer used to derive the propagation constant between different types monomer is

$$r_{ij} = \frac{k_{pii}}{k_{pij}}. \tag{5-28}$$

The parameters related to EVA polymerization are shown in Table 18.

Table 5.A.2. Kinetic constants of ethylene, vinyl acetate monomer, and propylene and reactivity ratios between monomers.

	Elementary reaction	Symbol	A (L/mol·s)	E/R (K)	ΔV (cm3/mol)	Reference
Ethylene	Propagation	k_p	1.25×10^8	3800	-20	[213]
	Termination	$k_{tc} = k_{td}$	1.25×10^9	327	13	[213]
	Transfer to monomer	k_{cm}	8.7×10^5	5032	-20	[213]
	Transfer to polymer	k_{cp}	4.38×10^8	6603	4.4	[213]
	β-scission	k_β	1.292×10^7	5671	-16.8	[214]
Vinyl acetate	Propagation	k_p	1.47×10^7	2490	-10.7	[215]
	Termination	$k_{tc} = k_{td}$	3.7×10^9	1610	-	[194]
	Transfer to monomer	k_{cm}	7.616×10^3	3170	-	[194]
	Transfer to polymer	k_{cp}	1.088×10^4	3170	-	[194]
Propylene	Propagation	k_p	4.31×10^9	3800	-20	-
	Termination	$k_{tc} = k_{td}$	6.03×10^{10}	327	13	-
	Transfer to monomer	k_{cm}	8.7×10^3	1046	-20	-
	Transfer to polymer	k_{cp}	4.38×10^5	330	4.4	-
Reactivity ratios	1: ethylene 2: vinyl acetate 3: propylene	r_{12}		1.090		[216]
		r_{13}		0.239		-
		r_{21}		1.060		[216]
		r_{23}		-		-
		r_{31}		0.820		-
		r_{32}		-		-

In the energy balance of the multi-compartment model, the heat from the free-radical polymerization, which is known to be an exothermic reaction, is

$$\Delta H = \sum_{i=1}^{3} r_{\psi_i} \Delta H_i \tag{15}$$

which is the weighted sum of the heats of polymerization. The heats of polymerization of ethylene, vinyl acetate monomer, and propylene are 22.3, 21.3, and 20.5 kcal/mol, respectively [217, 218].

The heat capacities of ethylene and vinyl acetate monomer are taken from Ghiass *et al.* and the heat capacity of propylene is derived from the property database of Aspen HYSYS V8.4 [167].

Chapter 6

Concluding Remarks

6.1 Summary of contributions

The mathematical model and parameters estimated based on three different systems are presented in this thesis. All models are developed based on first-principle equations including minimum empirical ones. For comparing with relative experimental data, empirically derived or unknown parameters are estimated and calibrated using local and global optimization algorithm. In past, these works could not be solved due to their complexity and enormous computational load. This thesis, however, enabled to address the problems by compiling the main part of the model into C/C++ as well as essentially adopting parallel computing toolbox in programs, both of which improve the speed of calculation. The major contribution of each Chapter is listed below.

- Chapter 3 provides typical procedure of modeling, parameter estimation, and validation about ambient air vaporizer. The developed model is compared with dataset from pilot-scale plant and sensitivity analysis is conducted with prime factors such as velocity, humidity, and temperature. The constructed model is also used to suggest a robust optimal design of the equipment that improves sustainable operation during a year.
- Chapter 4 shows the experiments and model description about a novel continuous segment flow tubular crystallizer. Producing a great number of unprecedented experimental results, first-principle

based mathematical model was validated and evaluated. An explanation of the experiment setting for validation of the model is also explicily described in this chapter. All of the works in this chapter utilize L-asparagine monohydrate and hen egg-white lysozyme, the former of which forms crystals in moderate condition with ease, and the latter of which represents protein in crystallization experiments.

- Chapter 5 treats the methodology that is capable of considering fluid dynamics and chemical reaction together. In this chapter, the major equipment is EVA autoclave reactor, one of classic polymer reactors. Attempting to discover a method using the aforementioned reactor, we employ the computational fluid dynamic program to calculate hydrodynamics induced by stirring parts of the reactors and apply the moment method to simplify complicated kinetic mechanism of polymerization. The results of fluid dynamics are compressed and then extracted by zoning algorithm and combined with reduced kinetic model. The proposed model is demonstrated with dataset from industrial size plants.

6.2 Future work

The works in research fields of this thesis are just being unearthed. On account of numerous research limitations as well as lacking experience and experiments in contrast, it is hardly applied for either educational or industrial purpose. Despite these restrictions, they have a bright prospect. First of all,

there are many opportunities in optimization algorithm and numerical solver for a variety of differential equations. As needs for analyzing and modeling of multi-phase and multi-component system increase, the size of matrices handled in model extends with abundant equations, naturally meeting the increased requirements of high computation efficiency. Inspite of a sufficient number of algorithms and solvers existing in recent days, it is still hard to find the global optimal point with over 5 parameters. In the thesis, the surrogate optimization constructed based on a radial basis function (RBF) and genetic algorithm are used as stochastic methods for detecting global optimal point. Given that the systems treated are highly nonlinear, only DIRECT algorithm of the deterministic methods is recommended to alleviate this problem. Even the methods proposed in this thesis are proved to be suitable for nonlinear optimization, they consume a significant amount of time for computational load. Second, structures of the continuous crystallization process are proposed for the first time along with developed productivity of the continuous process. Unlike the past when crystal growth and design mostly took place in batch process, leading to only few modeling researches on continuous crsytallization process, there are abundant resources books and journals on basic kinetic parameters and reaction mechanisms of crystallization. Modeling works for these crystallizer, therefore, has huge potential to develop and sustainably fulfill its potential. Finally, limitations of existing reactors provide researchers with opoortunities to resolve a problem of the intricate structure of reactors. As of now, there are numerous reactors where multiple elementary reactions and fluid flow dynamics occur concurrently, making strong interaction between them. The strong interaction plays an important role in predicting and modeling the

system, but also disturbs this role at the same time. In order to solve this problem with the development of computational fluid dynamics technique, several solutions are suggested including the multigrid method, the most widely employed problem solution. This method, however, also fails to solve the number of meshes due to the intricate structure of reactor. As to find an appropriate solution to this unsolvable problem, cooperation between physics and chemistry is required. Similar to the multi-compartment model proposed in this thesis, there are great possibilities to interpret the performance of polymerization autoclave reactor.

Appendix

Acknowledgment and collaboration declaration

Chapter 3: Yongkyu Lee devised of all modeling processes and contributed to the original manuscript[1] described in section 3.2, and 3.4.1. Yongkyu Lee and Jonggeol Na made an equal contribution to the manuscript[2] described in section 3.3, and 3.4.2. While Yongkyu Lee performed every mathematical modeling of the ambient air vaporizer, Jonggeol Na executed statistical analysis and optimization of the model. Most contents in this chapter were written by Yongkyu Lee with some exceptions which were completed by Jongmin Lee and Jonggeol Na. The experimental data of the pilot-scale equipment were provided by Taejin corporation.

This research was supported by a grant (14IFIP-B085984-04) from Smart Civil Infrastructure Research Program funded by the Ministry of Land, Infrastructure and Transport (MOLIT) of Korea government, Korea Agency for Infrastructure Technology Advancement (KAIA), the Energy Efficiency & Resources Core Technology Program of the Korea Institute of Energy Technology Evaluation and Planning (KETEP), granted financial resources from the Ministry of Trade, Industry & Energy (MOTIE), Republic of Korea (No. 20162220100030).

Chapter 4: The work presented in this chapter represents a collaboration between the Braatz Lab at MIT and Yongkyu Lee from SNU. Except for some parts written with a collaborative effort of Yongkyu Lee and Nicholas J.

Mzdzier, all sections were conceived and drafted by Yongkyu Lee with guidance from Moo Sun Hong and Richard D. Braatz.

The original CCHEX concept was conceived by Richard D. Braatz, Michael Rasche, and Mo Jiang. The physical CCHEX system was designed and built by Nicholas J. Mozdzierz and Moritz H. P. Benisch. The full-factorial experiments discussed in section 4.2 were conceived, executed, and analyzed solely by Nicholas J. Mozdzierz. The work reflecting his performance was previously described in [3]. In regard to the experiments described in section 4.3, Amos E. Lu provided assistance with cross-polarized transmitted light microscopy. Leia M. Dwyer and Arijit Mukherjee of the Myerson lab at MIT also offered assistance with PXRD measurements. Yongkyu Lee developed image analysis algorithm and acquisition process of crystal size distribution which were previously executed by Nicholas J. Mozdzierz. Remaining works, such as description of mathematical models and analysis were conceived and executed by Yongkyu Lee.

Chapter 5: The works were modeled, analyzed, and verified by Yongkyu Lee, with the aid of Kyeongwoo Jeon, Jiyeong Cho, Jonggeol Na, and Jongmin Park. Yongyu Lee, Kyeongwoo Jeon, Jonggeol Na, and Jongmin Park developed region-based dividing algorithm applied to CFD simulation. Yongkyu Lee and Jiyeong Cho established the kinetic model of polymerization. In all experiments, dataset was given by a corporation whose name cannot be disclosed. With the exception of section 5.2.4, which was written jointly by Yongkyu Lee and Kyeongwoo Jeon, all sections were drafted by Yongkyu Lee.

This work was supported by C1 Gas Refinery Program through the National Research Foundation of Korea(NRF) funded by the Ministry of Science and ICT 2018M3D3A1A01055765.

Supplementary materials

Table S.1. Product crystal size statistics and error for the experiments and the crystallizer model corresponding to the operating conditions in Table 6.

experiment number		1	2	3	4	5	6	7	8	9
Observed data	crystal mean length (μm)	29.2	49.9	52.8	53.2	36.8	41.4	44.1	40.7	43.7
	standard deviation (μm)	26.9	44.3	42.9	45.2	25.9	33.0	44.5	32.8	35.4
	coefficient of variation (%)	92.4	88.9	81.2	84.9	70.4	79.5	100.9	80.6	81.0
	crystal median length (μm)	12.7	31.8	36.5	33.4	22.2	25.3	19.6	25.2	28.4
Predicted data	crystal mean length (μm)	47.8	47.0	47.0	45.6	53.2	52.7	52.2	27.4	25.8
	standard deviation (μm)	39.1	40.1	40.1	38.5	42.6	42.6	37.6	13.5	13.6
	coefficient of variation (%)	80.2	85.4	85.4	84.4	80.2	80.9	72.0	49.3	52.9
	crystal median length (μm)	23.1	20.5	20.5	20.8	23.5	23.0	25.0	13.6	10.7
median error (%)		45.0	55.1	78.0	60.8	5.7	10.0	21.7	85.6	165.7
R squared (–)		0.53	0.94	0.90	0.91	0.91	0.94	0.92	0.44	0.26
experiment number		**10**	**11**	**12**	**13**	**14**	**15**	**16**	**17**	**18**
Observed data	crystal mean length (μm)	50.0	42.8	47.4	43.2	45.6	40.2	38.3	34.8	34.3
	standard deviation (μm)	62.1	30.2	35.5	32.7	35.2	26.7	31.3	27.8	28.3
	coefficient of variation (%)	124.3	70.7	74.9	75.7	77.2	66.3	81.9	79.9	82.6
	crystal median length (μm)	21.9	30.4	31.4	28.6	30.5	29.4	24.4	18.7	17.2
Predicted data	crystal mean length (μm)	50.3	51.0	50.8	47.5	52.0	51.7	53.0	24.7	23.4
	standard deviation (μm)	39.3	39.6	39.6	38.5	39.5	39.5	37.4	10.9	11.0
	coefficient of variation (%)	78.2	77.7	77.9	80.9	75.9	76.4	70.6	44.4	47.4
	crystal median length (μm)	25.7	24.0	23.9	22.5	25.1	24.8	25.8	11.5	9.3
median error (%)		14.8	26.5	31.5	27.4	21.2	18.8	5.8	63.3	85.0
R squared (–)		0.94	0.96	0.96	0.99	0.96	0.93	0.88	0.46	0.33
experiment number		**19**	**20**	**21**	**22**	**23**	**24**	**25**	**26**	**27**
Observed data	crystal mean length (μm)	52.5	38.0	31.9	44.9	29.0	35.0	42.6	39.9	36.2
	standard deviation (μm)	49.8	31.8	28.9	33.8	19.8	25.3	34.0	31.2	29.9
	coefficient of variation (%)	94.9	83.6	90.7	75.2	68.1	72.2	79.7	78.4	79.9
	crystal median length (μm)	29.7	21.3	14.4	30.5	18.1	22.2	26.1	25.3	20.0
Predicted data	crystal mean length (μm)	53.1	44.6	43.1	52.4	44.6	43.1	50.3	36.4	33.8
	standard deviation (μm)	36.4	27.8	28.1	36.5	27.8	28.1	37.8	19.9	20.2
	coefficient of variation (%)	68.5	62.4	65.0	69.7	62.4	65.0	75.2	54.6	59.9
	crystal median length (μm)	30.1	24.3	22.6	29.5	24.2	22.6	23.4	23.4	18.6
median error (%)		1.5	12.3	36.2	3.3	25.4	1.7	11.5	8.0	7.6
R squared (–)		0.98	0.95	0.96	0.98	0.90	0.87	0.99	0.66	0.54

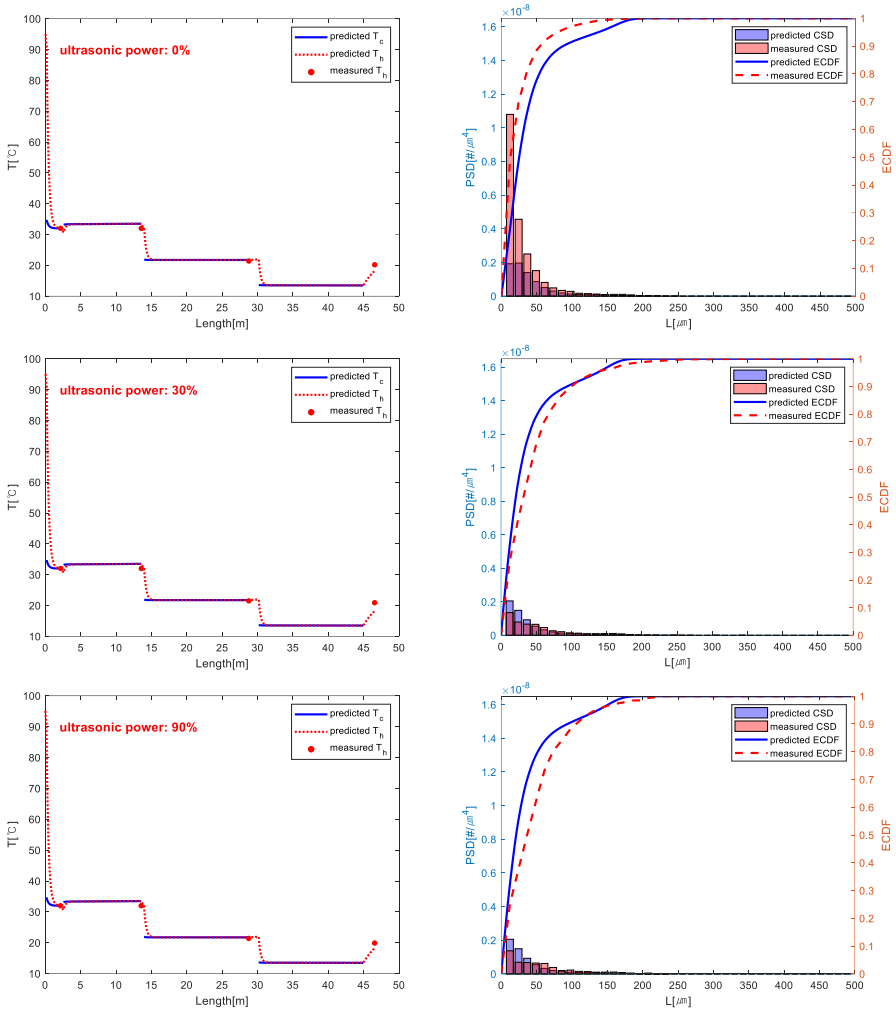

Figure S.1. The figures of experiment #1–3 in Table 6

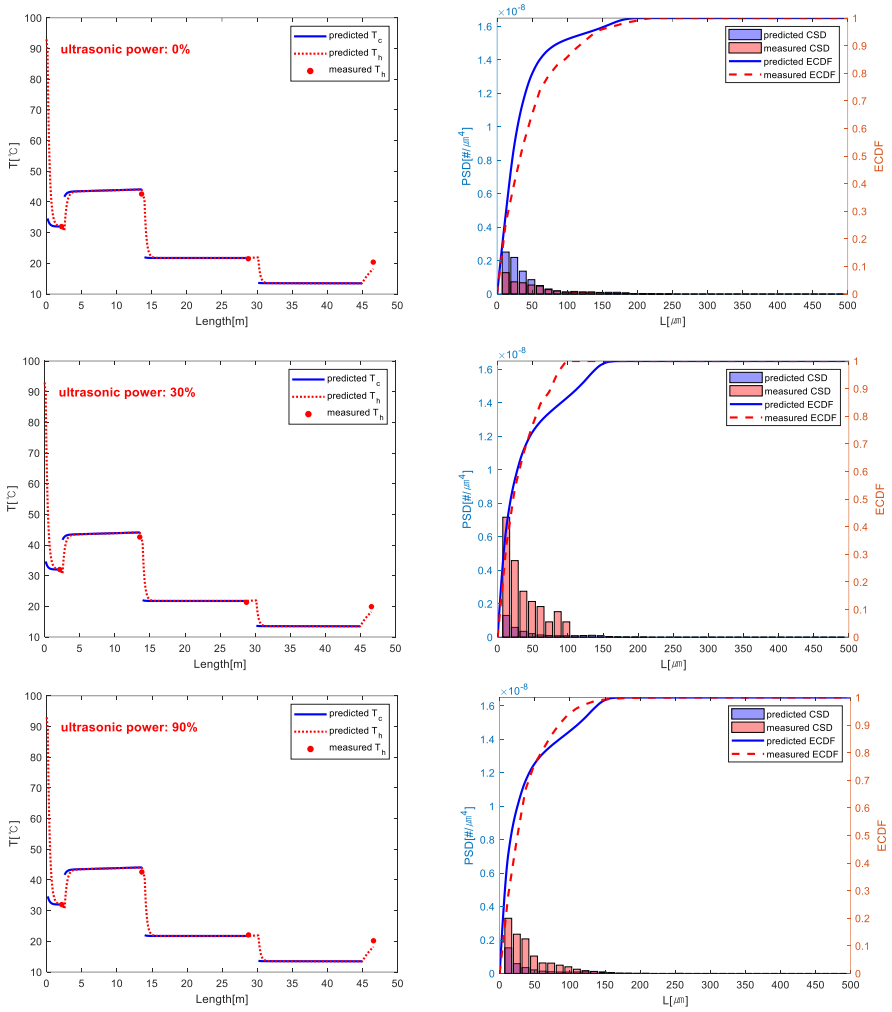

Figure S.2. The figures of experiment #4–6 in Table 6

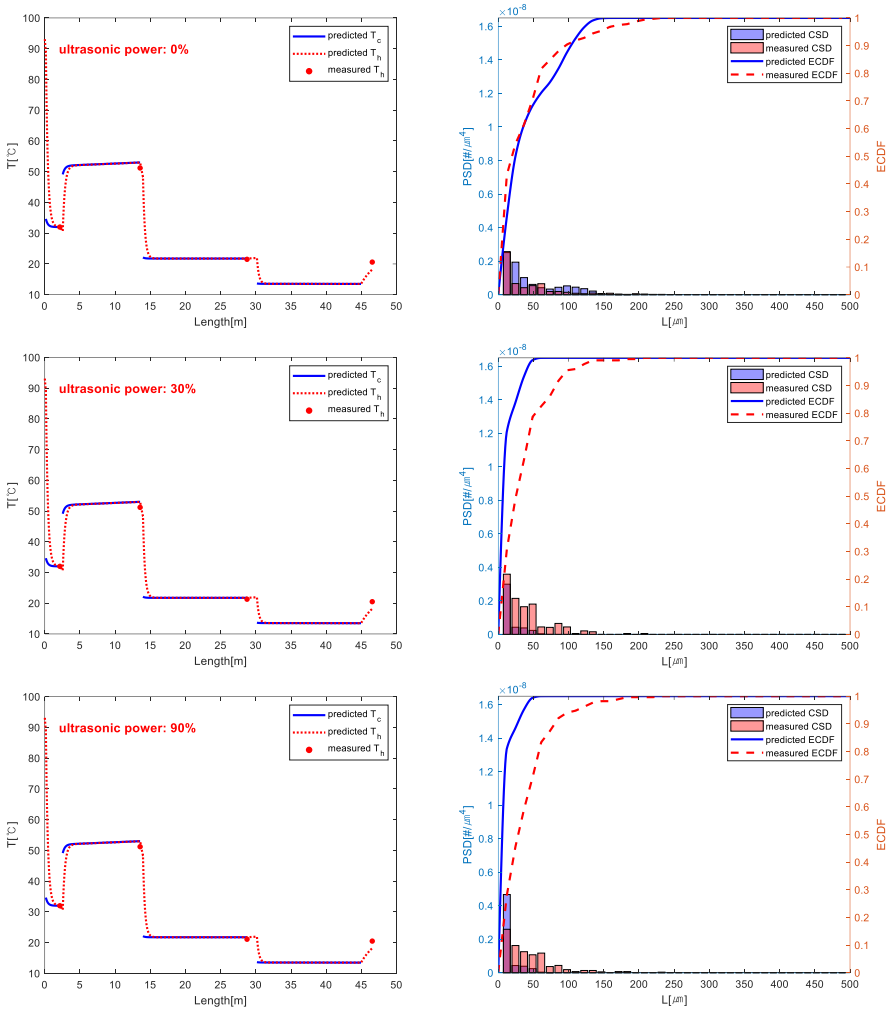

Figure S.3. The figures of experiment #7–9 in Table 6

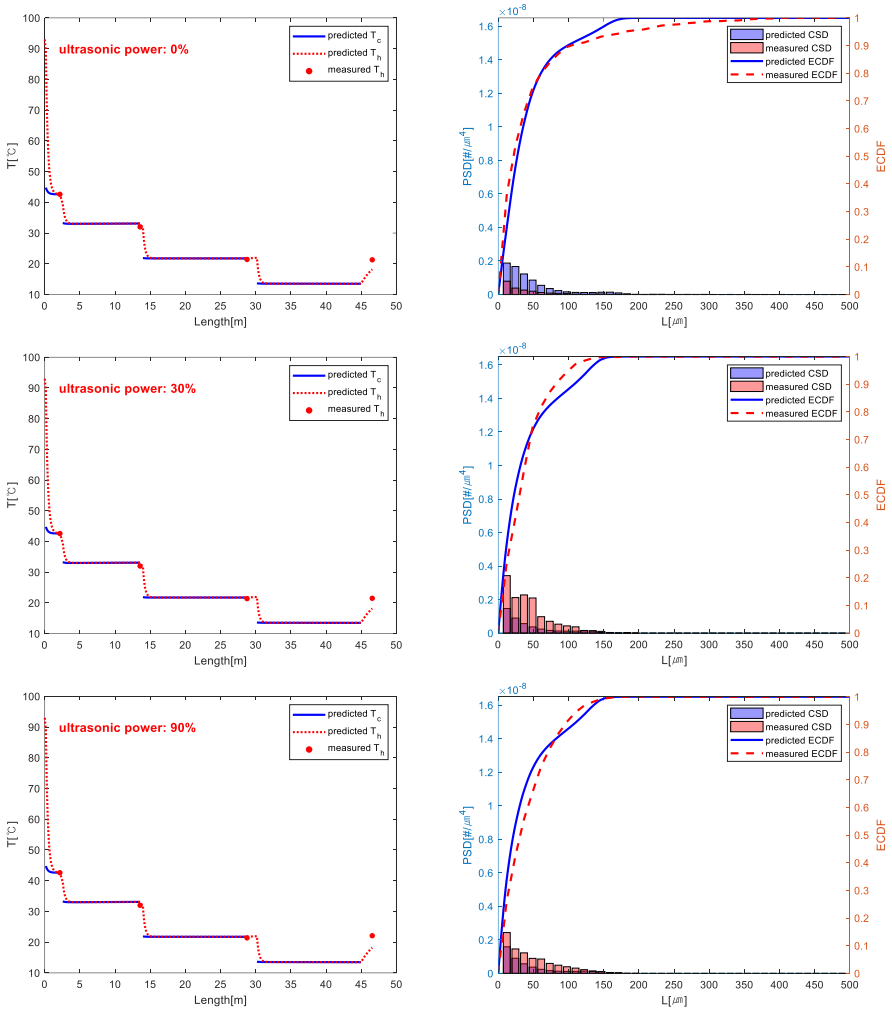

Figure S.4. The figures of experiment #10–12 in Table 6

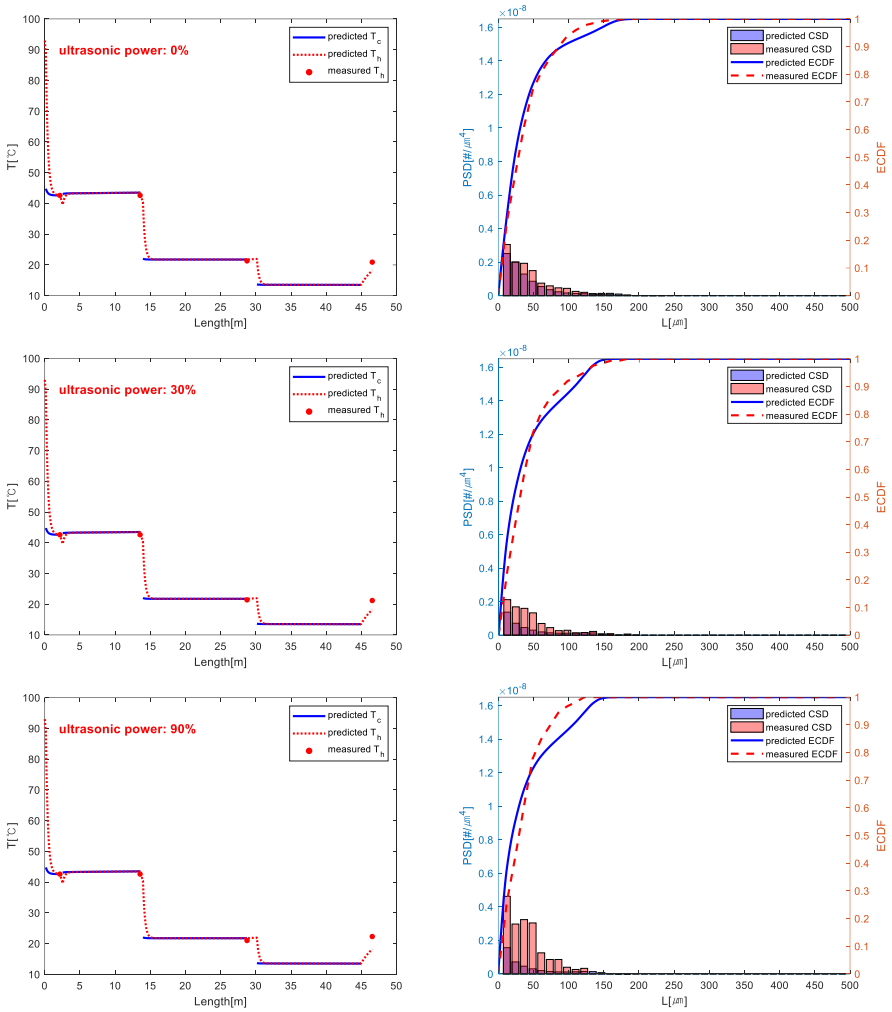

Figure S.5. The figures of experiment #13–15 in Table 6

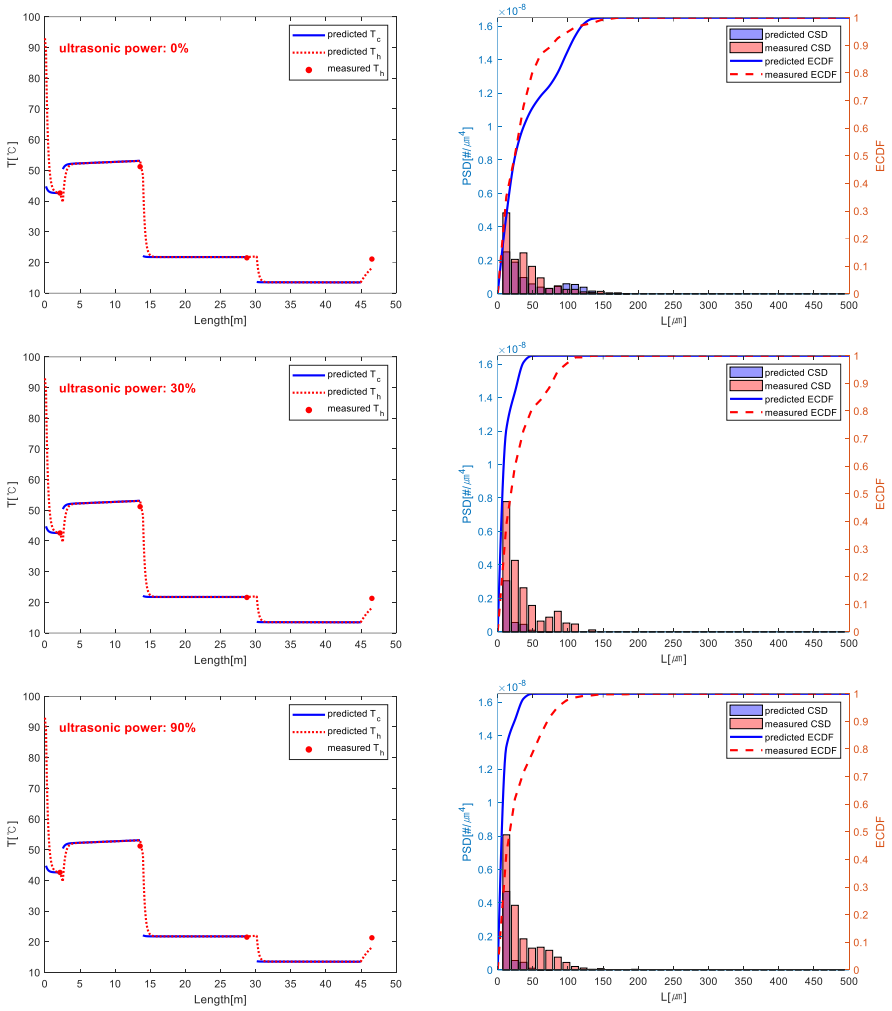

Figure S.644. The figures of experiment #16–18 in Table 6

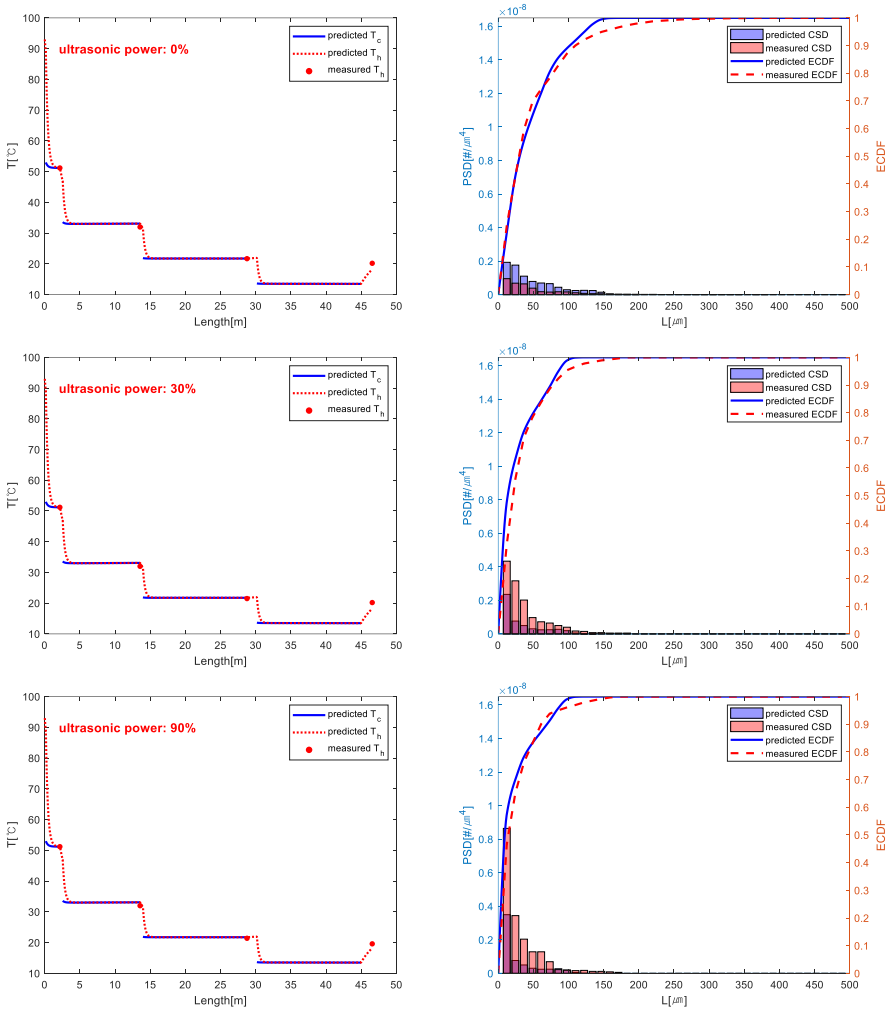

Figure S.745. The figures of experiment #19–21 in Table 6

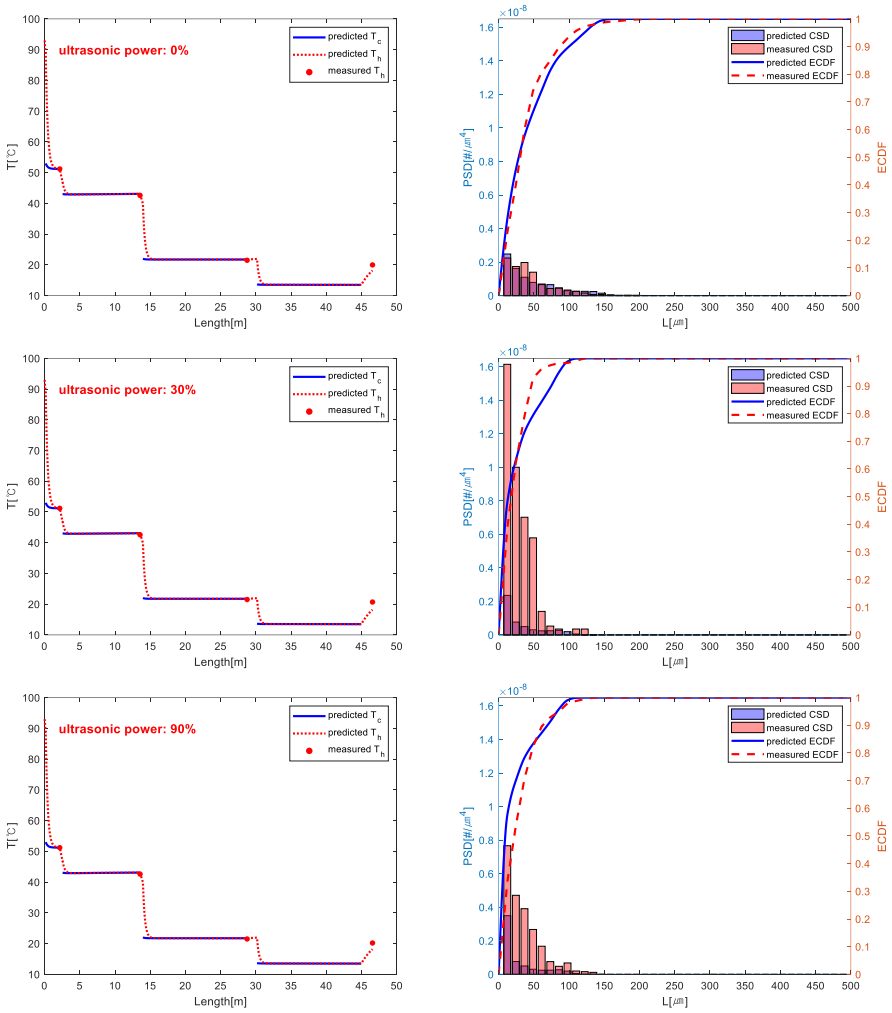

Figure S.8. The figures of experiment #22–24 in Table 6

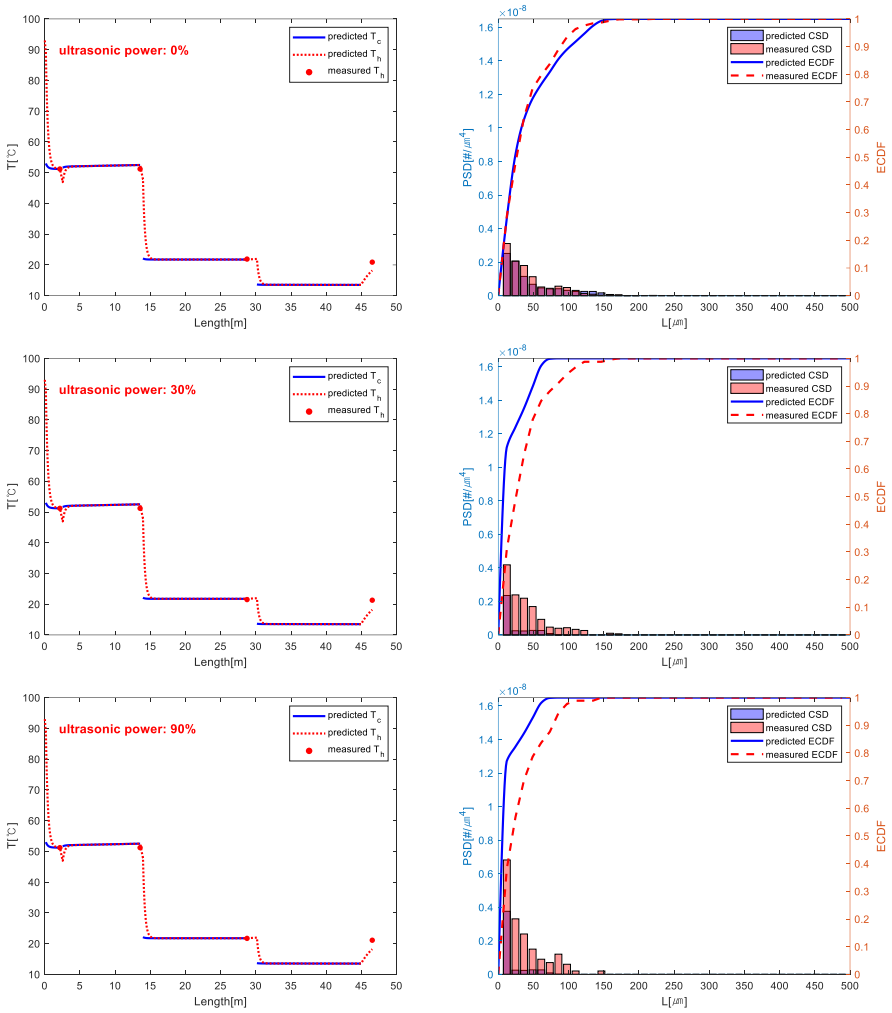

Figure S.9. The figures of experiment #25–27 in Table 6

Reference

1. Lee, Y., J. Park, and C. Han, *Modeling and Analysis of Frost Growth in Pilot-Scale Ambient Air Vaporizer.* Industrial & Engineering Chemistry Research, 2018. **57**(17): p. 5933-5943.
2. Lee, Y., J. Na, and W.B. Lee, *Robust design of ambient-air vaporizer based on time-series clustering.* Computers & Chemical Engineering, 2018. **118**: p. 236-247.
3. Mozdzierz, N.J., *Developing scalable and modular technologies for continuous biopharmaceutical production. (Unpublished doctoral dissertation)*, in *Chemical Engineering*. 2018, Massachusetts Institute of Technology, Cambridge, MA.
4. Li, H.-X. and C. Qi, *Modeling of distributed parameter systems for applications—A synthesized review from time–space separation.* Journal of Process Control, 2010. **20**(8): p. 891-901.
5. Fornberg, B. and D.M. Sloan, *A review of pseudospectral methods for solving partial differential equations.* Acta Numerica, 1994. **3**: p. 203-267.
6. Finlayson, B.A. and L.E. Scriven, *The method of weighted residuals—a review.* Appl. Mech. Rev, 1966. **19**(9): p. 735-748.
7. Patel, D., et al., *LNG vaporizer selection based on site ambient conditions.* Proceedings of the LNG, 2013. **17**: p. 16-19.
8. *Website of Global LNG Limited.* http://www.globallnginfo.com *(accessed August 2017).*
9. Egashira, S., *LNG vaporizer for LNG re-gasification terminal.* KOBELCO Technology Review, 2013. **32**: p. 64-69.
10. Dendy, T. and R. Nanda. *Utilization of atmospheric heat exchangers in LNG vaporization processes: a comparison of systems and methods*.

11. Kuang, Y.W., C.C. Yi, and W. Wang, *Numerical simulation of frosting behavior and its effect on a direct-contact ambient air vaporizer.* Journal of Natural Gas Science and Engineering, 2015. **27**: p. 55-63.
12. Liu, S., W. Jiao, and H. Wang, *Three-dimensional numerical analysis of the coupled heat transfer performance of LNG ambient air vaporizer.* Renewable Energy, 2016. **87**: p. 1105-1112.
13. Liu, S., et al., *Dynamic heat transfer analysis of liquefied natural gas ambient air vaporizer under frost conditions.* Applied Thermal Engineering, 2017. **110**: p. 999-1006.
14. Chen, S., S. Yao, and F. Xie, *Analysis of thermal conductivity of frost on cryogenic finned-tube vaporizer using fractal method.* Energy and power Engineering, 2013. **5**(04): p. 109.
15. Pandey, A.S., et al., *Performance testing and analysis of vertical ambient air vaporizers.* IOP Conference Series: Materials Science and Engineering, 2017. **171**: p. 012094.
16. Bernert, R.E., W. Everett, and R.E. Bernert, *Cryogenic ambient air vaporizers: frost growth, wind and seismic design for safety.* Cryogenics, 1993. **33**(8): p. 789-793.
17. Lee, K.-S., W.-S. Kim, and T.-H. Lee, *A one-dimensional model for frost formation on a cold flat surface.* International Journal of Heat and Mass Transfer, 1997. **40**(18): p. 4359-4365.
18. Lee, K.-S., S. Jhee, and D.-K. Yang, *Prediction of the frost formation on a cold flat surface.* International Journal of Heat and Mass Transfer, 2003. **46**(20): p. 3789-3796.
19. Yan, W.-M., et al., *Performance of finned tube heat exchangers operating under frosting conditions.* International Journal of Heat and Mass Transfer, 2003. **46**(5): p. 871-877.
20. Yang, D.-K. and K.-S. Lee, *Dimensionless correlations of frost properties on a cold plate.* International Journal of Refrigeration, 2004. **27**(1): p. 89-96.

21. Yang, D.-K., K.-S. Lee, and S. Song, *Modeling for predicting frosting behavior of a fin–tube heat exchanger.* International Journal of Heat and Mass Transfer, 2006. **49**(7): p. 1472-1479.
22. Hermes, C.J.L., et al., *A study of frost growth and densification on flat surfaces.* Experimental Thermal and Fluid Science, 2009. **33**(2): p. 371-379.
23. Kandula, M., *Frost growth and densification in laminar flow over flat surfaces.* International Journal of Heat and Mass Transfer, 2011. **54**(15): p. 3719-3731.
24. Kandula, M., *Frost growth and densification on a flat surface in laminar flow with variable humidity.* International Communications in Heat and Mass Transfer, 2012. **39**(8): p. 1030-1034.
25. Lee, S.H., et al., *Frost growth characteristics of spirally-coiled circular fin-tube heat exchangers under frosting conditions.* International Journal of Heat and Mass Transfer, 2013. **64**: p. 1-9.
26. Jeong, H.M., et al., *Experimental study on the characteristics of longitudinal fin air-heating vaporizers in different seasons.* Journal of Mechanical Science and Technology, 2008. **22**(5): p. 981-990.
27. Jeong, H.M., et al., *Natural convection heat transfer estimation from a longitudinally finned vertical pipe using CFD.* Journal of Mechanical Science and Technology, 2009. **23**(6): p. 1517-1527.
28. Jeong, H.-M., et al., *Optimum design of vaporizer fin with Liquefied Natural Gas by numerical analysis.* Journal of Mechanical Science and Technology, 2006. **20**(4): p. 545-553.
29. Bernert Jr, R.E. and R.E. Bernert Sr, *Ambient Air Vaporizer Fog Dispersal System. U.S. Patent 8,662,149*. July 15, 2014.
30. Bernert Jr, R.E. and R.E. Bernert Sr, *Frost Free Cryogenic Ambient Air Vaporizer. U.S. Patent 8,776,535*. March 4, 2014.
31. Mak, J., *Ambient Air Vaporizer. U.S. Patent 8,826,673*. September 9, 2014.

32. Mak, J., *Configurations and Methods for Waste Heat Recovery and Ambient Air Vaporizers in LNG Regasification. U.S. Patent 8,950,196*. February 10, 2015.
33. Iwasaki, M. and K. Asada, *Intermediate fluid type vaporizer*. 2002, Google Patents.
34. Kataoka, Y., M. Shimizu, and T. Watanabe, *Submerged combustion type vaporizer*. 1974, Google Patents.
35. Bernert Jr, R.E. and R.E. Bernert Sr, *Frost free cryogenic ambient air vaporizer*. 2014, Google Patents.
36. Kandula, M., *CORRELATION OF WATER FROST POROSITY IN LAMINAR FLOW OVER FLAT SURFACES.* 2012. **3**(1): p. 79-87.
37. Saul, A. and W. Wagner, *International Equations for the Saturation Properties of Ordinary Water Substance.* Journal of Physical and Chemical Reference Data, 1987. **16**(4): p. 893-901.
38. Perry, R.H., D.W. Green, and J.O. Maloney, *Perry's Chemical Engineers' Handbook, McGraw-Hill, New York, 1997.*
39. Bennett, C.O. and J.E. Myers, *Momentum, heat, and mass transfer*. Vol. 370. 1982: McGraw-Hill New York.
40. Incorpera, F.P., et al., *Fundamentals of heat and mass transfer.* John Wiley & Sons, 1996. **3**: p. 749-751.
41. Chilton, T.H. and A.P. Colburn, *Mass Transfer (Absorption) Coefficients Prediction from Data on Heat Transfer and Fluid Friction.* Industrial & Engineering Chemistry, 1934. **26**(11): p. 1183-1187.
42. Le Gall, R., *Experimental study and modeling of frost formation in heat exchangers.* 1994.
43. Salazar, A.n., *On thermal diffusivity.* European Journal of Physics, 2003. **24**(4): p. 351-358.
44. Lee, K.S., T.H. Lee, and W.S. Kim, *Heat and mass transfer of parallel plate heat exchanger under frosting condition.* SAREK Journal, 1994. **6**(2): p. 155-165.

45. Barron, R.F.N., G. F., *Cryogenic Heat Transfer*. 1999, Taylor & Francis: Philadelphia.
46. Ahmad, M.I., N. Zhang, and M. Jobson, *Modelling and optimisation for design of hydrogen networks for multi-period operation.* Journal of Cleaner Production, 2010. **18**(9): p. 889-899.
47. Fazlollahi, S. and F. Maréchal, *Multi-objective, multi-period optimization of biomass conversion technologies using evolutionary algorithms and mixed integer linear programming (MILP).* Applied Thermal Engineering, 2013. **50**(2): p. 1504-1513.
48. Isafiade, A., et al., *Optimal synthesis of heat exchanger networks for multi-period operations involving single and multiple utilities.* Chemical Engineering Science, 2015. **127**: p. 175-188.
49. Isafiade, A.J. and D.M. Fraser, *Interval based MINLP superstructure synthesis of heat exchanger networks for multi-period operations.* Chemical Engineering Research and Design, 2010. **88**(10): p. 1329-1341.
50. Ma, X., et al., *Synthesis of multi-stream heat exchanger network for multi-period operation with genetic/simulated annealing algorithms.* Applied Thermal Engineering, 2008. **28**(8): p. 809-823.
51. Papalexandri, K.P. and E.N. Pistikopoulos, *A multiperiod MINLP model for the synthesis of flexible heat and mass exchange networks.* Computers & Chemical Engineering, 1994. **18**(11): p. 1125-1139.
52. Ukkusuri, S.V. and G. Patil, *Multi-period transportation network design under demand uncertainty.* Transportation Research Part B: Methodological, 2009. **43**(6): p. 625-642.
53. Zeballos, L.J., et al., *Multi-period design and planning of closed-loop supply chains with uncertain supply and demand.* Computers & Chemical Engineering, 2014. **66**: p. 151-164.
54. Zhang, W.V.N., *Design of flexible heat exchanger network for multi-period operation.* Chemical Engineering Science, 2006. **61**(23): p. 7730-7753.

55. Calafiore, G.C. and M.C. Campi, *The scenario approach to robust control design.* IEEE Transactions on Automatic Control, 2006. **51**(5): p. 742-753.
56. Chen, W., et al., *A Procedure for Robust Design: Minimizing Variations Caused by Noise Factors and Control Factors.* Journal of Mechanical Design, 1996. **118**(4): p. 478-485.
57. Gu, X., et al., *Worst case propagated uncertainty of multidisciplinary systems in robust design optimization.* Structural and Multidisciplinary Optimization, 2000. **20**(3): p. 190-213.
58. Parkinson, A., C. Sorensen, and N. Pourhassan, *A General Approach for Robust Optimal Design.* Journal of Mechanical Design, 1993. **115**(1): p. 74-80.
59. Vorobyov, S.A., A.B. Gershman, and L. Zhi-Quan, *Robust adaptive beamforming using worst-case performance optimization: a solution to the signal mismatch problem.* IEEE Transactions on Signal Processing, 2003. **51**(2): p. 313-324.
60. Lucor, D., et al., *Stochastic design optimization: Application to reacting flows.* Computer Methods in Applied Mechanics and Engineering, 2007. **196**(49): p. 5047-5062.
61. Shen, D.E. and R.D. Braatz, *Polynomial chaos-based robust design of systems with probabilistic uncertainties.* AIChE Journal, 2016. **62**(9): p. 3310-3318.
62. Xiong, F., et al. *Polynomial chaos expansion based robust design optimization*. in *2011 International Conference on Quality, Reliability, Risk, Maintenance, and Safety Engineering*. 2011.
63. Ratanamahatana, C., et al. *A Novel Bit Level Time Series Representation with Implication of Similarity Search and Clustering*. in *Advances in Knowledge Discovery and Data Mining*. 2005. Berlin, Heidelberg: Springer Berlin Heidelberg.
64. Lin, J., et al., *A symbolic representation of time series, with implications for streaming algorithms*, in *Proceedings of the 8th ACM*

SIGMOD workshop on Research issues in data mining and knowledge discovery. 2003, ACM: San Diego, California. p. 2-11.

65. Seifert, B. and T. Gasser, *Data Adaptive Ridging in Local Polynomial Regression.* Journal of Computational and Graphical Statistics, 2000. **9**(2): p. 338-360.
66. Tufts, D.W., R. Kumaresan, and I. Kirsteins, *Data adaptive signal estimation by singular value decomposition of a data matrix.* Proceedings of the IEEE, 1982. **70**(6): p. 684-685.
67. Aghabozorgi, S., A. Seyed Shirkhorshidi, and T. Ying Wah, *Time-series clustering – A decade review.* Information Systems, 2015. **53**: p. 16-38.
68. Kim, J.M., et al. *Signal processing using Fourier & wavelet transform for pulse oximetry*. IEEE.
69. Mörchen, F., *Time series feature extraction for data mining using DWT and DFT*. 2003, Univ.
70. Wu, Y.-L., D. Agrawal, and A.E. Abbadi, *A comparison of DFT and DWT based similarity search in time-series databases*, in *Proceedings of the ninth international conference on Information and knowledge management*. 2000, ACM: McLean, Virginia, USA. p. 488-495.
71. Bruce, L.M., C.H. Koger, and L. Jiang, *Dimensionality reduction of hyperspectral data using discrete wavelet transform feature extraction.* IEEE Transactions on Geoscience and Remote Sensing, 2002. **40**(10): p. 2331-2338.
72. Das, D., N.K. Singh, and A.K. Sinha, *A comparison of Fourier transform and wavelet transform methods for detection and classification of faults on transmission lines.* IEEE Power India Conference, 2006(237).
73. Vlachos, M., et al. *A wavelet-based anytime algorithm for k-means clustering of time series*. Citeseer.
74. Daubechies, I., *The wavelet transform, time-frequency localization and signal analysis.* IEEE Transactions on Information Theory, 1990. **36**(5): p. 961-1005.

75. Stanković, R.S. and B.J. Falkowski, *The Haar wavelet transform: its status and achievements.* Computers & Electrical Engineering, 2003. **29**(1): p. 25-44.
76. Sobol', I.M., *Global sensitivity indices for nonlinear mathematical models and their Monte Carlo estimates.* Mathematics and Computers in Simulation, 2001. **55**(1): p. 271-280.
77. Cannavó, F., *Sensitivity analysis for volcanic source modeling quality assessment and model selection.* Computers & Geosciences, 2012. **44**: p. 52-59.
78. Sobol, I.M., *Sensitivity estimates for nonlinear mathematical models.* Mathematical modelling and computational experiments, 1993. **1**(4): p. 407-414.
79. Soboĺ, I.M., *Quasi-Monte Carlo methods.* Progress in Nuclear Energy, 1990. **24**(1): p. 55-61.
80. MacQueen, J. *Some methods for classification and analysis of multivariate observations*. Oakland, CA, USA.
81. Na, J., Y. Lim, and C. Han, *A modified DIRECT algorithm for hidden constraints in an LNG process optimization.* Energy, 2017. **126**: p. 488-500.
82. Rios, L.M. and N.V. Sahinidis, *Derivative-free optimization: a review of algorithms and comparison of software implementations.* Journal of Global Optimization, 2013. **56**(3): p. 1247-1293.
83. Jones, D.R., C.D. Perttunen, and B.E. Stuckman, *Lipschitzian optimization without the Lipschitz constant.* Journal of Optimization Theory and Applications, 1993. **79**(1): p. 157-181.
84. Zou, K.H., K. Tuncali, and S.G. Silverman, *Correlation and Simple Linear Regression.* Radiology, 2003. **227**(3): p. 617-628.
85. Nagy, Z.K., M. Fujiwara, and R.D. Braatz, *Modelling and control of combined cooling and antisolvent crystallization processes.* Journal of Process Control, 2008. **18**(9): p. 856-864.

86. Zydney, A.L., *Continuous downstream processing for high value biological products: A Review.* 2016. **113**(3): p. 465-475.
87. Kleinebudde, P., J. Khinast, and J. Rantanen, *Continuous manufacturing of pharmaceuticals*. Vol. 7703. 2017: John Wiley & Sons.
88. Jiang, M. and R.D. Braatz, *Low-Cost Noninvasive Real-Time Imaging for Tubular Continuous-Flow Crystallization.* 2018. **41**(1): p. 143-148.
89. Jiang, M., et al., *Opportunities and challenges of real-time release testing in biopharmaceutical manufacturing.* 2017. **114**(11): p. 2445-2456.
90. Barrett, P., et al., *A Review of the Use of Process Analytical Technology for the Understanding and Optimization of Production Batch Crystallization Processes.* Organic Process Research & Development, 2005. **9**(3): p. 348-355.
91. Croughan, M.S., K.B. Konstantinov, and C. Cooney, *The future of industrial bioprocessing: Batch or continuous?* 2015. **112**(4): p. 648-651.
92. LaPorte, T.L. and C. Wang, *Continuous processes for the production of pharmaceutical intermediates and active pharmaceutical ingredients.* Current opinion in drug discovery & development, 2007. **10**(6): p. 738-745.
93. Hong, M.S., et al., *Challenges and opportunities in biopharmaceutical manufacturing control.* Computers & Chemical Engineering, 2018. **110**: p. 106-114.
94. Wiedmeyer, V., et al., *Continuous Crystallization in a Helically Coiled Flow Tube: Analysis of Flow Field, Residence Time Behavior, and Crystal Growth.* Industrial & Engineering Chemistry Research, 2017. **56**(13): p. 3699-3712.
95. Rivera, T. and A.D. Randolph, *A model for the precipitation of pentaerythritol tetranitrate (PETN).* Engineering Chemistry Process Design Development, 1978. **17**(2): p. 182-188.

96. Alvarez, A.J. and A.S. Myerson, *Continuous Plug Flow Crystallization of Pharmaceutical Compounds.* Crystal Growth & Design, 2010. **10**(5): p. 2219-2228.
97. Lemaître, J., et al., *Réacteur continu à écoulement segmenté pour la synthèse de poudres minérales par précipitation*.
98. Vacassy, R., et al., *Calcium carbonate precipitation using new segmented flow tubular reactor.* AIChE Journal, 2004. **46**(6): p. 1241-1252.
99. Eder, R.J.P., et al., *Continuously Seeded, Continuously Operated Tubular Crystallizer for the Production of Active Pharmaceutical Ingredients.* Crystal Growth & Design, 2010. **10**(5): p. 2247-2257.
100. Eder, R.J.P., et al., *Continuous Sonocrystallization of Acetylsalicylic Acid (ASA): Control of Crystal Size.* Crystal Growth & Design, 2012. **12**(10): p. 4733-4738.
101. Furuta, M., et al., *Continuous crystallization using a sonicated tubular system for controlling particle size in an API manufacturing process.* Chemical Engineering and Processing: Process Intensification, 2016. **102**: p. 210-218.
102. Jiang, M., et al., *Modification of Crystal Shape through Deep Temperature Cycling.* Industrial & Engineering Chemistry Research, 2014. **53**(13): p. 5325-5336.
103. Jiang, M., et al., *Indirect Ultrasonication in Continuous Slug-Flow Crystallization.* Crystal Growth & Design, 2015. **15**(5): p. 2486-2492.
104. Jiang, M., et al., *Continuous-Flow Tubular Crystallization in Slugs Spontaneously Induced by Hydrodynamics.* Crystal Growth & Design, 2014. **14**(2): p. 851-860.
105. Jiang, M., C. Gu, and R.D. Braatz, *Analysis of focused indirect ultrasound via high-speed spatially localized pressure sensing and its consequences on nucleation.* Chemical Engineering and Processing: Process Intensification, 2017. **117**: p. 186-194.

106. Eder, R.J.P., et al., *Seed loading effects on the mean crystal size of acetylsalicylic acid in a continuous-flow crystallization device.* Crystal Research and Technology, 2011. **46**(3): p. 227-237.
107. Jiang, M., et al., *Towards achieving a flattop crystal size distribution by continuous seeding and controlled growth.* Chemical Engineering Science, 2012. **77**: p. 2-9.
108. Estel, L., et al., *Distributed state estimation of a counter current heat exchanger under varying flow rate.* Computers & Chemical Engineering, 2000. **24**(1): p. 53-60.
109. Arbaoui, M.A., et al., *Counter-current tubular heat exchanger: Modeling and adaptive predictive functional control.* Applied Thermal Engineering, 2007. **27**(13): p. 2332-2338.
110. Ansari, M.R. and V. Mortazavi, *Simulation of dynamical response of a countercurrent heat exchanger to inlet temperature or mass flow rate change.* Applied Thermal Engineering, 2006. **26**(17): p. 2401-2408.
111. Rasche, M.L., M. Jiang, and R.D. Braatz, *Mathematical modeling and optimal design of multi-stage slug-flow crystallization.* Computers & Chemical Engineering, 2016. **95**: p. 240-248.
112. Bergman, T.L., et al., *Fundamentals of heat and mass transfer*. 2011: John Wiley & Sons.
113. Myerson, A., *Handbook of industrial crystallization*. 2002: Butterworth-Heinemann.
114. Erdemir, D., A.Y. Lee, and A.S. Myerson, *Nucleation of Crystals from Solution: Classical and Two-Step Models.* Accounts of Chemical Research, 2009. **42**(5): p. 621-629.
115. Vekilov, P.G., *The two-step mechanism of nucleation of crystals in solution.* Nanoscale, 2010. **2**(11): p. 2346-2357.
116. Zahn, D., *Thermodynamics and Kinetics of Prenucleation Clusters, Classical and Non-Classical Nucleation.* ChemPhysChem, 2015. **16**(10): p. 2069-2075.

117. Wirges, H.-P., *The Kinetics of Industrial Crystallization.* Chemie Ingenieur Technik, 1986. **58**(8): p. 665-665.
118. Ruckenstein, E. and B. Nowakowski, *A kinetic theory of nucleation in liquids.* Journal of Colloid and Interface Science, 1990. **137**(2): p. 583-592.
119. Kurotani, M., et al., *Effect of ultrasonic irradiation on the behavior of primary nucleation of amino acids in supersaturated solutions.* Journal of Crystal Growth, 2009. **311**(9): p. 2714-2721.
120. Miyasaka, E., S. Ebihara, and I. Hirasawa, *Investigation of primary nucleation phenomena of acetylsalicylic acid crystals induced by ultrasonic irradiation—ultrasonic energy needed to activate primary nucleation.* Journal of Crystal Growth, 2006. **295**(1): p. 97-101.
121. Agrawal, S.G. and A.H.J. Paterson, *Secondary Nucleation: Mechanisms and Models.* Chemical Engineering Communications, 2015. **202**(5): p. 698-706.
122. Garnier, S., S. Petit, and G. Coquerel, *Influence of supersaturation and structurally related additives on the crystal growth of α-lactose monohydrate.* Journal of Crystal Growth, 2002. **234**(1): p. 207-219.
123. Meyer, H.J., *The influence of impurities on the growth rate of calcite.* Journal of Crystal Growth, 1984. **66**(3): p. 639-646.
124. Sangwal, K., *Effects of impurities on crystal growth processes.* Progress in Crystal Growth and Characterization of Materials, 1996. **32**(1): p. 3-43.
125. Myers-Beaghton, A.K. and D.D. Vvedensky, *Generalized Burton-Cabrera-Frank theory for growth and equilibration on stepped surfaces.* Physical Review A, 1991. **44**(4): p. 2457-2468.
126. Woodruff, D.P., *How does your crystal grow? A commentary on Burton, Cabrera and Frank (1951) 'The growth of crystals and the equilibrium structure of their surfaces'.* Philosophical Transactions of the Royal Society A, Mathematical, Physical and Engineering Sciences, 2015. **373**(2039).

127. Burton, W.K., N. Cabrera, and F.C. Frank, *The growth of crystals and the equilibrium structure of their surfaces.* Philosophical Transactions of the Royal Society of London. Series A, Mathematical and Physical Sciences, 1951. **243**(866): p. 299.
128. Ruecroft, G., et al., *Sonocrystallization: The Use of Ultrasound for Improved Industrial Crystallization.* Organic Process Research & Development, 2005. **9**(6): p. 923-932.
129. Pinar, Z., et al., *Analytical solution of population balance equation involving growth, nucleation and aggregation in terms of auxiliary equation method.* Applied Mathematics & Information Sciences, 2015. **9**(5): p. 2467.
130. Gagnon, P., *Technology trends in antibody purification.* Journal of Chromatography A, 2012. **1221**: p. 57-70.
131. Jungbauer, A., *Continuous downstream processing of biopharmaceuticals.* Trends in Biotechnology, 2013. **31**(8): p. 479-492.
132. Konstantinov, K.B. and C.L. Cooney, *White Paper on Continuous Bioprocessing May 20–21 2014 Continuous Manufacturing Symposium.* Journal of Pharmaceutical Sciences, 2015. **104**(3): p. 813-820.
133. Kelley, B., *Very Large Scale Monoclonal Antibody Purification: The Case for Conventional Unit Operations.* Biotechnology Progress, 2008. **23**(5): p. 995-1008.
134. Kelley, B., *Industrialization of mAb production technology: The bioprocessing industry at a crossroads.* mAbs, 2009. **1**(5): p. 443-452.
135. Zydney, A.L., *Continuous downstream processing for high value biological products: A Review.* Biotechnology and Bioengineering, 2015. **113**(3): p. 465-475.
136. Bryntesson, M., M. Hall, and K. Lacki, *Chromatography method*. 2011, Google Patents.

137. Warikoo, V., et al., *Integrated continuous production of recombinant therapeutic proteins.* Biotechnology and Bioengineering, 2012. **109**(12): p. 3018-3029.
138. Eggersgluess, J., T. Wellsandt, and J. Strube, *Integration of Aqueous Two-Phase Extraction into Downstream Processing.* Chemical Engineering & Technology, 2014. **37**(10): p. 1686-1696.
139. Hammerschmidt, N., et al., *Economics of recombinant antibody production processes at various scales: Industry-standard compared to continuous precipitation.* Biotechnology Journal, 2014. **9**(6): p. 766-775.
140. Neugebauer, P. and J.G. Khinast, *Continuous Crystallization of Proteins in a Tubular Plug-Flow Crystallizer.* Crystal Growth & Design, 2015. **15**(3): p. 1089-1095.
141. Hekmat, D., *Large-scale crystallization of proteins for purification and formulation.* Bioprocess and Biosystems Engineering, 2015. **38**(7): p. 1209-1231.
142. McPherson, A., *Introduction to protein crystallization.* Methods, 2004. **34**(3): p. 254-265.
143. Russo Krauss, I., et al., *An Overview of Biological Macromolecule Crystallization.* International Journal of Molecular Sciences, 2013. **14**(6).
144. Baker, J.C. and B.M. Roberts, *Preparation of stable insulin analog crystals. U.S. Patent 5,597,893*. Jan 28, 1997.
145. Zhang, D., et al., *Progress of Pharmaceutical Continuous Crystallization.* Engineering, 2017. **3**(3): p. 354-364.
146. Forsythe, E.L., R.A. Judge, and M.L. Pusey, *Tetragonal Chicken Egg White Lysozyme Solubility in Sodium Chloride Solutions.* Journal of Chemical & Engineering Data, 1999. **44**(3): p. 637-640.
147. Chayen, N.E., *Methods for separating nucleation and growth in protein crystallisation.* Progress in Biophysics and Molecular Biology, 2005. **88**(3): p. 329-337.

148. Pons Siepermann, C.A., S. Huang, and A.S. Myerson, *Nucleation Inhibition of Benzoic Acid through Solution Complexation.* Crystal Growth & Design, 2017. **17**(5): p. 2646-2653.
149. Dombrowski, R.T., *1 - Microscopy techniques for analyzing the phase nature and morphology of biomaterials*, in *Characterization of Biomaterials*, M. Jaffe, et al., Editors. 2013, Woodhead Publishing. p. 1-33.
150. Ranodolph, A., *Theory of particulate processes: analysis and techniques of continuous crystallization*. 2012: Elsevier.
151. Varlashkin, P., *Approaches to quantification of amorphous content in crystalline drug substance by powder X-ray diffraction.* American Pharmaceutical Review, 2011. **14**(1).
152. Speakman, S., *Basics of X-Ray Powder Diffraction: Training to Become an Independent User of the X-Ray SEF at the Center for Materials Science and Engineering at MIT.* Online][Cited: April 6, 2017.] http://prism.mit.edu/xray/oldsite/Basics%20of%20X-Ray%20Powder%20Diffraction.pdf.
153. Bates, S., et al., *Analysis of Amorphous and Nanocrystalline Solids from Their X-Ray Diffraction Patterns.* Pharmaceutical Research, 2006. **23**(10): p. 2333-2349.
154. Kemethmüller, S., et al., *Quantitative Analysis of Crystalline and Amorphous Phases in Glass–Ceramic Composites Like LTCC by the Rietveld Method.* Journal of the American Ceramic Society, 2006. **89**(8): p. 2632-2637.
155. Kumar, R., et al., *Development of sodium acetate trihydrate-ethylene glycol composite phase change materials with enhanced thermophysical properties for thermal comfort and therapeutic applications.* Scientific Reports, 2017. **7**(1): p. 5203.
156. Schneider, C., et al., *Applications of ethylene vinyl acetate copolymers (EVA) in drug delivery systems.* Journal of Controlled Release, 2017. **262**: p. 284-295.

157. Henderson, A.M., *Ethylene-vinyl acetate (EVA) copolymers: a general review.* IEEE Electrical Insulation Magazine, 1993. **9**(1): p. 30-38.
158. McKeen, L.W., *The effect of sterilization on plastics and elastomers*. 2018: William Andrew.
159. Eckes, D. and M. Busch, *Coupled Deterministic and Stochastic Modeling of an Industrial Multi-Zone LDPE Autoclave Reactor.* Macromolecular Symposia, 2016. **360**(1): p. 23-31.
160. Sivalingam, G., N.J. Soni, and S.M. Vakil, *Detection of decomposition for high pressure ethylene/vinyl acetate copolymerization in autoclave reactor using principal component analysis on heat balance model.* The Canadian Journal of Chemical Engineering, 2015. **93**(6): p. 1063-1075.
161. Brandolin, A., et al., *Prediction of molecular weight distributions by probability generating functions. Application to industrial autoclave reactors for high pressure polymerization of ethylene and ethylene-vinyl acetate.* Polymer Engineering & Science, 2001. **41**(8): p. 1413-1426.
162. Kiparissides, C., et al., *Mathematical Modeling of Free-Radical Ethylene Copolymerization in High-Pressure Tubular Reactors.* Industrial & Engineering Chemistry Research, 2005. **44**(8): p. 2592-2605.
163. López-Carpy, B., et al., *Mathematical Modeling of the Molecular Weight Distribution in Low Density Polyethylene. I. Steady-State Operation of Multizone Autoclave Reactors.* 2018. **12**(4): p. 1800013.
164. Zabisky, R.C.M., et al., *A kinetic model for olefin polymerization in high-pressure tubular reactors: a review and update.* Polymer, 1992. **33**(11): p. 2243-2262.
165. Bjerve Sund, E. and K. Lien, *Simultaneous optimization of mixing patterns and feed distribution in LDPE autoclave reactors.* Computers & Chemical Engineering, 1997. **21**: p. S1031-S1036.

166. Chien, I.L., T.W. Kan, and B.-S. Chen, *Dynamic simulation and operation of a high pressure ethylene-vinyl acetate (EVA) copolymerization autoclave reactor.* Computers & Chemical Engineering, 2007. **31**(3): p. 233-245.
167. Ghiass, M. and R.A. Hutchinson, *Simulation of Free Radical High-Pressure Copolymerization in a Multizone Autoclave: Model Development and Application.* Polymer Reaction Engineering, 2003. **11**(4): p. 989-1015.
168. Jacob, N.C. and R. Dhib, *Nonlinear MPC of a multi-zone multi-feed LDPE autoclave reactor.* Journal of Industrial and Engineering Chemistry, 2012. **18**(5): p. 1781-1795.
169. Kolhapure, N.H. and R.O. Fox, *CFD analysis of micromixing effects on polymerization in tubular low-density polyethylene reactors.* Chemical Engineering Science, 1999. **54**(15): p. 3233-3242.
170. Read, N.K., S.X. Zhang, and W.H. Ray, *Simulations of a LDPE reactor using computational fluid dynamics.* AIChE Journal, 1997. **43**(1): p. 104-117.
171. Zhang, C., et al., *Simulation and optimization of polymer molecular weight distribution with nonideal reactors.* Computers & Chemical Engineering, 2017. **106**: p. 744-757.
172. Zhou, W., E. Marshall, and L. Oshinowo, *Modeling LDPE Tubular and Autoclave Reactors.* Industrial & Engineering Chemistry Research, 2001. **40**(23): p. 5533-5542.
173. Bezzo, F., S. Macchietto, and C.C. Pantelides, *A general methodology for hybrid multizonal/CFD models: Part I. Theoretical framework.* Computers & Chemical Engineering, 2004. **28**(4): p. 501-511.
174. Wells, G.J. and W.H. Ray, *Mixing effects on performance and stability of low-density polyethylene reactors.* AIChE Journal, 2005. **51**(12): p. 3205-3218.

175. Zahradník, J., et al., *A networks-of-zones analysis of mixing and mass transfer in three industrial bioreactors.* Chemical Engineering Science, 2001. **56**(2): p. 485-492.
176. Bezzo, F. and S. Macchietto, *A general methodology for hybrid multizonal/CFD models: Part II. Automatic zoning.* Computers & Chemical Engineering, 2004. **28**(4): p. 513-525.
177. Seppälä, M., et al. *Development of automatic algorithm for combining CFD and multiblock modelling and application to flotation cell*. in *6th International Conference on Computational Fluid Dynamics in the Oil & Gas, Metallurgical and Process Industries*. 2008.
178. Bezzo, F., S. Macchietto, and C.C. Pantelides, *General hybrid multizonal/CFD approach for bioreactor modeling.* AIChE Journal, 2003. **49**(8): p. 2133-2148.
179. Delafosse, A., et al., *CFD-based compartment model for description of mixing in bioreactors.* Chemical Engineering Science, 2014. **106**: p. 76-85.
180. Delafosse, A., et al., *Development of a compartment model based on CFD simulations for description of mixing in bioreactors.* Biotechnol. Agron. Soc. Environ, 2010. **14**(S2): p. 517-522.
181. Nauha, E.K. and V. Alopaeus, *Modeling method for combining fluid dynamics and algal growth in a bubble column photobioreactor.* Chemical Engineering Journal, 2013. **229**: p. 559-568.
182. Alvarado, A., et al., *A compartmental model to describe hydraulics in a full-scale waste stabilization pond.* Water Research, 2012. **46**(2): p. 521-530.
183. Bertrand, M., et al., *Hybrid LES–multizonal modelling of the uranium oxalate precipitation.* Chemical Engineering Science, 2012. **77**: p. 95-104.
184. Bashiri, H., F. Bertrand, and J. Chaouki, *Development of a multiscale model for the design and scale-up of gas/liquid stirred tank reactors.* Chemical Engineering Journal, 2016. **297**: p. 277-294.

185. Bashiri, H., et al., *Compartmental modelling of turbulent fluid flow for the scale-up of stirred tanks.* The Canadian Journal of Chemical Engineering, 2014. **92**(6): p. 1070-1081.
186. Bermingham, S.K., et al., *Hybrid CFD–multizonal modelling of polymorphs and agglomeration phenomena in crystallisation process.* Chem. Eng. Trans, 2007. **11**: p. 149-154.
187. Du, Y., et al., *Equivalent Reactor Network Model for the Modeling of Fluid Catalytic Cracking Riser Reactor.* Industrial & Engineering Chemistry Research, 2015. **54**(35): p. 8732-8742.
188. Yu, X., et al., *A compartmental CFD-PBM model of high shear wet granulation.* AIChE Journal, 2017. **63**(2): p. 438-458.
189. Ham, J.Y. and H.-K. Rhee, *Modeling and control of an LDPE autoclave reactor.* Journal of Process Control, 1996. **6**(4): p. 241-246.
190. Zhang, S.X., N.K. Read, and W.H. Ray, *Runaway phenomena in low-density polyethylene autoclave reactors.* AIChE Journal, 1996. **42**(10): p. 2911-2925.
191. Menter, F.R., R. Langtry, and S. Völker, *Transition Modelling for General Purpose CFD Codes.* Flow, Turbulence and Combustion, 2006. **77**(1): p. 277-303.
192. Lanzafame, R., S. Mauro, and M. Messina, *Wind turbine CFD modeling using a correlation-based transitional model.* Renewable Energy, 2013. **52**: p. 31-39.
193. Kinzl, M., et al., *Viscosity of solutions of low-density polyethylene in ethylene as a function of temperature and pressure.* Journal of Rheology, 2003. **47**(4): p. 869-877.
194. Zhang, S.X. and W.H. Ray, *Modeling of imperfect mixing and its effects on polymer properties.* AIChE Journal, 1997. **43**(5): p. 1265-1277.
195. Wells, G.J. and W.H. Ray, *Methodology for modeling detailed imperfect mixing effects in complex reactors.* AIChE Journal, 2005. **51**(5): p. 1508-1520.

196. Tosun, G. and A. Bakker, *A Study of Macrosegregation in Low-Density Polyethylene Autoclave Reactors by Computational Fluid Dynamic Modeling.* Industrial & Engineering Chemistry Research, 1997. **36**(2): p. 296-305.
197. Sarmoria, C., et al., *Modeling of molecular weights in industrial autoclave reactors for high pressure polymerization of ethylene and ethylene-vinyl acetate.* Polymer Engineering & Science, 2000. **40**(6): p. 1480-1494.
198. Chan, W.-M., P.E. Gloor, and A.E. Hamielec, *A kinetic model for olefin polymerization in high-pressure autoclave reactors.* AIChE Journal, 1993. **39**(1): p. 111-126.
199. Smedberg, A., T. Hjertberg, and B. Gustafsson, *Crosslinking reactions in an unsaturated low density polyethylene.* Polymer, 1997. **38**(16): p. 4127-4138.
200. Smedberg, A., T. Hjertberg, and B. Gustafsson, *The role of entanglements in network formation in unsaturated low density polyethylene.* Polymer, 2004. **45**(14): p. 4867-4875.
201. Soares, J.B.P., *Mathematical modelling of the microstructure of polyolefins made by coordination polymerization: a review.* Chemical Engineering Science, 2001. **56**(13): p. 4131-4153.
202. Xie, T.Y. and A.E. Hamielec, *Modelling free-radical copolymerization kinetics—evaluation of the pseudo-kinetic rate constant method, 2. Molecular weight calculations for copolymers with long chain branching.* Macromolecular Theory and Simulations, 1993. **2**(3): p. 455-483.
203. Hamielec, A.E., J.F. MacGregor, and A. Penlidis, *Multicomponent free-radical polymerization in batch, semi- batch and continuous reactors.* Makromolekulare Chemie. Macromolecular Symposia, 1987. **10-11**(1): p. 521-570.

204. Byrne, G.D. and A.C. Hindmarsh, *PVODE, an ODE Solver for Parallel Computers.* The International Journal of High Performance Computing Applications, 1999. **13**(4): p. 354-365.
205. Cohen, S.D., A.C. Hindmarsh, and P.F. Dubois, *CVODE, a stiff/nonstiff ODE solver in C.* Computers in physics, 1996. **10**(2): p. 138-143.
206. Hindmarsh, A.C., *The PVODE and IDA Algorithms*. 2000: United States.
207. Hindmarsh, A.C., et al., *SUNDIALS: Suite of nonlinear and differential/algebraic equation solvers %J ACM Trans. Math. Softw.* 2005. **31**(3): p. 363-396.
208. Serban, R. and A.C. Hindmarsh, *CVODES: The Sensitivity-Enabled ODE Solver in SUNDIALS.* 2005(47438): p. 257-269.
209. Langtry, R. and F. Menter, *Transition Modeling for General CFD Applications in Aeronautics*, in *43rd AIAA Aerospace Sciences Meeting and Exhibit*. 2005, American Institute of Aeronautics and Astronautics.
210. Sommerfeld, M. and S. Decker, *State of the Art and Future Trends in CFD Simulation of Stirred Vessel Hydrodynamics.* Chemical Engineering & Technology, 2004. **27**(3): p. 215-224.
211. Vrábel, P., et al., *Compartment Model Approach: Mixing in Large Scale Aerated Reactors with Multiple Impellers.* Chemical Engineering Research and Design, 1999. **77**(4): p. 291-302.
212. Vrábel, P., et al., *Mixing in large-scale vessels stirred with multiple radial or radial and axial up-pumping impellers: modelling and measurements.* Chemical Engineering Science, 2000. **55**(23): p. 5881-5896.
213. Saldívar-Guerra, E., et al., *Cover Picture: Macromol. React. Eng. 2/2016.* Macromolecular Reaction Engineering, 2016. **10**(2): p. 91-91.
214. Pladis, P. and C. Kiparissides, *A comprehensive model for the calculation of molecular weight–long-chain branching distribution in free-radical polymerizations.* Chemical Engineering Science, 1998. **53**(18): p. 3315-3333.

215. Beuermann, S., M. Buback, and D. Nelke, *Pressure dependence of the propagation rate coefficient kp for vinyl acetate polymerizations in bulk and in solution of fluid CO2.* Macromolecules, 2001. **34**(19): p. 6637-6640.
216. Brandrup, J., et al., *Polymer handbook*. Vol. 7. 1989: Wiley New York etc.
217. Roberts, D.E., *Heats of polymerization. A summary of published values and their relation to structure.* Journal of Research of the National Bureau of Standards, 1950. **44**: p. 221-232.
218. Jessup, R.S., *The Heat and Free Energy of Polymerization of Ethylene.* 1948. **16**(7): p. 661-664.

Abstract in Korean (국문초록)

최근에 몇 년에 걸쳐서 많은 연구자들이 이론을 기반으로 실험 결과와 일치하는 수학 모델을 개발하고자 많은 노력을 기울여 왔다. 하지만 이런 노력에도 불구하고 다상 흐름 혹은 교반 반응기와 같은 복잡한 현상을 내포한 시스템을 위한 모델을 수립하는 것은 여전히 화학 공학 분야에서 쉽지 않은 일로 여겨진다. 이 와중에 다양한 수치적 방법에서의 계산 효율의 증가와 안정성의 향상은 기본방정식에 기초한 시스템을 정확하게 해결하고 분석할 수 있게 해주었다. 이로 인하여 내부 요소들 간의 상호 의존성이 존재하는 시스템의 거동을 정확하게 예측하기 위한 수학적 모델의 필요성이 부각되었다. 기본 현상들을 표현할 수 있는 방정식들을 기반으로 모델을 구축하기 위한 방법론은 시스템 해석에 있어서 기술적 장벽을 낮출 수 있다.

이 학위 논문에서 우리는 실험실 또는 파일럿 규모의 실험으로부터 입증된 세 가지 수학적 모델을 제안한다. 첫 번째로, 공기를 사용하여 액상의 천연가스를 기화시키는 장치는 운전 도중에 기화기 표면에 서리 층이 형성되고 그로 인한 단열 효과로 장비의 성능이 서서히 저하된다. 시스템은 주변 공기를 열 흡수원으로 사용하기 때문에 시스템 특성의 변동을 파악하기 위해서는 공기 중 수증기 및 천연 가스의 상전이 및 전달 현상을 동시에 고려하여야 한다. 제시된 수학적 모델에 의해 예측한 결과는 파일럿 규모 기화기로부터 얻은 실험 데이터와 5.5% 평균 절대

오차를 보였다. 이에 더하여, 앞에서 제시한 기화기 모델을 이용하여 1 년 동안의 기상 조건에서 운전 효율을 유지하면서 지속 운전이 가능한 기화기의 설계 방법과 결과를 제안하였다. 이산 파형 변환과 k-평균 군집화를 포함하는 두 가지 이상의 데이터 분석 기법을 사용하여 시계열 데이터를 대표할 수 있는 특징을 추출한다. 추출된 특징 아래에서 최적화된 디자인은 기존 제시된 안에 비해 22.92% 만큼 향상된 성능을 보여주었다. 두 번째 시스템은 신제약 기술 공정인 연속 관형 결정화 반응기는 기존에 널리 쓰이던 회분식 반응기에 비하여 생산 속도 및 스케일 업 측면에서 장점이 많다. 하지만 제어기술이 기반이 되어야한다는 점에 있어서 그 도입이 늦어졌고 이에 따라 자연스럽게 개발된 모델 또한 전무하다. 우리는 이 장치에서 결정 크기 분포를 추산하기 위한 인구 균형 모델을 열 교환 모델과 동시에 고려하여 결정 크기 분포를 추산할 수 있었다. 제 1 원리 결정 반응식을 기반으로 구축된 모델은 완전 요인 배치법을 기반으로 실험된 데이터를 성공적으로 예측하였다. 결정이 액상에 용해되지 않으면서 낮은 수준의 과포화 상태를 유지한 실험에 대해서는 평균 결정 길이와 표준편차가 실험 결과와 20% 이내의 오차를 보였다. 앞에서 모델의 검증에 사용된 데이터가 LAM (L-아스파라긴 일 수화물)용액으로부터 얻어진 것이었다면 이후에는 HEWL (달걀 흰자 리소자임)를 사용하여 제품의 결정 크기 분포의 조절 가능성을 보였다. 마지막으로 폴리머 생산을 위한 고압 오토클레이브 반응기의 거동을 예측하기 위한

다중 구획 모델을 제안하였다. 복잡한 고분자 합성 메커니즘을 모사하기 위하여 반응기 내 임펠러의 회전이 중합에 미치는 효과와 중합 열로 인한 영향력을 순차적으로 평가하였다. 제안된 모델은 3D 구조를 가진 산업화된 반응기에서 생산된 두 가지 고분자의 물성을 7%이내 정확도로 예측할 수 있다.

본 학위논문에서는 다루는 시스템은 모두 분포 정수계 시스템으로 시간과 공간에 대하여 편미분방정식으로 표현할 수 있다. 고차 모델을 구축하기 위해 이산화 접근법을 기반으로 최소한의 가정 하에 시스템을 해석하였다. 이는 논문에 제시한 시스템 뿐만 아니라 시공간에서 예측 어려운 분포를 가지는 변수를 가진 모든 시스템에 대하여 적용이 가능하다. 이 논문이 앞으로 화학 공학 분야의 시스템을 해석하는 데 있어서 더 발전된 연구를 위한 지침서가 되기를 희망한다.

주요어: 수학적 모델링, 파라미터 추정, 분포정수계, 대기식 기화기, 인구 균형 모델링, 연속 결정화 공정, 고압 오토 클레이브 반응기

학 번 : 2014-22598